LEABHARLANN CHOLÁISTE NA TRÍONÓIDE, BAILE ÁTHA CLIATH | TRINITY COLLEGE LIBRARY DUBLIN
Ollscoil Átha Cliath | The University of Dublin

Terms and Conditions of Use of Digitised Theses from Trinity College Library Dublin

Copyright statement

All material supplied by Trinity College Library is protected by copyright (under the Copyright and Related Rights Act, 2000 as amended) and other relevant Intellectual Property Rights. By accessing and using a Digitised Thesis from Trinity College Library you acknowledge that all Intellectual Property Rights in any Works supplied are the sole and exclusive property of the copyright and/or other IPR holder. Specific copyright holders may not be explicitly identified. Use of materials from other sources within a thesis should not be construed as a claim over them.

A non-exclusive, non-transferable licence is hereby granted to those using or reproducing, in whole or in part, the material for valid purposes, providing the copyright owners are acknowledged using the normal conventions. Where specific permission to use material is required, this is identified and such permission must be sought from the copyright holder or agency cited.

Liability statement

By using a Digitised Thesis, I accept that Trinity College Dublin bears no legal responsibility for the accuracy, legality or comprehensiveness of materials contained within the thesis, and that Trinity College Dublin accepts no liability for indirect, consequential, or incidental, damages or losses arising from use of the thesis for whatever reason. Information located in a thesis may be subject to specific use constraints, details of which may not be explicitly described. It is the responsibility of potential and actual users to be aware of such constraints and to abide by them. By making use of material from a digitised thesis, you accept these copyright and disclaimer provisions. Where it is brought to the attention of Trinity College Library that there may be a breach of copyright or other restraint, it is the policy to withdraw or take down access to a thesis while the issue is being resolved.

Access Agreement

By using a Digitised Thesis from Trinity College Library you are bound by the following Terms & Conditions. Please read them carefully.

I have read and I understand the following statement: All material supplied via a Digitised Thesis from Trinity College Library is protected by copyright and other intellectual property rights, and duplication or sale of all or part of any of a thesis is not permitted, except that material may be duplicated by you for your research use or for educational purposes in electronic or print form providing the copyright owners are acknowledged using the normal conventions. You must obtain permission for any other use. Electronic or print copies may not be offered, whether for sale or otherwise to anyone. This copy has been supplied on the understanding that it is copyright material and that no quotation from the thesis may be published without proper acknowledgement.

Simulations of Foams and Liquid Surfaces

Kevin Geoffrey Bradley

A Thesis submitted to

The University of Dublin

Trinity College

for the degree of

Doctor of Philosophy.

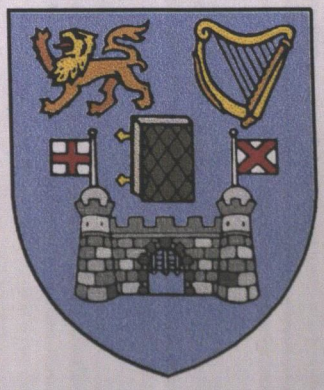

October 2000

© K. G. Bradley & University of Dublin

TRINITY COLLEGE
09 MAY 2001
LIBRARY DUBLIN
Thesis
6244

Declaration

This thesis has not been submitted as an exercise for a degree at any other University.

Except where otherwise stated, the work described herein has been carried out by the author alone.

This thesis may be borrowed or copied upon request with the permission of the Librarian, University of Dublin, Trinity College. The copyright belongs jointly to the University of Dublin and Kevin Geoffrey Thomas Bradley.

Signature of Author 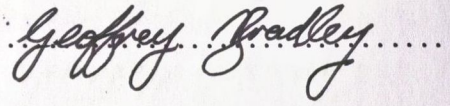

Kevin Geoffrey Thomas Bradley

October 2000

Acknowledgements

I'd like to start by thanking my supervisor, Professor Denis Weaire. Over the last three years he proposed many interesting reasearch topics and was a constant source of inspiration and tuition.

I would also like to thank Professor Ken Brakke for all the help and advice he provide on all aspects of his software package, The Surface Evolver. Without his help many of the calculations in this thesis would not have been possible.

Dr. Simon Cox, Dr. Stefan Hutzler, Dr. Robert Phelan, Dr. Nic Pittet and Dr. Claire Pittet (postdocs from the Foam group at one time or another) all provide me with support and advice. Thanks to Dr. Andy Kraynik, Dr. Jan Cilliers and Dr. Nic Rivier for informative converstation.

I'd also like to thank everyone in the Physics and Mathematics departments who assisted me, these include: Dr. Jim Sexton, Dr. Eamonn Cahill, Dr. Charles Patterson, Dr. Sarah McMurray, Dr. Phil Yecko and Dr. Turlogh Downes.

Research works best in a group environment, other members of the group from the last three years included Lola Alonso, Brendan DeBruijn and Paul Curtayne.

I'd like to thank Catriona and my parents for all the support they've provide for the duration of this thesis.

Financial support for this work came from TCD High Performance Computing grants, Enterprise Ireland, and Shell International Oil Products B.V., Shell Research and Technology Centre, Amsterdam.

Summary

In this thesis, we combine physics and numerical methods to describe the basic properties of foams and liquid surfaces.

In Part I, we provide a brief general introduction to the subject of foam physics, detailing what a foam is and how thin films are liquid surfaces form. We also discuss some uses of foams in industry.

In Part II, the structure of foams on a localised, individual bubble or single surface scale, is considered. Crystalline cylindrical foams form an excellent testbed for numerical calculations on the local rheology of a foam. We discuss a new model used in the simulation of these foams and investigate their energies and structural transition points. The model is extended to allow for calculations of wet cylindrical foams.

When two identical liquid drops are forced together a thin surface of contact forms between them before they coalesce. We consider a situation when coalescence does not occur and an instability arises as the two drops are forced out of each others way. A model of the two drops is discussed and we investigate any instabilities that arise.

In general, the energy of a dry foam depends only on its surface tension and surface area - and hence its geometry. For wet foams, the energy depends on an additional factor, its liquid content. The liquid forms in a network of long thin channels (known as Plateau borders), which meet at symmetric fourfold vertices. The problem becomes one of accurately describing the geometry of a foam with a proscribed liquid volume - a method for doing this is discussed.

Liquid flow through a network of Plateau borders is impeded by their geometry. We describe a model used to calculate the resistance to flow due to a single channel and a single symmetric fourfold vertex. The standard

theory of foam drainage ignores the contribution junctions make to resistance of flow. We find that their effect is large even at small liquid fractions.

In Part III, we discuss the numerical solutions of the foam drainage equation. All foams drain under the influence of gravity, so the foam drainage equation must be included when modelling additional foam properties - such as convective motion and bubble sorting. We present implementation details of a fast, efficient numerical solver - the Lax Wendroff method - and discuss its uses when solving the drainage equation.

Metal foams are of growing importance to industry and yet few theoretical models exist to describe their formation process. We present a simple theoretical and numerical model which describes the drainage and heat transfer processes that occur in a metal foam formation process. An analytical analysis is developed and may be used to provide a qualitative description of a solidified metal foam in terms of its initial parameters.

Finally, details of the computational software used in the second Part of this thesis are provided in Part IV. We describe the *Surface Evolver* and its applications to energy calculations of dry foam structures. Extensions to the software for modelling crystalline cylindrical foams and wet foams are provided. We also describe the fluid mechanics package *Fleunt* and discuss its applications to foam physics. Details of the conversion from *Evolver* to *Fluent* surface geometries are provided.

Contents

I Introduction 1

1 General Introduction 2

1.1 What is a foam ? 2

1.2 Fundamentals 3

1.2.1 The Laplace-Young Law 3

1.2.2 Plateau's rules 4

1.2.3 Wet foams 5

1.2.4 Energy expansions 6

1.2.5 Drainage process 7

1.2.6 Computations 8

1.3 Industrial applications 9

II Discrete systems 11

2 Cylindrical foams 13

2.1 Introduction 13

2.2 History, experiments and theory 17

2.3 Surface energy calculations 18

2.4 Calculation details, results and theory 19

2.4.1 Dry foams 19

2.4.2 Examples 21
2.4.3 Transition points 25
2.4.4 The twist boundary defect 28
2.4.5 Twist angle dependence on λ 30
2.5 Wet structures 32
2.6 Conclusions 37
2.7 Acknowledgements 38

3 Liquid instabilities **39**
3.1 Introduction 39
3.2 Geometrical parameters 41
3.3 Calculation details 43
3.4 Results 46
3.5 Conclusions 49
3.6 Acknowledgements 50

4 Vertex Corrections **52**
4.1 Introduction 52
4.2 Theory and Calculations 53
4.3 Volume corrections 56
4.4 Flow resistance corrections 59
4.4.1 Theory and entrance corrections 59
4.4.2 A circular duct 62
4.4.3 A Plateau border 66
4.4.4 A tetrahedral junction 71
4.5 Conclusions 75
4.6 Acknowledgements 76

III Continuous systems 77

5 Foam Drainage 79

5.1 Introduction 79

5.2 The foam drainage equation (f.d.e.) 81

5.2.1 Analytical solutions of the f.d.e. 82

5.3 Numerical analysis of the f. d. e. 84

5.3.1 Numerical Solvers 85

5.3.2 Comparison between methods from a performance viewpoint. 94

5.4 Conclusions 95

5.5 Acknowledgements 96

6 Metal Foams 97

6.1 Introduction 97

6.1.1 Metallic foam formation processes 98

6.2 The physical processes of metallic foam formation 99

6.2.1 Drainage 102

6.2.2 Heat diffusion and mass transport 102

6.2.3 Viscosity 104

6.2.4 Latent heat 104

6.3 Numerical methods 105

6.3.1 Dimensionless form of the metal foam equations 105

6.3.2 Boundary conditions 106

6.3.3 Discretisation 107

6.4 Results for one dimensional calculations 108

6.4.1 Numerical simulations of Case I 109

6.4.2 Numerical simulations of Case II 112

6.4.3 Analytical approximation of Case I 114
6.4.4 Analytical approximation of Case II 121
6.4.5 Analysis of solidification fronts 123
6.5 Analysis of two-dimensional metal foams 127
6.5.1 Numerical simulation of Case III 127
6.5.2 Numerical simulation of Case IV 128
6.5.3 Numerical simulation of Case V 133
6.5.4 Analytical approximations 135
6.6 Further analysis 137
6.6.1 Coalescence 137
6.6.2 Microgravity 141
6.7 Conclusions 141
6.8 Acknowledgements 142

IV Calculation details **143**

7 Numerical methods **144**
7.1 Introduction 144
7.2 The Surface Evolver 144
7.2.1 History 144
7.2.2 Evolver Basics 146
7.2.3 Convergence 147
7.2.4 Accuracy - an example 149
7.2.5 Eigenvectors and Eigenvalues, Hessian Techniques . . . 152
7.3 Energy calculations for wet structures 153
7.3.1 Wet bamboo structure 154
7.3.2 Wet 211 structure 156

7.4 Hessian techniques - Liquid drops 157
7.5 Static modelling of wet foams 161
7.5.1 Vertex correction calculations 164
7.6 Fluent - Modelling liquid flow in foams 166
7.6.1 The Evolver and Fluent 168
7.7 Conclusions 169
7.8 Acknowledgements 169

A Calculation details **170**

A.1 A derivation of the Laplace-Young Law 170
A.2 Volume calculations using the *Surface Evolver* 171
A.3 Surface energy of cylindrical crystalline structures 172
A.4 The foam drainage equation 173
A.4.1 A note on η 175
A.4.2 A note on N 176
A.4.3 Two dimensions 176
A.5 Metal foams - the dimensionless form of the foam drainage equation 177
A.5.1 Foam drainage equation 178
A.5.2 Heat transfer equation 179
A.5.3 Viscosity, specific heat and latent heat 179
A.5.4 Metal foam equations in 1d 180
A.5.5 Two dimensions 181

List of Figures

1.1 A foam is a two phase system, in this case gas bubbles (white regions) are dispersed within a continuous liquid medium (dark regions). ('Hive' - courtesy of Michael Boran). 3

1.2 An *idealised* dry foam ($\Phi_l = 0$) is a collection of monodisperse polyhedral cells typified by Kelvin's tetrakaidecahedra which must obey some simple local equilibrium rules. 4

1.3 A saddle deformation. The two principal curvature radii, R_1 and R_2 at a point P on the surface, define the local curvature, R, the mean local curvature, $\mathcal{K}$ and the Gaussian curvature, $\mathcal{G}$, of the surface at that point. At P, the mean curvature is zero because $R_1 = -R_2$. 5

1.4 Left, a *dry* ($\Phi_l = 0$) tetrahedral junction. Films meet three at a time on lines at 120°, and four lines meet to form the 4-fold vertex. Right, a *wet* ($\Phi_l \sim 0.005$) tetrahedral junction. The lines and vertex swell to accommodate the liquid. 6

2.1 Nitrogen gas is forced out of a pipette into a detergent solution forming equal sized bubbles. These bubbles rise into a cylindrical tube and may form ordered structures, the details of which depend on the ratio of tube to bubble radius, λ. 14

2.2 Photographs of some of the ordered structures typically found in experiments, (a) 211, with two bubbles per unit cell, (b) 321, with three bubbles per unit cell, and (c) 422, with four bubbles per unit cell. (Courtesy of Stefan Hutzler) 15

2.3 A 321 structure. The points on the surface of a cylinder are labelled by an integer, i, that increase with altitude. Moving from one vertex to the next in a given spiralling direction increases or decrease the altitude by k, l, or m units respectively. Vertices linked with a golden line are spiralling in the l direction. Vertices linked with a pink line are spiralling in the m direction. A vertex on one facet (e.g. the blue vertex) spirals to it's identical vertex on the next facet (e.g. the red vertex), via a move of k units, or a move of l and m units via an intermediary vertex (e.g. the green vertex). 16

2.4 Twist boundary in the 211 structure. The photos were taken at 1.5 second intervals. The twist moves down the tube with constant velocity without dispersing. (Courtesy of Stefan Hutzler.) 18

2.5 (A) The *Surface Evolver* takes a six bubble structure which is topologically identical to the 321 crystalline structure, and (B) rotates it through a uniform 'spiral boundary' angle, $\theta = 40°$. 22

2.6 An *Evolver* simulation of a 321 crystalline structure after two levels of refinement and area minimisation. 23

2.7 The internal films of 211 may simply be considered as surfaces which, through some spiral boundary angle, θ, match up at the top and bottom of the structure. The films do not need to be elements of a body to enclose a region. 24

2.8 *Surface Evolver* simulations of ordered cylindrical structures in the dry limit, $\Phi_l = 0$. 26

2.9 The total energy of various ordered cylindrical structures plotted against the ratio, λ, of tube to bubble radius. 27

2.10 A rotational twist may be applied to a 211 structure. The energy dependence of the structure on twist angle is generated using the *Surface Evolver*. 28

2.11 The energy of a dry 211 structure, $\Phi_l = 0$, varies quadratically with twist angle, θ, disproving the idea of a local energy minimum at some non-zero twist angle. 29

2.12 Applying a linear twist in the 211 structure produces a linear force. Numerical data - solid line, linear fit - dotted line. 30

2.13 A uniform twist, of 180^o, initially applied over part of a 211 supercell, will seek to minimise total surface energy by spreading out over the entire structure. 31

2.14 The minimum energy of the 321 structure for $\lambda = 1.3$ is dependent not only on λ, but also on a twist angle θ. 32

2.15 Wet crystalline structures where $\Phi_l = 3\%$. (Left) a wet 110 structure, (Right) a wet 211 structure. The green films show liquid-film interfaces where $\gamma = 1$, the blue films show film-film interfaces where $\gamma = 2$. The energy and area contribution due to faces on the surface of the cylinder is calculated using surface and line integrals on the edges on the cylinder surface. The 110 structure repeats periodically through a translation of height h in the z-direction. The 211 structure repeats periodically through a translation of height $\frac{h}{2}$ in the z-direction and a rotation of 180°. 34

2.16 The bamboo structure repeats periodically in the z-direction. The films on the surface of the cylinder have been removed. The blue films correspond to film-film interfaces where $\gamma = 2$. The green films correspond to liquid-film interfaces where $\gamma = 1$, and all the liquid is contained within the green films and the cylinder surface. 35

2.17 The 211 structure repeats periodically in the z-direction. The films on the surface of the cylinder have been removed. The blue films correspond to film-film interfaces where $\gamma = 2$. The green films are the Plateau borders and correspond to liquid-film interfaces where $\gamma = 1$. All the liquid is contained within the green films and the cylinder surface. 36

2.18 The variation of surface energy with liquid fraction for 211 and bamboo structures indicates a topological transition at $\Phi_l \simeq 0.16$. Data points from *Surface Evolver* calculations are fitted to the theoretical energy expansion outlined in section 1.2.4: $E_T = a - b\Phi_l^{\frac{1}{2}} - c\Phi_l$ 37

3.1 Photograph of the instability as seen experimentally. The two drops move out of each others' way to reduce the total energy of the system. (Courtesy of R. Monti.) 40

3.2 The initial setup of the system shows two liquid drops of volume V, fixed to rings of diameter D. They are separated by a distance d, which is progressively reduced to bring the drops into contact with each other. 42

3.3 When two non coalescing liquid drops are brought into contact, they initially retain cylindrical symmetry and have a circular surface of contact. 43

3.4 As two drops are pressed close together a critical separation distance, d_c, is encountered. Pressing the drops still closer together causes the cylindrical symmetry of the system to be broken as the drops distort moving out of each other way. The surface of contact between the two drops becomes elliptical from this point on. . . . 44

3.5 The solid curve shows the increase in normalised drop distortion J as the liquid drops are brought into closer contact (μ^{-1}). It is well approximated by a square root function (dashed curve). . . . 47

3.6 Prior to the point of instability the system can be seen to exhibit degeneracy of its two lowest eigenvalues (red and green curves). Degeneracy is lost as the distance between the two drops (μ^{-1}) is reduced beyond the point of instability. 48

3.7 Dependence of the critical point of instability as the normalised volume λ is altered. 49

4.1 A single straight Plateau border with uniform cross-sectional area A_{Pb}, and length L, generated using the *Surface Evolver*. 53

4.2 A two dimensional junction in a wet foam. In an idealised model, the Plateau borders forming between adjacent foam cells have a uniform width δ and length L, (A). A real foam has minimal line length with shape shown in (B). A wet foam has additional area, per Plateau border, at a junction - shown by the shaded region. This additional area may simply be considered as a correction to the length of a Plateau border, (C), so (B) and (C) represent the same junction. The flow and electrical resistance of a foam may also be consider in terms of an idealised model. An additional length correction accounts for the effects of junctions on these physical properties, (D). 55

4.3 A single tetrahedral vertex made up of four Plateau border arms of length L and asymptotic width δ. L is measured to the centre of the junction. Produced using the *Surface Evolver*. 56

4.4 Four Plateau borders of length L and cross sectional area A_{Pb} meet to form a tetrahedral vertex. The volume of the tetrahedral vertex may be consider as part of the liquid within the Plateau borders provided their lengths are adjust to an effective length, L_{eff}. The blue line indicates results from the *Surface Evolver*, the red line is a straight line fit. 58

4.5 A velocity profile of Poiseuille flow in a circular duct is parabolic. The profile is taken at a cross section at $x = \frac{L}{2}$, this ensures the flow is fully developed. The maximum velocity 4.4.2 may be read directly from the graph. The profile is produced using *Fluent*. . . . 64

4.6 Fluid entering a circular duct from the right initially causes a viscous layer to form at the inlet. The flow is still accelerating down the tube near the entrance, as the different colours in the figure suggest. Some short distance downstream, $\approx r_0$, predicted by Shah and London [61], the flow becomes fully developed and the velocity, u, becomes purely axial. This is evident from the parallel strips of constant velocity down the length of the sample. 65

4.7 The pressure on the walls of a Plateau border should vary linearly with its length according to equation 4.28. The image shows a three dimensional image of the surface pressure. The pressure inlet is the red area on the left of the picture and the pressure outlet is the blue area to the right of the picture. The image was produced by solving the Navier-Stokes equations for incompressible Poiseuille type flow using the numerical fluid mechanics package *Fluent*. . . . 67

4.8 The majority of flow in a Plateau border occurs in the centre. A small entrance effect is observed at the pressure inlet (velocity inlet) at the left of the picture. Flow is then fully developed and Poiseuille type as depicted by the distinctly different and parallel colored velocity regions. 68

4.9 Poiseuille flow through a Plateau border has a parabolic type profile. A slice across the width of the border produces a plane showing velocity contours, (top). A plot of contours against position confirms the existance of the parabolic type profile, (bottom). . . . 69

4.10 Fluent may be used to calculate the flow resistance, χ, of liquid in a Plateau border with fixed walls. The flow is Poiseuille type. χ may be calculated from equation 4.29. The numerical points produced using Fluent are plotted on the green line. A linear fit, $f(x) = ax + ba$, calculates the slope of the graph, and hence the flow resistance as $\chi \approx 50.66$ 70

4.11 A tetrahedral vertex showing the variation of static pressure on its surface. Produced using Fluent via Gambit and the Surface Evolver. 72

4.12 A vertex correction term for each Plateau border arm may be written as a length correction of 0.955 δ. The data points are calculated using the *Surface Evolver* and *Fluent*. The dark blue line is calculated for flow in through one Plateau border and out through three borders. The purple line is calculated for flow in through into one Plateau border and out one of the three symmetric borders. The red and green lines are fits of $f(x) = ax + ab$, and $g(x) = cx + cd$. The slope of the red line is $\frac{4}{3}(\chi)$, and the slope of the green line is $2(\chi)$. The flow resistance term for a single Plateau border is calculated as $\chi = 52$, and the intersection with the x axis is calculated as 0.955 δ. 73

4.13 A mid-plane cutting two of the arms of a tetrahedral vertex shows contours of the velocity magnitude. The contours should be straight and parallel for fully developed Poiseuille-type flow. Produced using Fluent via Gambit and the Surface Evolver. 74

5.1 A foam with a constant initial liquid fraction, $\alpha_l = 0.01$, dashed line, is not in an equilibrium state. Liquid will drain out of the sample over time and an equilibrium profile is reached when gravitational and capillary forces balance, solid line. 83

5.2 Adding liquid at a constant rate, Q_l, to the top of initially dry foam causes a solitary wave to form at the top of the sample and move downwards with an average velocity $u \propto Q_l^{\frac{1}{2}}$. The solid lines show the position of the solitary wave at dimensionless time, $\tau = 60, 120, 180, 240$. 84

5.3 Shown is a comparison between advective fronts produced by three different fluxes, F. Black line - the foam drainage equation, Red line - a smoother front produced by linearising the gradient term, Blue line - a sharper front produced by removing the gradient term. 88

5.4 The exact and numerical solitary wave solution of the foam drainage equation is shown. The numerical solution is produced using upwind differencing. A small amount of numerical diffusion is visible in the comparison between the solutions. $\Delta x = 0.1$, $\Delta t = 0.01$, $J = 1000$. 90

5.5 The exact and numerical solitary wave solution of the foam drainage equation is shown. The numerical solution is produced using the Lax method. A large amount of numerical diffusion is visible in the comparison between the solutions - indicating that the Lax methods is unsuitable for modelling the foam drainage equation. $\Delta x = 0.1$, $\Delta t = 0.01$, $J = 1000$. 91

5.6 The exact and numerical solitary wave solution of the foam drainage equation is shown. The numerical solution is produced using the Lax-Wendroff method. No dispersive effects are visible in the numerical solution. $\Delta x = 0.1$, $\Delta t = 0.01$, $J = 1000$. 91

5.7 The exact and numerical solitary wave solution of the foam drainage equation is shown. The numerical solution is produced using the MacCormack method. No dispersive effects are visible in the numerical solution. $\Delta x = 0.1$, $\Delta t = 0.01$, $J = 1000$. 92

5.8 The relative difference between the analytical and numerical solitary wave solution of the foam drainage equation with $\Delta x = 0.1$ is shown. The numerical methods are indicated by colour: Upwind - red line, Lax-Wendroff - green line, MacCormack - blue line. Clearly the two step methods are more accurate than the single step method. The error due to Lax is so large it is not shown. 93

5.9 As the grid step size Δx decreases, the numerical error, ϵ, from the upwind, Lax-Wendroff and MacCormack methods decreases linearly. It is clear that the truncation errors vanish to zero as the grid step size approaches zero. 93

6.1 A cross sectional cutting of a metal foam reveals the existence of a clearly defined network of solidified Plateau borders (dark regions) formed around bubbles with greatly varying radii (light regions). The aim of our model is to suggest initial conditions that may lead to a more homogeneous final product. Picture courtesy of John Banhart. 100

6.2 A sketch of the first two 1d cases considered. In Case I, the sample is cooled from both the top and bottom. In Case II, the sample is cooled from the bottom only. 108

6.3 Case I. Liquid metal is draining vertically in the sample as cooling fronts, originating at the top and bottom, move through the foam causing solidification. The dashed lines show successive profiles of relative density in increments of $\tau = 20$ up to $\tau = 100$. The solid line shows the final, solidified, relative density profile at $\tau = 133$. $\widehat{\Phi}_l^0 = 0.01$ and $Pe = 1.0$ 109

6.4 Case I. The dashed lines show successive profiles of the temperature, in increments of $\tau = 20$ from 0 to 120, as the sample cools and solidifies. The solid curved line is the final temperature profile of the solidified sample at $\tau = 133$. The solid vertical line is the solidification temperature, $\Theta_{crit} = 0.9$. 110

6.5 Case I. The total solidification time, τ_s, is proportional to the square of the length, L_ζ, of the foam sample. The solid curve shows values produced by the numerical metal foam program. The dashed curve is a square fit of $f(x) = ax^2$. $\widehat{\Phi}_l^0 = 0.01, Pe = 1$ . . . 112

6.6 Case I. The total solidification time, τ_s, is inversely proportional to the thermal conductivity, $\widehat{\kappa}_0$, of the metal. The solid curve shows values produced by the numerical metal foam program. The dashed curve is an inverse fit of $f(x) = \frac{a}{x}$. $\widehat{\Phi}_l^0 = 0.01, Pe = 1$ . . . 113

6.7 Case II. Liquid metal drains vertically in the sample as a solidification front, originating at the bottom, moves up through the foam. The dashed lines show successive profiles of relative density in increments of $\tau = 50$ from 0 to $\tau = 200$ The solid line shows the final, solidified, relative density profile at $\tau = 430$. $\widehat{\Phi}_l^0 = 0.01$ and $Pe = 1.0$ 114

6.8 Case II. The dashed lines show successive profiles of the temperature, in increments of $\tau = 50$ from 0 to 400, as the sample cools and solidifies. The solid curved line is the final temperature profile of the solidified sample at $\tau = 430$. The solid vertical line is the solidification temperature, $\Theta_{crit} = 0.9$ 115

6.9 A schematic diagram of the relative density profile for Case I at an early evolution time. The relative density at the top of the sample is *decreasing* linearly while the relative density at the bottom of the sample is *increasing* linearly. The total decrease of liquid in the upper part of the sample is shown as the top shaded and cyan triangles, while the total increase in liquid in the lower regions is shown as the lower shaded and cyan triangles, where $\zeta = \zeta_s$. However, the total loss/gain of liquid in equation 6.29 is approximated as the areas under the shaded triangles only. 118

6.10 Case I. The numerical (solid line) and analytical relative density profiles of the solidified metal foam sample are shown. The approximations used in the analytic method cause it to over calculate the slope of the density profiles. 120

6.11 Case II. A schematic representation of the drainage profile during early time evolution. The relative density at the bottom of the sample increases linearly while the remaining profile approximates that of a free draining foam. 122

6.12 Case II. The solid black lines shows the solidified relative density profile produced from the numerics. The blue and red lines show the two distinct parts of the analytic approximation. The dashed line shows the initial relative density profile. 124

6.13 The solid line shows the position, ζ, of the solidification fronts against time, τ, for the profile shown in Figure 6.3, as calculated by the numerical model. The dashed line shows the position, ζ, of the solidification fronts against time, τ, as produced by the analytical model. There is close agreement between the two plots. . 125

6.14 Case II. The red line shows the position, ζ, of the solidification front as a function of τ for the relative density profile shown in Figure 6.12, as calculated by the numerical model. The blue line shows the position of the solidification fronts produced by the analytical model. 126

6.15 Case III. (Top) shows a schematic of a two dimensional sample being cooled from all sides. Four solidification fronts form at the sides of the sample and move inwards as it cools - dashed lines. The sample drains predominantly in the ζ-direction due to gravity driven drainage, but also drains in the ξ-direction. (Bottom) shows the final relative density profile of the sample - which is highly inhomogeneous. 129

6.16 Case III. In the final phases of evolution, only the centre of the sample remains unsolidified. $\Theta_{init} = 1.0$, $\Theta_{crit} = 0.9$, solidification fronts have moved in from the top, bottom and sides of the sample. 130

6.17 Case IV. (A) shows a schematic of a two dimensional sample being cooled from the top and bottom only. Solidification fronts form at these sides of the sample and move inwards as it cools - dashed lines. The sample drains predominantly in the ζ-direction due to gravity driven drainage, but also drains in the ξ-direction. (B) shows the final relative density profile of the sample. The relative density profile viewed from the ζ-direction is identical to the profile of Case I. 131

6.18 Case IV. (A) A 3d view of the final temperature profile. (B) A side on view of the temperature profiles from $\tau = 0$ to $\tau = 100$, in increments of 20. The temperature profile is identical to its one dimensional counterpart, Case I, Figure 6.4. The final profile is at $\tau = 133$. 132

6.19 Case V. (A) Shown is a schematic of a two dimensional sample being cooled from its vertical sides only. Solidification fronts form at the sides of the sample and move inwards as it cools - dashed lines. The sample drains predominantly in the ζ-direction due to gravity driven drainage, but also drains due to pressure gradients in the ξ-direction. (B) Shown is the final relative density profile of the sample - which is highly inhomogeneous at the ends but completely homogeneous in the center. 134

6.20 Case III. The four solidification fronts combine and move inwards changing the liquid to solid and stopping further drainage as they go. The contours are shown for $\tau = 20$ to $\tau = 100$, at $\tau = 20$ intervals. The innermost contour is at $\tau = 127$, just before the entire foam solidifies at $\tau = 133$. $L_\zeta = L_\xi = 10$, $Pe = 1$, $\Theta_{init} = 1$, $\Theta_{crit} = 0.9$. 136

6.21 Case I. Coalescence occurs when the local liquid fraction drops below some critical value. The adjoining film between two bubbles bursts forming a larger single cell, and reducing the energy of the foam in the process. The local liquid fraction is reduced and the local bubble diameter increases. The variation in the relative density profile is sufficient to produce a slight fluctuation of local bubble diameter. 138

6.22 Case III: The effects of coalescence on the final bubble diameter distribution, (A), and relative density profile, (B), are shown. . . . 140

6.23 Case III: $\widehat{g} \approx 0.001$. The effects of microgravity on the formation process are considered. The fluctuation in the final density profile is simply 1000 times smaller as expected. 141

7.1 Two topologically identical objects: (a) shows a cube composed of flat sided triangular faces, while (b) shows a sphere, also composed of flat sided triangular faces. Both are generated using the Surface Evolver, the cubes surface energy is minimised as it is 'evolved' into the sphere. 145

7.2 The stages of minimisation of a sphere with radius 1: (a) shows the converged inputted plain sided structure, while (b) and (c) show the structure converged with one and two levels of refinement respectively. Note the flat red face in (a), refinement causes this parent facet to be replaced by four flat child facets in (b), and these child facets are further refined to replace themselves with four child facets of their own in (c). 150

7.3 Minimisation of a sphere of unit radius. The total number of conjugate gradient steps required to minimised the surface energy at each level of refinement, R_0 - R_5, is shown. The dashed line shows the analytical solution. 151

7.4 A *Surface Evolver* simulation showing a wet 110 foam. The blue facets are a gas-gas interface with $\gamma = 2$, the green facets are a gas-liquid interface with $\gamma = 1$, and the magenta facets are films on the surface wall where $\gamma = -1$. The magenta facets are replaced by edge integrals on the yellow and red edges. 154

7.5 A *Surface Evolver* simulation showing only the facets involved in calculations. The total energy calculated is for interior films minus the energy due to the Plateau border interface with the cylinder wall. The total energy contribution due to the films of the gas bubble and the border is calculated by simply adding the energy of the surface films for the dry foam case. $\Phi_l \approx 0.006$ 156

7.6 A wet 211 crystalline structures where $\Phi_l = 3\%$. The green films show liquid-film interfaces where $\gamma = 1$, the blue films show film-film interfaces where $\gamma = 2$. The energy and area contribution due to faces on the surface of the cylinder is calculated using surface and line integrals on the edges on the cylinder surface. The 211 structure repeats periodically through a translation of height $\frac{h}{2}$ in the $z - direction$ and a rotation of 180°. 157

7.7 *Surface Evolver* simulations of two liquid drops in contact. (Left) a minimised surface at one level of refinement, note the single flat green facet. (Right) a minimised surface at two levels of refinement. The single green parent facet has been replaced by four flat child facets. 158

7.8 Surface energy minimisation of two liquid drops in contact. The total number of conjugate gradient steps required to minimise the surface at each refinement level, *R0* - *R5*, is shown. The energy difference between successive refinement levels clearly converges to zero. 160

7.9 Minimisation of surface energy, at level *R1* refinement, for two liquid drops in contact. The energy drop at each refinement level contains structure as indicated by the figure. The two humps in the curve are caused by equiangulation and vertex averaging - processes which ensure the surface tessellation is uniform. 161

7.10 *Surface Evolver* simulations of a single tetrahedral junction. A foam in the dry limit ($\Phi_l \to 0$) obeys Plateau's rules and Laplace's law (A). For wet foam simulations, the lines are replaced by straight line tubes with triangular cross section and the point of intersection is replaced by an octahedron, (B). The structure is successively refined and minimised using conjugate gradient and Hessian techniques, (C), (D) and (E). The final minimised tetrahedral junction has its surrounding films removed, (F). $\Phi_l \approx 0.006$. 163

7.11 A typical residual graph produced by Fluent. The residuals of continuity and velocity are calculated after each iteration step. When the residuals converge the governing momentum and continuity equations are solved. 168

List of Tables

2.1 A comparison of experimental results, from Pittet *et al.* [29] and numerical results from Bradley *et al.* [17] and Weaire *et al.* [23] produced using the *Surface Evolver*, for dry $\Phi_l = 0$, cylindrical foam structures. 27

5.1 Numerical details for each of the three methods are shown. The Lax-Wendroff method computes the final position of its advective front $\sqrt{2}$ times slower than the upwind method, but with twice the accuracy. It is clearly faster than the MacCormack method. 94

7.1 The energy of a tessellated surface in the *Surface Evolver* converges towards a minimum as the tessellation is refined. The data is for a sphere of radius one. 152

7.2 The energy and instability point of the surface in Figure 7.7 depends on the number of surface facets. Refinement quadruples the number of triangles representing the surface - and hence provides a better approximation to the true surface energy. Refinement and minimisation must continue until the surface energy converges between two refinement levels. 159

7.3 A comparison between the computed radius, δ_n, and its asymptotic value at the end of a Plateau border arm, δ, is shown. Two methods are considered. If a method works correctly, $\frac{\delta_n}{\delta} \approx 1.0$ at high refinement levels. In Method I, $C = 0.75\delta$ or $C = 0.78\delta$, the radius is clearly not converging to its asymptotic value. In Method II, $C = 0.78\delta$, the radius converges to within 0.2% of the correct value after four levels of refinement and minimisation. (C is the vertex correction term.) 165

Part I

Introduction

Chapter 1

General Introduction

1.1 What is a foam ?

A foam is a two phase system, its continuous constituents define whether it is a solid or liquid foam, Figure 1.1, as its dispersed phase is always gas. When the dispersion of bubbles is homogeneous, we describe the foam as monodisperse, otherwise it is polydisperse. Its liquid fraction (we are primarily interested in liquid foams only) is labeled Φ_l, and its gas fraction is labeled Φ_g, so $\Phi_l + \Phi_g = 1$. Two extremes in liquid fraction exist; when $\Phi_l < 0.001$ we call the foam *dry* - or *Polyderschaum*, and when $\Phi_l = 0.36$ (close packing limit) the foam is *wet* - or *Kugelschaum*.

Foams, are closely related to emulsions and gels which form part of a group of objects known as colloids [1]. Foams, colloids, polymers and liquid crystals all fall under the general heading of soft matter [2].

As the area of foam research is quite broad, we only provide essential details relevant to this thesis. A more complete review of the subject is available in some recent books by Weaire and Hutzler [3], Gibson and Ashby [4] and Ekserova [5].

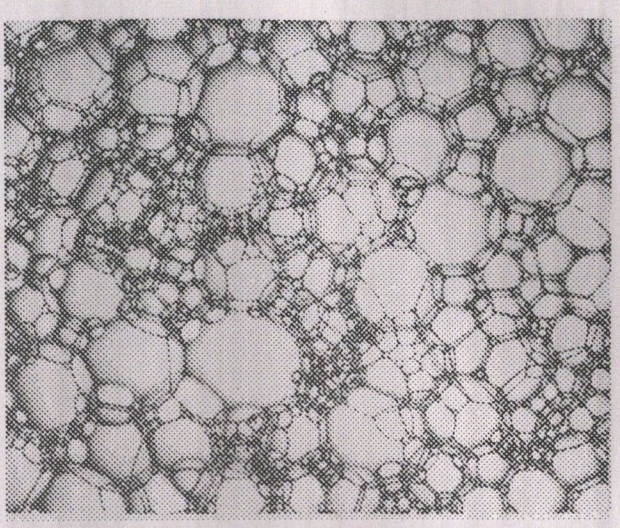

Figure 1.1: A foam is a two phase system, in this case gas bubbles (white regions) are dispersed within a continuous liquid medium (dark regions). ('Hive' - courtesy of Michael Boran).

1.2 Fundamentals

The basic equilibrium rules which describe the local behaviour of foam are based on the idea of an idealised dry foam, and are known as Plateaus rules. These were devised by Plateau [6] in 1873 and later verified by Taylor [7] in 1976. A good example of an idealised dry foam is simply a collection of polyhedral cells, e.g. Kelvin's tetrakaidecahedra, bounded by two dimensional curved walls, Figure 1.2. Normally, foams must also obeys the Laplace-Young Law.

1.2.1 The Laplace-Young Law

Consider two adjoining cells in a foam. They share a common interface where their films meet on a two dimensional surface. The law of Laplace-Young relates the local mean curvatures, $\mathcal{K}$, of this infinitely thin interface, and the surface tension of the films, γ, to the pressure difference between the

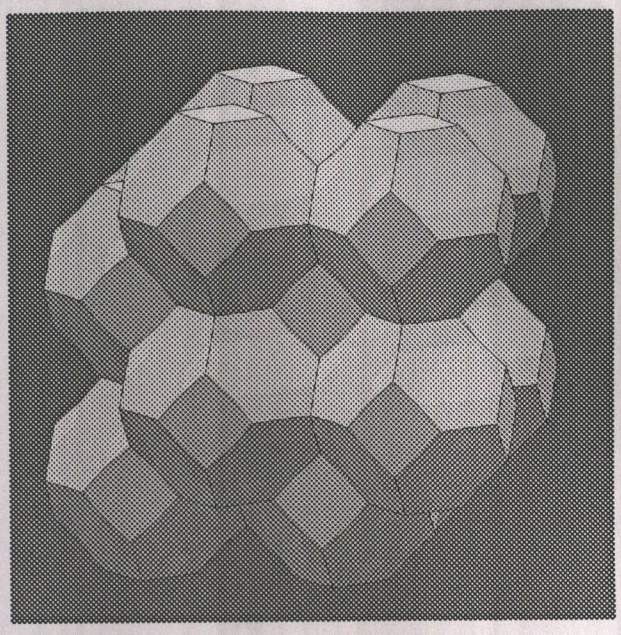

Figure 1.2: An *idealised* dry foam ($\Phi_l = 0$) is a collection of monodisperse polyhedral cells typified by Kelvin's tetrakaidecahedra which must obey some simple local equilibrium rules.

adjoining cells, Δp, by

$$\Delta p = 4\gamma\mathcal{K}$$

The local radius of curvature of the surface, R, is the inverse of the local mean curvature, $\mathcal{K}$. R is related to the two principal curvatures of the surface, R_1 and R_2 (Figure 1.3), by

$$\mathcal{K} = \frac{2}{R} = \frac{1}{R_1} + \frac{1}{R_2}$$

The Gaussian curvature of the surface is defined as $\mathcal{G} = (R_1 R_2)^{-1}$

1.2.2 Plateau's rules

Plateau is arguably the father of modern foam theory. His rules proceeded the Laplace-Young law, and describe the conditions necessary for a foam to exist in (meta-)stable equilibrium.

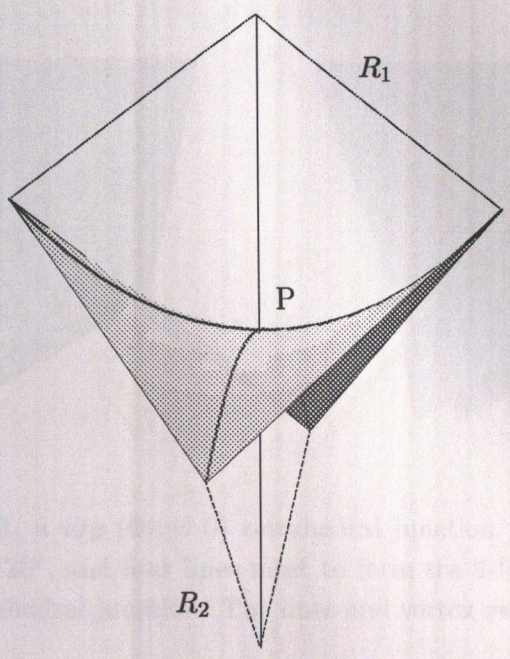

Figure 1.3: A saddle deformation. The two principal curvature radii, R_1 and R_2 at a point P on the surface, define the local curvature, R, the mean local curvature, $\mathcal{K}$ and the Gaussian curvature, $\mathcal{G}$, of the surface at that point. At P, the mean curvature is zero because $R_1 = -R_2$.

His rules state,

- for dry foams, films meet three at a time on lines at an angle of 120° to each other, Figure 1.4
- four lines meet to form a 4-fold tetrahedral vertex, Figure 1.4, for dry foams, it's symmetry is perfect with all angles, $\varepsilon = \cos^{-1}\left(\frac{1}{3}\right)$

1.2.3 Wet foams

As the liquid fraction, Φ_l, is increased the lines and vertices swell and the foam becomes *wet*, Figure 1.4. Wet foams must obeys additional rules

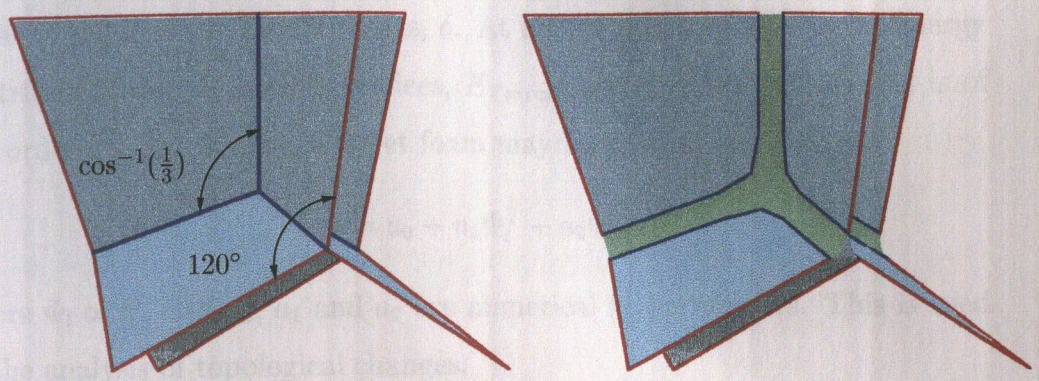

Figure 1.4: Left, a *dry* ($\Phi_l = 0$) tetrahedral junction. Films meet three at a time on lines at 120°, and four lines meet to form the 4-fold vertex. Right, a *wet* ($\Phi_l \sim 0.005$) tetrahedral junction. The lines and vertex swell to accommodate the liquid.

- liquid gathers in the lines which swell to form Plateau borders,
- the tetrahedral junctions swell to form symmetric fourfold vertices[1]
- the thin films remain infinitesimally thin - they do not swell and so retain no liquid

The Laplace-Young law can also be applied to wet foams.

1.2.4 Energy expansions

When analyzing structural transitions in wet foams, it is useful to write the energy of the foam as an expansion of the form

$$E = E_{dry} + E_{PB} + E_{Vertex}$$

as suggested by Weaire and Hutzler [3]. The energy of the dry foam structure is given by E_{dry}. At low liquid fractions, $\Phi_l \lesssim 0.01$, only the energy

[1]Stable eightfold vertices may form at a sufficiently high liquid fraction.

contribution due to swollen Plateau borders, E_{PB}, is relevant and is of the order of the Plateau border radius, δ. At higher liquid fractions, the energy contribution due to swollen vertices, E_{Vertex}, becomes important, and is of the order δ^2. The energy of a wet foam may be written as

$$E = a_0 + a_1 \Phi_l^{\frac{1}{2}} + a_2 \Phi_l$$

where $\Phi_l \propto \delta^2$, and a_0, a_1 and a_2 are numerical fit parameters. This is used in the analysis of topological changes.

1.2.5 Drainage process

A wet foam consists of a network of Plateau borders, which meet at tetrahedral junctions, surrounding the gas filled cells. An equation, formally known as the *foam drainage equation* - Verbist and Weaire [8], Verbist *et al.* [9] and Weaire *et al.* [10], describes the flow of liquid through such a network of Plateau borders. Several idealisations are made in this model, they include;

(i) At low liquid fractions, $\Phi_l < 0.01$, the Plateau borders are long and straight and contain all of the liquid in the foam. The liquid content of the tetrahedral junctions is ignored

(ii) The surface viscosity of the Plateau border walls is sufficiently high to inhibit surface flow, i.e. a no-slip boundary condition is applied to the walls, reducing the problem to one of Poiseuille flow

(iii) The resistance to flow in the Plateau borders is approximated as an effective viscosity, but the resistance to flow due to the junctions is ignored

Recent publications by Koehler *et al.* [11, 12] have called into question the reliability of (ii) - at least under certain circumstances - and have presented

a new foam drainage model.

We present new calculations of flow resistance due to Plateau border geometry and junction geometry in Chapter 4. The resistance corrections due to junction geometry are shown to be significant even at low flow rates, where $\Phi_l \approx 0.01$, possibly calling into question the reliability of (iii), and maybe even the reliability of the new drainage model.

Nevertheless, the foam drainage equation produces realistic results and we use it to simulate drainage in Chapter 5, and to model metallic foam formation processes in Chapter 6.

1.2.6 Computations

The *Surface Evolver* [13] may be used to perform accurate calculations on dry and wet foams. It takes as input some predefined topological structure and engages in an iteration of local variables to minimise the surface energy under certain conditions. The *Surface Evolver* is used extensively in the calculation of foam properties - notable contributions are from Phelan [14], Phelan *et al.* [15], Weaire and Phelan [16], Bradley *et al.* [17, 19], Bradley and Weaire [18], Kraynik *et al.* [20, 21], Reinelt *et al.* [22] and Weaire *et al.* [23]. We use it for calculations in Chapters 2, 3 and 4. A detailed description of its functionality is described in Chapter 7 along with numerical details of calculations from these Chapters.

Fluent, [24] is a computational fluid mechanics package. We use it model the flow resistance of a Plateau border and a tetrahedral junction in Chapter 4. The *Evolver* is used to produce a surface mesh of the required structure. A special script is used to transfer the geometrical surface data from the *Evolver* into *Gambit* - a preprocessor package for *Fluent*. The structure is then meshed and transferred into *Fluent* enabling the calculation of flow

resistance for complex geometrical geometries. This is a new technique we have developed, Bradley *et al.* [19].

1.3 Industrial applications

Foams are widely used in industry, their unique physical properties make them ideal for many important applications. Several examples are provided to elucidate this point.

Possibly their most popular use is in the production of beer! As beer is poured, bubbles of gas are nucleated and form a fine foam. The process is vital in producing the taste of the beer - without nucleation the beer would be flat.

Foam fractionation is used to separate mixtures of solutions with different surface activities. Solute absorbs on the surface of bubbles which move up a fractionation cylinder leaving the remaining constituents in a pool of liquid. The solute may be removed from the surface of the foam at the top of the cylinder, Weaire and Hutzler [3].

Foam flotation is used extensively in the mineral extraction industry. Finely ground ore is suspended in a foamable liquid which is agitated to form the foam. Minerals which are rich in metal and thus hydrophobic remain suspended in the foam, while the hydrophyllic particles, low in metal, drain through the foam. The metal rich minerals are removed from the surface of the foam, Weaire and Hutzler [3].

Aqueous foams may be used in enhanced oil recovery. 5 - 10% of oil flows naturally out of an oilfield in a process known as primary extraction. A further 10 - 40% is obtained by secondary extraction. This involves boring several injector wells around the production well and pumping liquid down

these wells to force the oil out the primary well. The injected fluids are less viscous than the oil, and as a result flow through the oil without sweeping it all out. The residual oil is retrieved by adding chemicals which reduce interfacial tensions allowing the oil to be gathered. These chemicals are expensive so it is advantageous to distribute them in a foam, Weaire and Hutzler [3] and Taupin [25].

Foams are widely used in the construction industry. Solid polystyrene boards are used for insulation in building and in the construction of roads.

Sheets of lightweight metal foams are now commercially available - typically these are metal foams pressed between two thin sheets of aluminum. Though extremely lightweight, they are incredibly strong due to the properties of the constituent metal and their cellular structure. Typical uses range from applications in the automobile manufacture industry, Seelinger [26], to possibly future use in the lightweight construction of space-frames made from aluminum foam sandwiches, Baumgarter *et al.* [27]. Metal foams are particularly interesting and are discussed extensively in Chapter 6.

The importance of foams in the oil production, mineral refinement and metal foam production industries coupled with the complexities of studying these dynamic systems has meant that most of the research in these fields has been empirically based.

In this thesis we use numerical calculations to provide a firm physical understanding of underlying properties of foams. In particular we present a detailed first analysis of the metal foam formation process in chapter 6.

Part II

Discrete systems

Introduction

In this part of the thesis, we concentrate on performing calculations at the level of individual foam cells. We use the *Surface Evolver* to track the energy and volume of bubbles and the liquid which forms in Plateau borders between them. We use *Fleunt* to calculate the effects of liquid flow on individual Plateau borders and tetrahedral junctions.

Chapter 2

Cylindrical foams

2.1 Introduction

When soap bubbles of equal size are introduced into a glass cylinder, an ordered cylindrical foam structure may form. The bubbles, of radius r, are normally produced by injecting nitrogen gas into a detergent solution below a cylindrical tube of radius R - this is typified by the experimental setup shown in Figure 2.1. A remarkable range of ordered structures may be observed, Figure 2.2, provided that the ratio of bubble to tube radius, $\lambda = \frac{R}{r}$, remains small. The interior foam is disordered at values of $\lambda > 3$.

In this Chapter, we sketch the history of cylindrical foams and provide computational results aimed at explaining some of the properties of these beautiful ordered structures. It is convenient to consider some of the more modern experiments first as a means of introducing the basic properties of these structures. Our goal is to use numerical techniques to investigate and hopefully explain these observations.

The recent history of this subject began in 1992 when Weaire *et al.* [28] - engaged in a the study of drainage waves - used relatively large bubbles

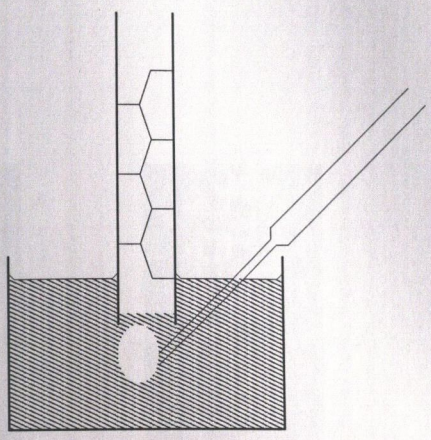

Figure 2.1: Nitrogen gas is forced out of a pipette into a detergent solution forming equal sized bubbles. These bubbles rise into a cylindrical tube and may form ordered structures, the details of which depend on the ratio of tube to bubble radius, λ.

in a cylinder and observed crystalline structures. The key features of these structures were identified in the ensuing publications by Weaire *et al.* [28] and Pittet *et al.* [29], but the most important one concerns the general nature of the surface structure on the cylinder wall. The surface structure consists entirely of hexagons and the junctions of this two-dimensional hexagonal pattern are threefold vertices, as required by Plateau's equilibrium rules [6].

The description of the surface structure does not stop there. Pittet *et al.* [30] observed that these hexagonal faces form a triangular lattice on the cylindrical face, with three spiraling families of k, l and m reticular lines. In terms of topology alone, there are infinitely many distinct ways of wrapping this hexagonal pattern on a cylinder, each of which may be identified with the three positive integers (k, l, m). The vertices are labeled by an integer i. Moving from vertex to vertex in the k, l or m spiralling direction increases i by k, l or m units respectively. Figure 2.3 shows an example of the (3,2,1) structure to help elucidate this point. It is clear from the Figure that $k =$

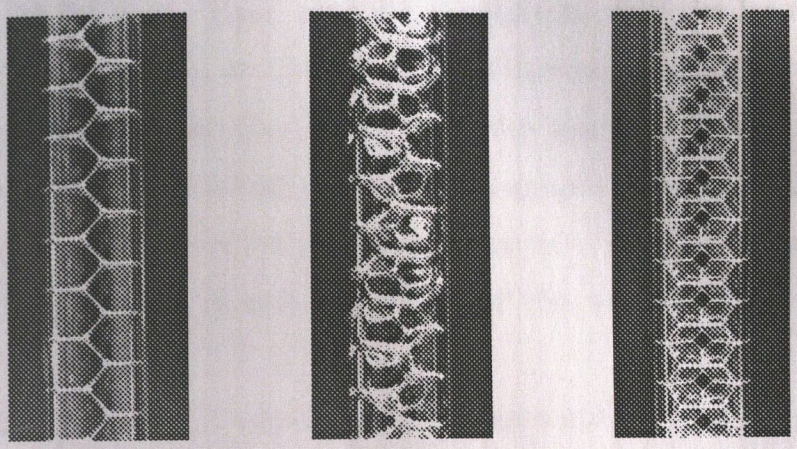

(a) 211 (b) 321 (c) 422

Figure 2.2: Photographs of some of the ordered structures typically found in experiments, (a) 211, with two bubbles per unit cell, (b) 321, with three bubbles per unit cell, and (c) 422, with four bubbles per unit cell. (Courtesy of Stefan Hutzler)

$l + m$.

This labeling system is not new - it is borrowed from the subject of phyllotaxis devised by Thompson [31], which classifies widely occurring botanical structures such as cones, daisies and sun flowers. Snakes scales and some viruses consist of ordered arrangements on cylinders, and are also classified using this system.

The study of cylindrical foams goes beyond the understanding of the hexagonal surface structure. The ordered internal cells are at least as interesting as the surface structure and include the common types of cells which

2.2 History, experiments and theory

Observations of these elegant structures were first recorded by Mann and Stephens [32] in 1933. They obtained photographs very similar to those in Figure 2.2 by passing air through oil and observing the bubbles as they moved up through a glass tube. They immediately identified these structures as being highly ordered and felt that their photographs 'cannot but fail to do full justice to the beauty of the phenomena observed'. They also stressed the 'unlimited possibilities' of such structures, but this was the extent of their work on this subject.

Twenty years later, J.D. Dodd [33] performed a number of experiments in an attempt to prove the existence of Kelvin's hypothesised tetrakaidecahedron. He constructed a cylindrical foam by blowing individual bubbles, one at a time, into a cylinder. However, he only created the simplest arrangements featuring these cells.

One of the most striking effects that can be observed in a crystalline cylindrical foam is the transformation from one structure to another. This can be provoked by wetting the foam with the steady addition of liquid or by varying pressure so as to expand or contract it. In the late '90s, these transformations were recorded and discussed in a series of papers.

In 1996, Pittet *et al.* [30] noted that the transitions observed are due to the creation of motion of a single dislocation. These transitions have been interpreted with 2D dislocation theory in the spirit of Bragg and Nye [34].

In the same year, Boltenhagen and Pittet [35] showed that a crystalline foam is stable under a steady liquid flow rate $Q < Q_C$. When the flow rate exceeds Q_C the foam undergoes a structural transition. Two years later Boltenhagen *et al.* [36] reported that particular sequences of transitions are observed under compression or expansion (or wetting and drainage). These

sequences of transitions are characterised by hysteresis.

One particularly surprising effect was discovered - the twist defect. A localised defect was observed by Hutzler *et al.* [37], whose stability and behavior has yet to be explained, section 2.4.4. Figure 2.4 shows snapshots of a crystalline foam sample as the defect passes through it.

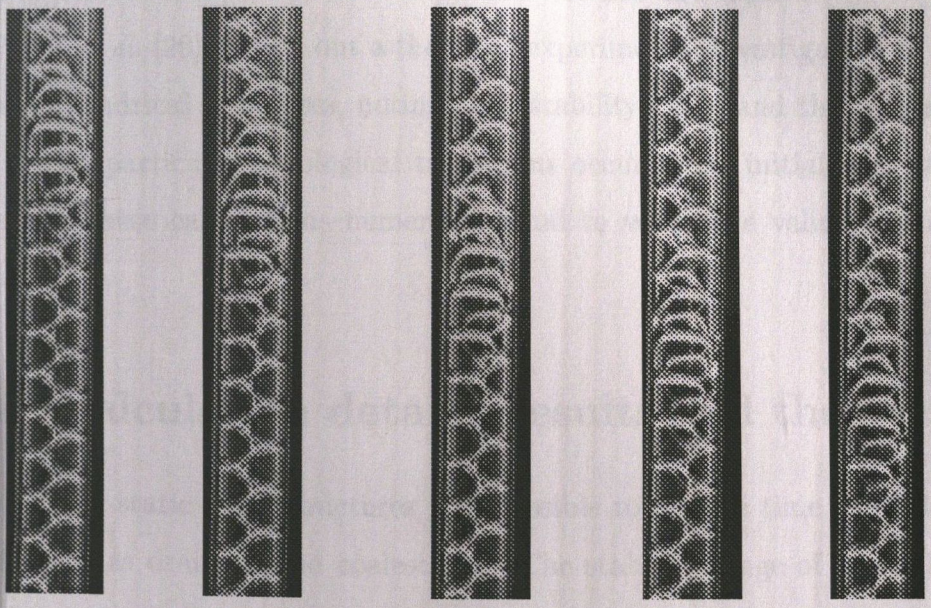

Figure 2.4: Twist boundary in the 211 structure. The photos were taken at 1.5 second intervals. The twist moves down the tube with constant velocity without dispersing. (Courtesy of Stefan Hutzler.)

2.3 Surface energy calculations

A foam is a dynamic systems with many physical processes occuring over varying timescales. Remarkably, the stability of these crystalline structures is largely unaffected by dynamic effects such as drainage (at low flow rates)

and coalescence. Their robust nature makes them interesting to study. Furthermore, they readily form at low liquid fractions, and are stable in the dry limit, $\Phi_l \to 0$.

Static foams may be modelled using the *Surface Evolver* [13]. In the dry limit, $\Phi_l = 0$, foams are far less complex to model as Plateau borders vanish, becoming lines and four-fold vertices are reduced to points. In principle the *Surface Evolver* is capable of handling both wet and dry cases.

Pittet *et al.* [29] carried out a thorough experimental investigation of the simpler cylindrical structures, noting their stability range and the values of λ at which particular topological transitions occur. Our initial goal is to reproduce these calculations numerically and to verify the validity of our model.

2.4 Calculation details, results and theory

By studying static foam structures it is possible to remove time dependent effects such as drainage and coalescence. The stability range of crystalline structures may be investigated allowing us some insight into the process of structural transitions.

Numerical calculations are conveniently divided into two distinct regimes,

(i) foams in the *dry* limit, $\lim \Phi_l \to 0$

(ii) and *wet* foams, $\Phi_l \lesssim 0.1$

2.4.1 Dry foams

Crystalline structures forming with non-zero liquid fractions, $\Phi_l > 0$, may completely drain to form dry foams. Therefore, numerical calculations using

dry foams are relevant.

The *Surface Evolver*, [13], is a computer program that minimises the energy of a surface subject to certain constraints. The energy can include surface tension, gravity and a variety of other forms. Constraints can be geometrical constraints on vertices and edges or can be constraints on integral quantities such as body volumes. Minimisation is done by evolving a surface down the energy gradient via a number of techniques such as gradient descent or conjugate gradient, see Chapter 7.

We are interested in a three dimensional model of a foam confined within a cylinder. The bubble volumes are constrained and in general the total energy of the foam, E_T, depends only on its surface tension and total film area,

$$E_T = \gamma S,$$

where γ is the surface tension, and S is the total film area.

The foam structure is formed and infinitely spirals up through the cylinder with a period defined by its spiral constants k and l. Experimentally the top of a 'real' foam sample has some bubbles in contact with air, but otherwise the approximation of a continuous system is good.

A crystalline structure formed within a cylinder has two clearly defined regions. These regions are

- films within the cylinder, with bulk energy E_F
- films on the cylinder surface, with bulk energy E_S

so the total energy of the bulk foam may be written as

$$E_T = E_F + E_S$$

The total surface area of the cylinder wall remains unchanged as different crystalline structures are formed, therefore the bulk energy of films on the cylinder wall remains constant.

Previous calculations of crystalline foam structures, by Phelan [14], Weaire and Phelan [39] and others, made use of the *Torus* model in the *Surface Evolver*. Their modelling involved the unnecessary calculation of films on the cylinder surface. Furthermore, it was not possible to use the *Surface Evolver Torus* model with what we call a 'spiral boundary condition'. This was a limiting factor as such a boundary condition can greatly reduce the size of computations for structures such as 321 and 431. The spiral boundary condition matches the structure at the bottom of a finite cylindrical structure to that at the top, but allowing a relative rotation through an arbitrary angle, θ.

Excluding films on the cylinder wall and allowing for spiral boundary conditions greatly reduces the computational resources required to minimise these structures. A model must:

- concentrate on the energy of films within the cylindrical boundary
- allow for spiralling structures
- tackle the problem of gaps between facets and the cylinder wall

Following consultations, Brakke [40] wrote an additional model within the *Evolver* known as the *screw_symmetry* group model. Most of the calculations in this Chapter use this new model.

2.4.2 Examples

We show an example of how one of the structures - the 321 - is obtained. One of the powerful aspects of the *Surface Evolver* is its ability to take a

topological object and minimise it subject to certain constraints. The 321 structure, with three bubbles per unit cell, wraps itself around a cylinder at an *unknown* angle. To model this structure we generate a data file for the *Evolver* which is topologically similar to a 321 structure. See section A.2.

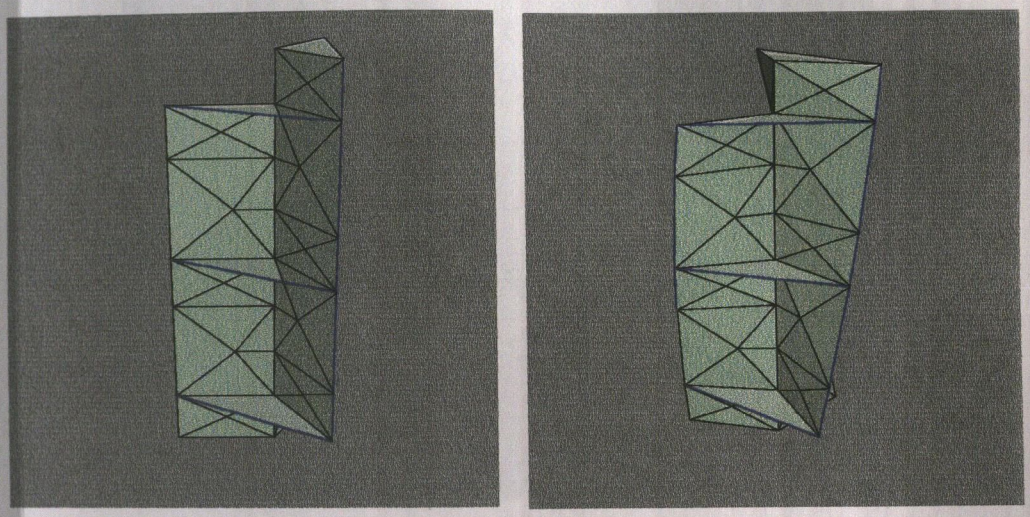

(A) (B)

Figure 2.5: (A) The *Surface Evolver* takes a six bubble structure which is topologically identical to the 321 crystalline structure, and (B) rotates it through a uniform 'spiral boundary' angle, $\theta = 40°$.

Figure 2.5 (a) shows a crude structure which is topologically identical to the 321 structure. It contains two unit cells - i.e. six *bubbles*. Each *bubble* has six lines on the surface of the cylinder (this becomes clearer as the surface is refined), corresponding to the hexagonal *surface structure* previously mentioned. The films on the surface walls have been removed to reduce computational time and their energy and volume content are included using surface integrals, see Appendix A.2.

Following two levels of minimisation, the crystalline structure, Figure 2.6, looks similar to a region of six bubbles in the photograph of a 321, Fig-

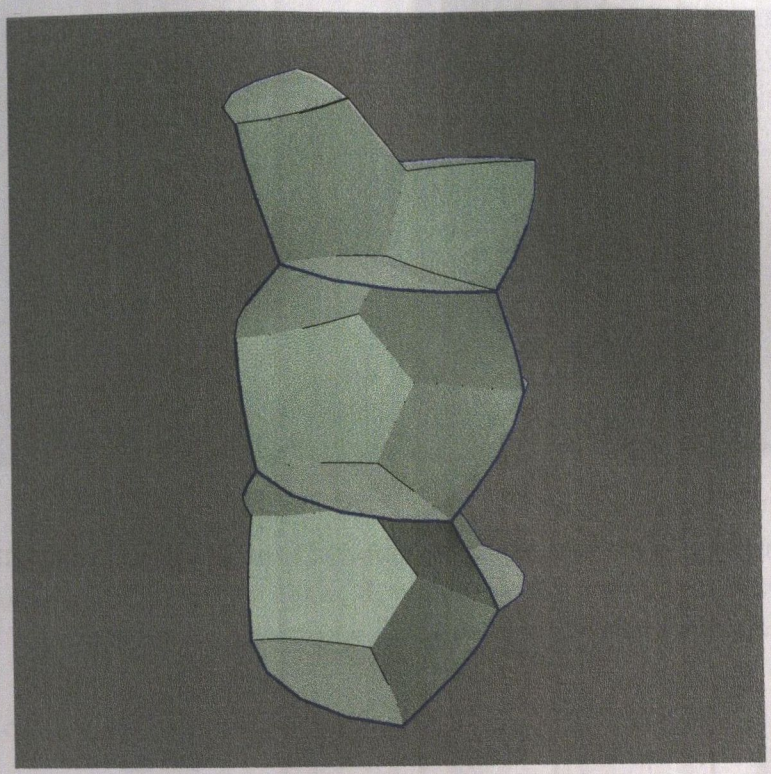

Figure 2.6: An *Evolver* simulation of a 321 crystalline structure after two levels of refinement and area minimisation.

ure 2.2(b).

Film type dry structures

All crystalline structures are periodically reproducible, in the direction of the cylinder axis, through some rotational angle θ. The *Evolver's screw_symmetry* model can be exploited to make use of this symmetry.

The energy of the interior films for some structures, such as 211, may be calculated in isolation of the bulk structure, so their energy may be computed to a high degree of accurately. Below are the initial film models of the 211 spiral structure, see Figure 2.7, and the films after three levels of refinement.

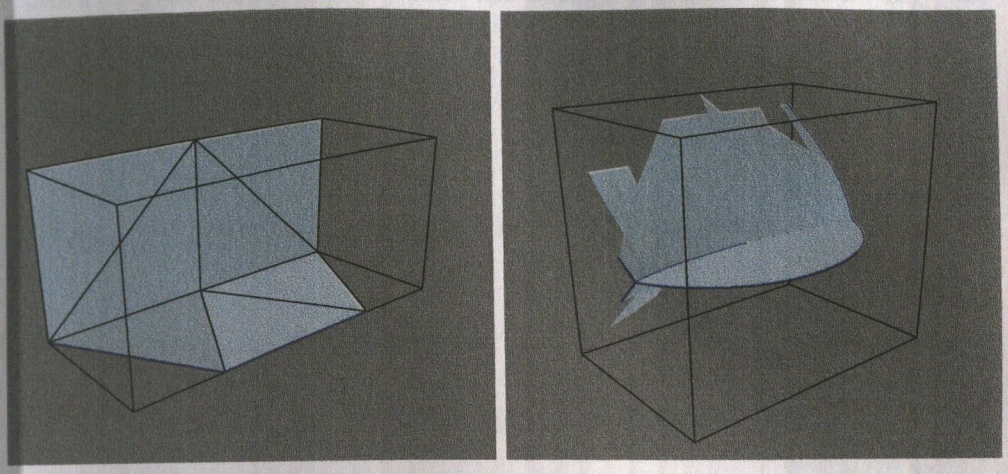

Figure 2.7: The internal films of 211 may simply be considered as surfaces which, through some spiral boundary angle, θ, match up at the top and bottom of the structure. The films do not need to be elements of a body to enclose a region.

Theory of dry structure energy

The theory of a cylindrical dry foams energy may be understood as follows:

Isolating several Kelvin cells in a cylinder causes them to contort to fill the required shape. Kelvin cells have the lowest known surface area for a *single* space filling cell, so the contorted cells must have an energy greater than the undistorted cells.

The energy of these structures is broken into two parts; an interior film energy, E_F and a cylinder surface energy, E_S, section 2.4.1. For simple structures (where, for example $\lambda < 3$) the total energy contribution from the cylinder surface films will be reasonably large. However, for very large λ, this contribution will be very small. Also, the internal cell structure for larger λ will be that of Kelvin's tetrakaidecahedra. Thus as λ increases we would expect the total energy to converge towards the Kelvin cells energy.

Calculations show that as the complexity of the crystalline structures increase (i.e. as they head towards bulk) the cylinder surface energy, E_S,

goes down, Figure 2.9. For dry foams the energy variation depends only on λ, and may be written as

$$E_T^B(\lambda) = E_F^B(\lambda) + 3.224\lambda^{-1}$$

per bubble, see Appendix A.3. For Kelvin $E_T^{PB}(\lambda) \sim 5.3063$

2.4.3 Transition points

Phelan and Weaire [14, 39] used the *Surface Evolver* to perform a number of accurate simulations of these structures in an attempt to reproduce these transition points, but were limited due to restrictions in their model.

We implemented the new *Evolver screw_symmetry* group model and performed simulations of many of the observed structures (Figure 2.8) calculating their range of stability and the transition points from one structure to another.

In each case the equivalent spherical bubble radius, r, was varied over an appropriate range. The relative energies of competing structures, such as those in Figure 2.8, are shown in Figure 2.9.

M. A. Fortes *et al.* [41] have discussed the much simpler case of 2D foams confined to a strip, but little theory is available for the interpretation or prediction of the energies in the 3D case. Nor can they be directly measured. Nevertheless, the agreement between experimental results, by Pittet *et al.* [29], and these simulations is quite good - as shown in Table 2.1.

It should be noted that crystalline foam structures are meta-stable well beyond their transition point. This has been observed experimentally by Pittet *et al.* [29] and verified numerically, Figure 2.9.

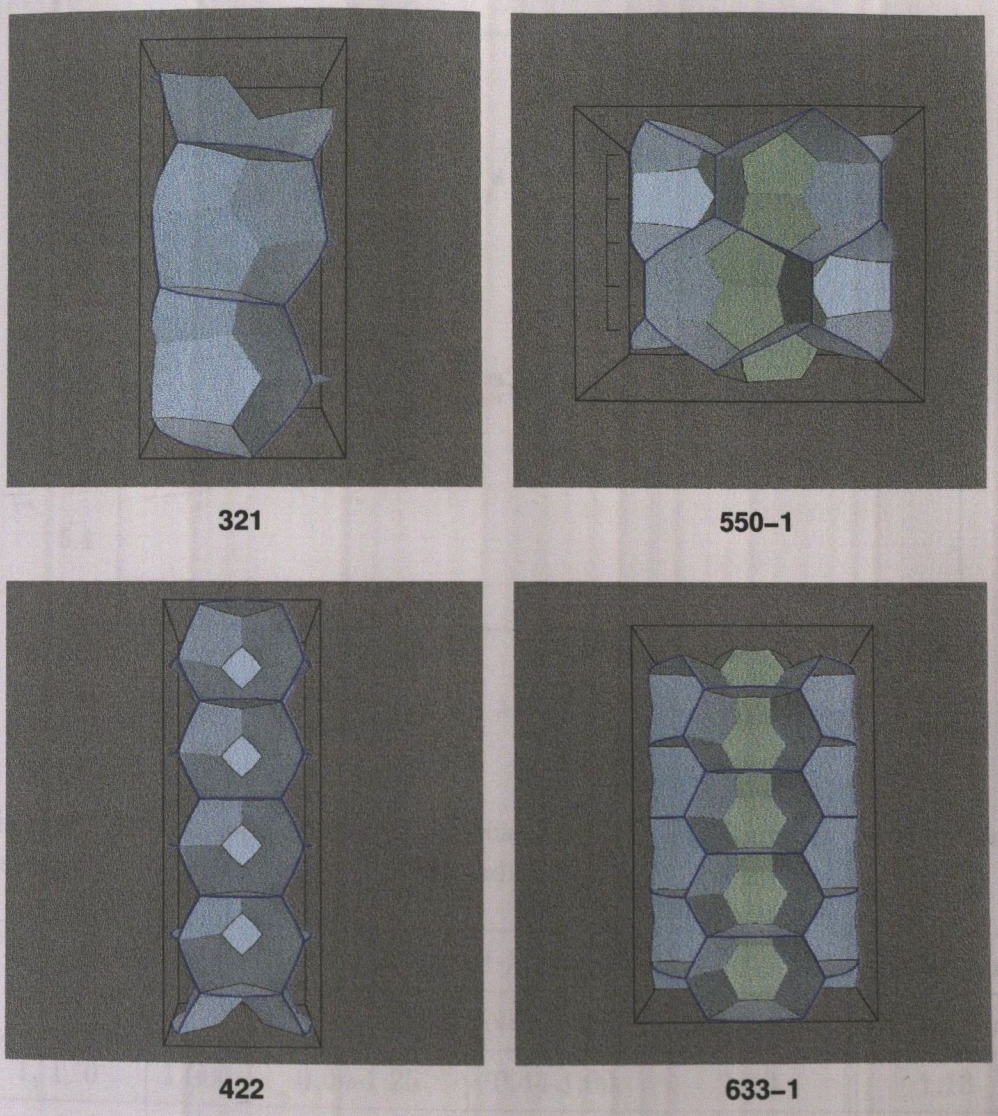

Figure 2.8: *Surface Evolver* simulations of ordered cylindrical structures in the dry limit, $\Phi_l = 0$.

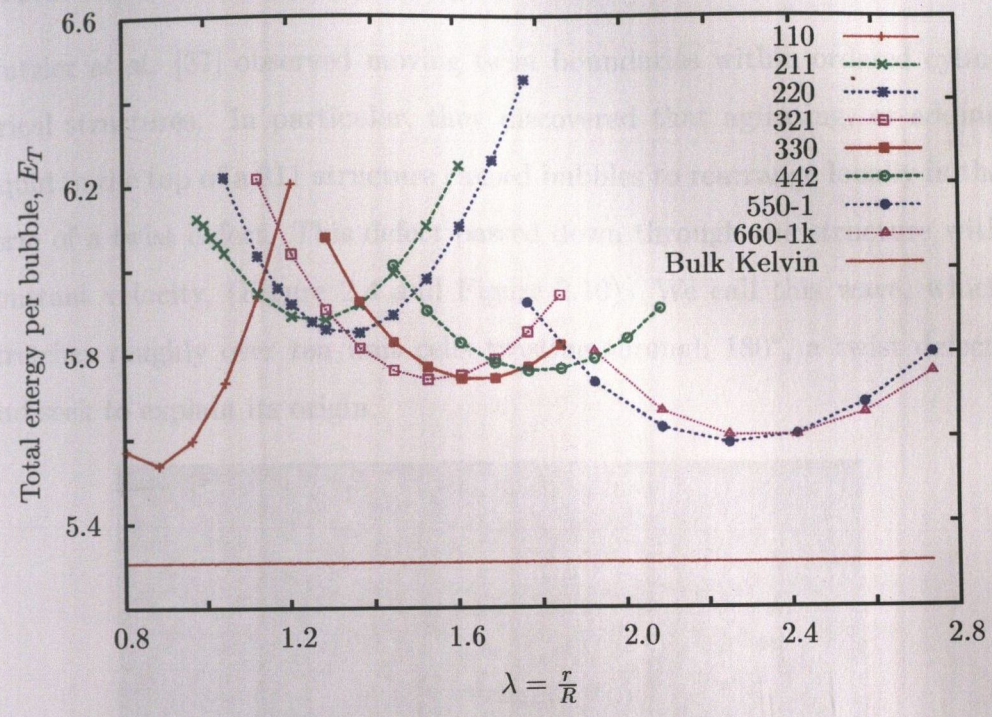

Figure 2.9: The total energy of various ordered cylindrical structures plotted against the ratio, λ, of tube to bubble radius.

k, l, m	V	Range of λ		Structural transition point	
		Experimental	Numerical	Experimental	Numerical
1, 1, 0	1.000	0.44-1.25	0.44-1.60	1.10	1.13
2, 1, 1	1.732	1.05-1.52	1.05-1.70	1.17	1.25
2, 2, 0	2.000	1.10-1.24	1.15-1.80	1.43	1.35
3, 2, 1	2.646	1.25-1.83	1.13-1.90	1.53	1.61
3, 3, 0	3.000	1.53-2.34	1.30-1.90	1.75	1.77
4, 4, 2	3.464	1.25-1.98	1.50-2.20	2.22	1.90
5, 5, 0 - 1	5.000	1.55-2.38	1.65-2.75	2.36	2.42
6, 6, 0 - 1k	5.169	1.76-2.56	1.94-2.75	-	-

Table 2.1: A comparison of experimental results, from Pittet *et al.* [29] and numerical results from Bradley *et al.* [17] and Weaire *et al.* [23] produced using the *Surface Evolver*, for dry $\Phi_l = 0$, cylindrical foam structures.

2.4.4 The twist boundary defect

Hutzler *et al.* [37] observed moving twist boundaries within ordered cylindrical structures. In particular, they discovered that agitating, or adding liquid to the top of a 211 structure caused bubbles to rearrange locally in the form of a twist defect. This defect passed down through the structure with constant velocity, (Figure 2.4 and Figure 2.10). We call this wave, which stretches roughly over ten unit cells twisting through 180°, a twist defect, and seek to explain its origin.

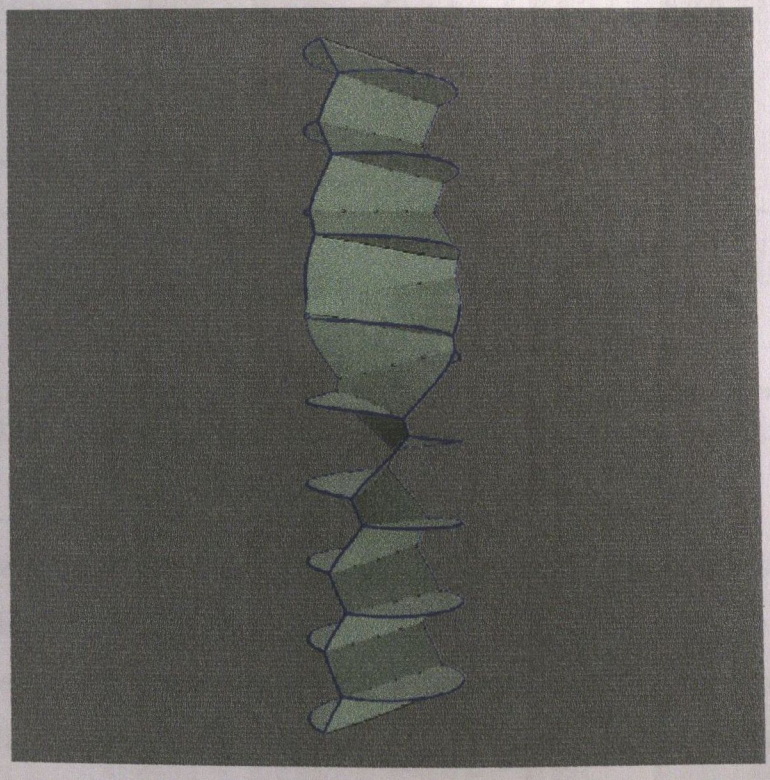

Figure 2.10: A rotational twist may be applied to a 211 structure. The energy dependence of the structure on twist angle is generated using the *Surface Evolver*.

One possibility is that the surface energy of a 211 structure is minimal at some non-zero twist angle. We calculated its energy as the twist angle

was altered, Figure 2.11. Clearly the energy is a quadratic function with

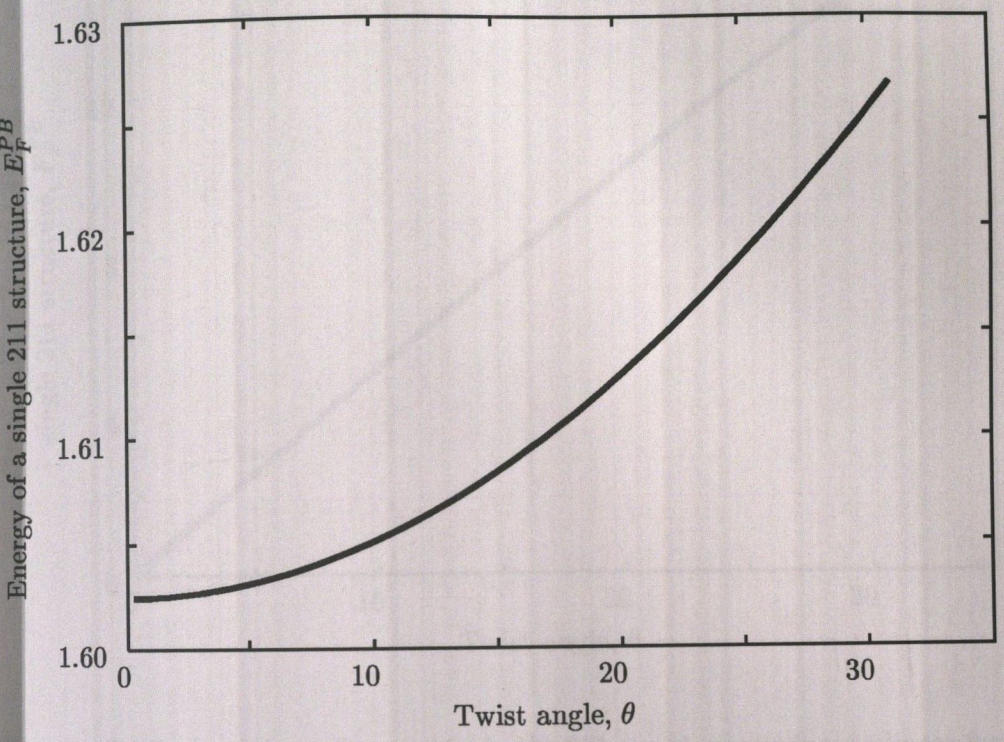

Figure 2.11: The energy of a dry 211 structure, $\Phi_l = 0$, varies quadratically with twist angle, θ, disproving the idea of a local energy minimum at some non-zero twist angle.

minimum energy at zero twist angle. A quadratic response in energy suggests the application of a linear force giving rise to the twist effect. The rate of change of energy (force) with twist angle θ is calculated and shown in Figure 2.12. The linear relationship between F and θ suggests the structure is identical to a simple spring model where each bubble is a mass connected to it nearest neighbour via a Hooke spring.

In further numerical experiments the minimum energy of a large sample of 211 bubbles, with a region of ten bubbles fixed with a uniform twist angle through 180°, was calculated, Figure 2.13. The fixed constraint on the twist

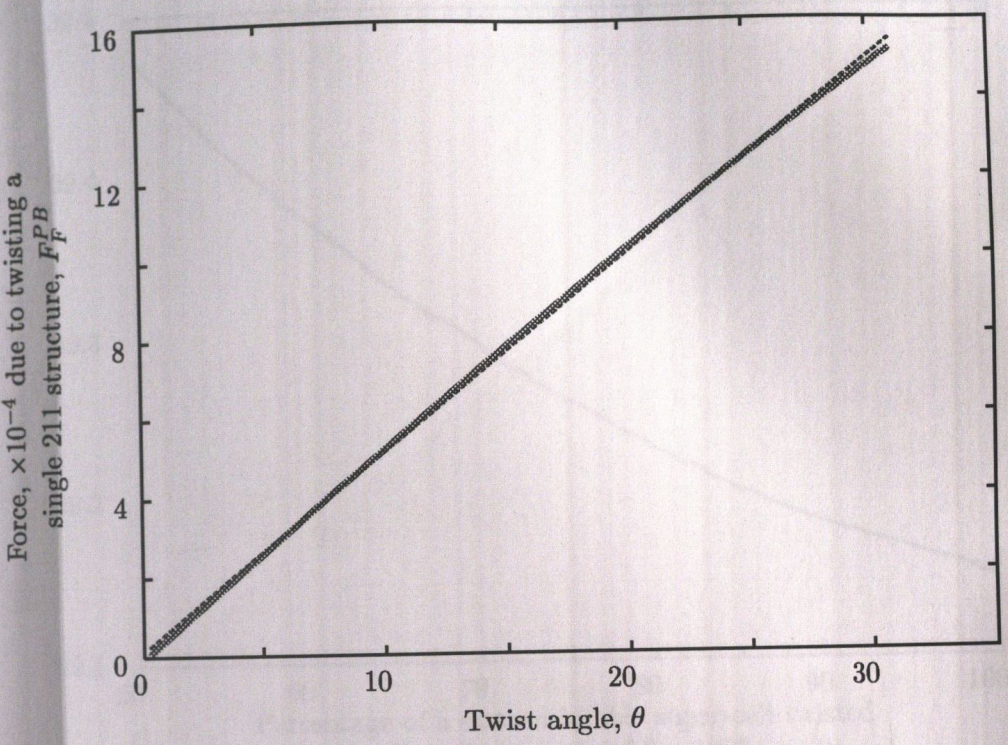

Figure 2.12: Applying a linear twist in the 211 structure produces a linear force. Numerical data - solid line, linear fit - dotted line.

angle was removed and the minimum energy recalculated. The structure clearly reached minimum energy once the twist had unwound and uniformly distributed itself through the entire sample. This contradicts the somewhat inconclusive results found by Phelan [14].

2.4.5 Twist angle dependence on λ

Structures such as 321, Figure 2.5, and 431 contain three and four bubbles respectively per unit cell. These unit cells, rotated through some *unknown* spiral boundary angle θ, stack one atop the other to build the structure. 321 is commonly observed in experiments of the type describe by Pittet *et al.*

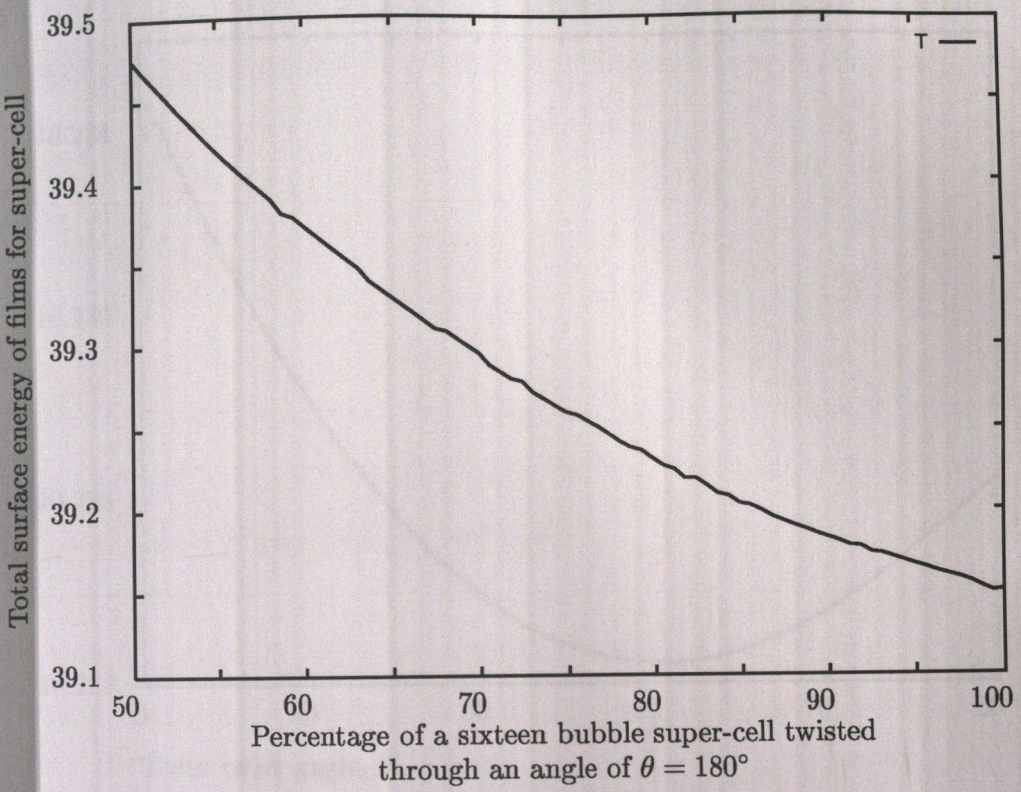

Figure 2.13: A uniform twist, of 180°, initially applied over part of a 211 super-cell, will seek to minimise total surface energy by spreading out over the entire structure.

[29]. The large range of stability of 321, Table 2.1, suggests that its twist angle θ may be dependent on λ.

By altering λ, within the stable region of the structure, Table 2.1, we recalculate the minimum energy of 321 and find the value of θ_{min} at this energy.

Numerical experiments show that as λ changes, the twist angle θ is altered to minimise surface energy, making the structure more stable. Therefore, θ is not fixed for spiraling structures, i.e. structures where $m \neq 0$ and $m \neq l$. Figure 2.14 shows how the energy of 321 varies with twist angle θ for $\lambda = 1.3$. The structure has a minimum energy at $\theta = 60°$.

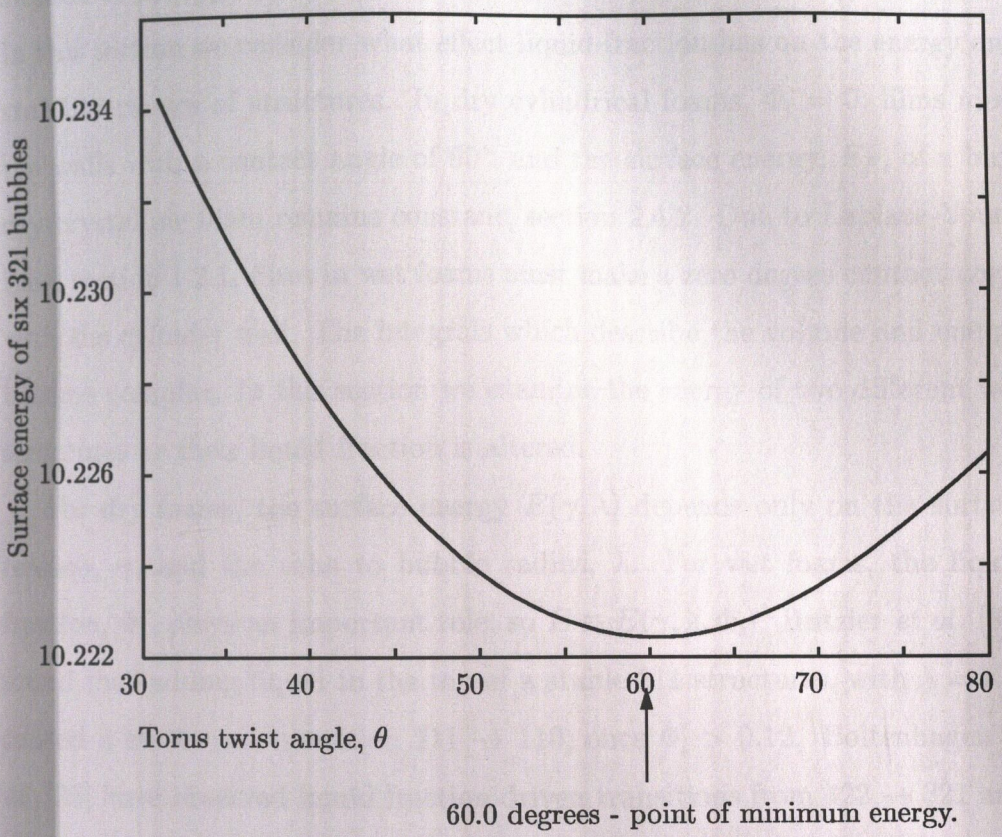

Figure 2.14: The minimum energy of the 321 structure for $\lambda = 1.3$ is dependent not only on λ, but also on a twist angle θ.

Reinelt *et al.* [22] have calculated and explained the structural transition from 211 to 110. It seems possible that the twist angle, θ, plays some role in the route to structural instability from $321 \rightarrow 211$.

2.5 Wet structures

Many experiments involve the use of 'wet foams', that is, foams where the liquid fraction is not insignificant. In wet foams the Plateau borders are

swollen to an appreciable size - this is discussed further in Chapters 4 and 7. In this section we consider what effect liquid fraction has on the energy and stability ranges of structures. In dry cylindrical foams, $\Phi_l = 0$, films meet the walls with a contact angle of 90°, and the surface energy, E_F, of a bulk dry crystalline foam remains constant, section 2.4.2. Due to Laplace-Young Law, section 1.2.1, films in wet foams must make a zero degree contact angle with the cylinder wall. The integrals which describe the volume and energy become complex. In this section we examine the energy of two different wet structures as their liquid fraction is altered.

For dry foams, the surface energy $E(\gamma, \lambda)$ depends only on the surface tension, γ, and the tube to bubble radius, λ. For wet foams, the liquid fraction, Φ_l, plays an important role, so $E \equiv E(\gamma, \lambda, \Phi_l)$. Hutzler *et al.* [37] found that adding liquid to the top of a stable 211 structures, with $\lambda = 1.3$, caused a structural transition 211 $\rightarrow$ 110, once $\Phi_l > 0.12$. Boltenhagen *et al.* [35] have observed liquid fraction driven transitions from 422 $\rightarrow$ 321 and offer theoretical explanations.

We simulated the conditions observed by Hutzler *et al.* with $\lambda = 1.3$ for 211 (*Evolver* data file provided by Brakke [40]) and 110 crystalline structures, Figure 2.15. These structures are generated using a 'facet' model of the surfaces, i.e. the volumes of the bubbles, not shown, are calculated using surface and line integrals. There is no automated way of generating *Evolver* datafiles for wet foams with cylindrical constraints. Plateau borders have to be added in by hand with complex integrals to account for their volume and energy contributions, these are discussed in detail in section 7.3.

In the 110 structure, the Plateau border joins the central blue film and the cylinder wall - which are shown in Figure: 2.15 (Left). As the liquid fraction increases the energy of the structure decreases. When $\Phi_l \approx 0.36$, the close

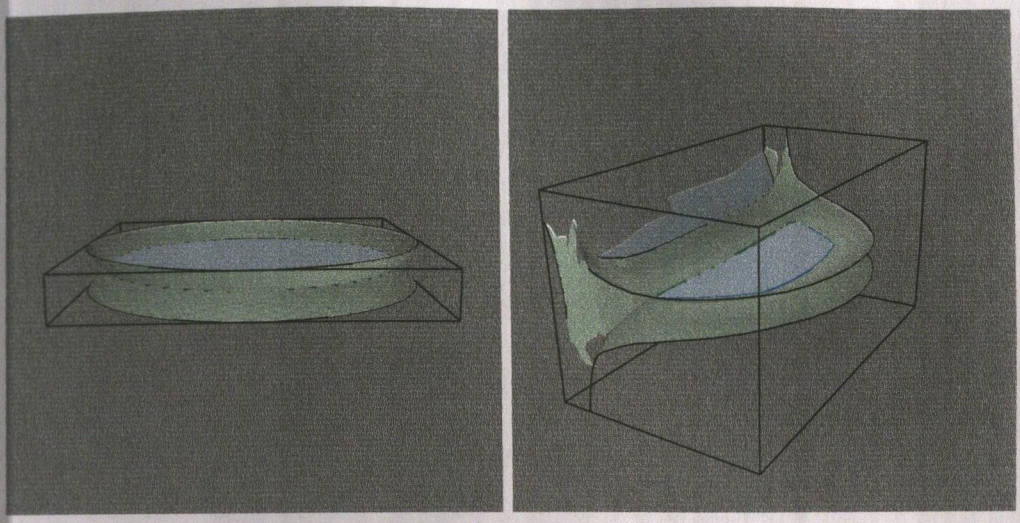

Figure 2.15: Wet crystalline structures where $\Phi_l = 3\%$. (Left) a wet 110 structure, (Right) a wet 211 structure. The green films show liquid-film interfaces where $\gamma = 1$, the blue films show film-film interfaces where $\gamma = 2$. The energy and area contribution due to faces on the surface of the cylinder is calculated using surface and line integrals on the edges on the cylinder surface. The 110 structure repeats periodically through a translation of height h in the z-direction. The 211 structure repeats periodically through a translation of height $\frac{h}{2}$ in the z-direction and a rotation of 180°.

packing limit, the bubble of unit radius will be spherical with energy ~ 4.836 - far less than that of Kelvin. Minimising these *Evolver* structures is a time consuming and difficult process. Problems such as facet overlapping occur - the *Evolver* is not able to detect this. Facet overlapping occurs when two curved surfaces meet at a line with zero contact angle between them and the tessellation is too coarse to handle the strict zero contact angle condition. The problem may be overcome by evolving with a non-zero contact angle until a sufficiently refined tessellation is obtained. *Evolver* simulations of wet foams are shown in Figure 2.16 and Figure 2.17.

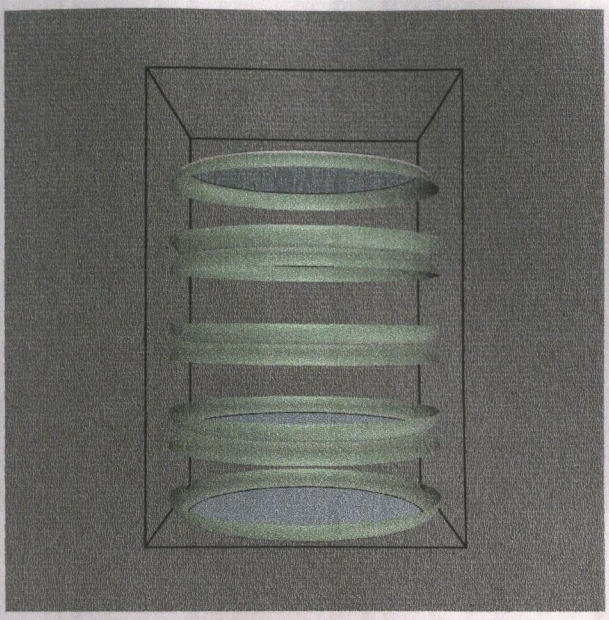

Figure 2.16: The bamboo structure repeats periodically in the z-direction. The films on the surface of the cylinder have been removed. The blue films correspond to film-film interfaces where $\gamma = 2$. The green films correspond to liquid-film interfaces where $\gamma = 1$, and all the liquid is contained within the green films and the cylinder surface.

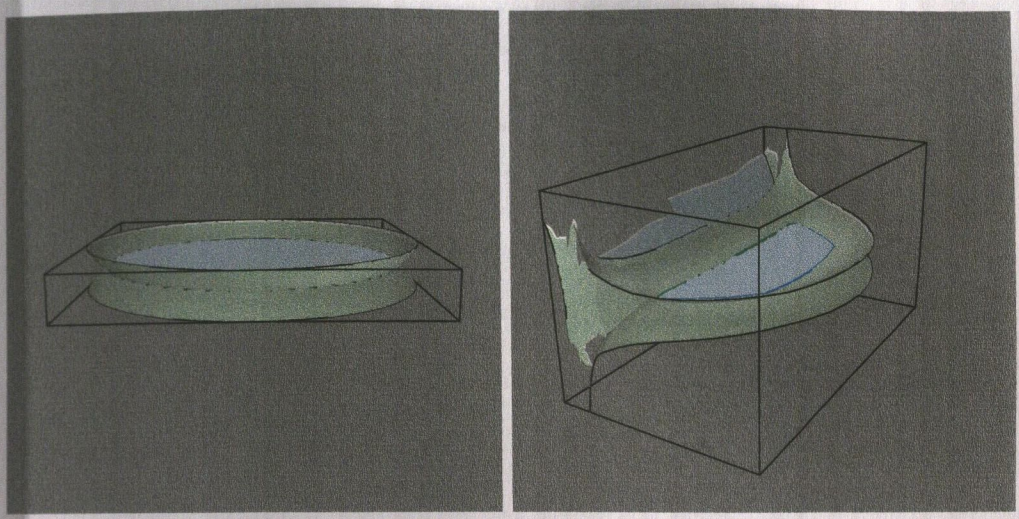

Figure 2.15: Wet crystalline structures where $\Phi_l = 3\%$. (Left) a wet 110 structure, (Right) a wet 211 structure. The green films show liquid-film interfaces where $\gamma = 1$, the blue films show film-film interfaces where $\gamma = 2$. The energy and area contribution due to faces on the surface of the cylinder is calculated using surface and line integrals on the edges on the cylinder surface. The 110 structure repeats periodically through a translation of height h in the z-direction. The 211 structure repeats periodically through a translation of height $\frac{h}{2}$ in the z-direction and a rotation of 180°.

packing limit, the bubble of unit radius will be spherical with energy ~ 4.836 - far less than that of Kelvin. Minimising these *Evolver* structures is a time consuming and difficult process. Problems such as facet overlapping occur - the *Evolver* is not able to detect this. Facet overlapping occurs when two curved surfaces meet at a line with zero contact angle between them and the tessellation is too coarse to handle the strict zero contact angle condition. The problem may be overcome by evolving with a non-zero contact angle until a sufficiently refined tessellation is obtained. *Evolver* simulations of wet foams are shown in Figure 2.16 and Figure 2.17.

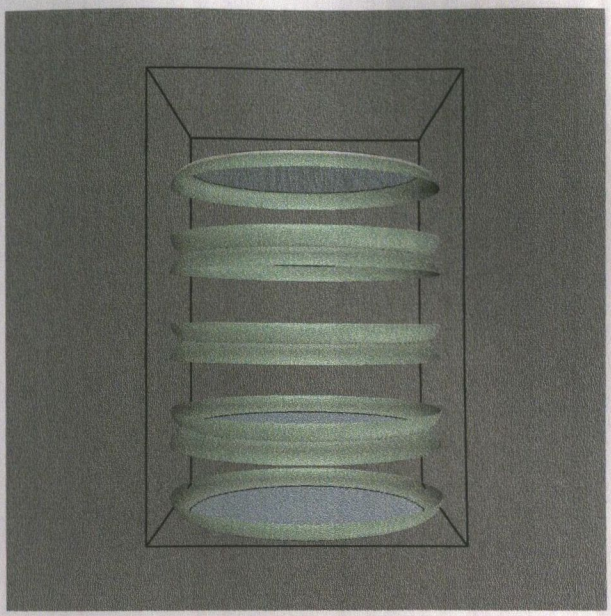

Figure 2.16: The bamboo structure repeats periodically in the z-direction. The films on the surface of the cylinder have been removed. The blue films correspond to film-film interfaces where $\gamma = 2$. The green films correspond to liquid-film interfaces where $\gamma = 1$, and all the liquid is contained within the green films and the cylinder surface.

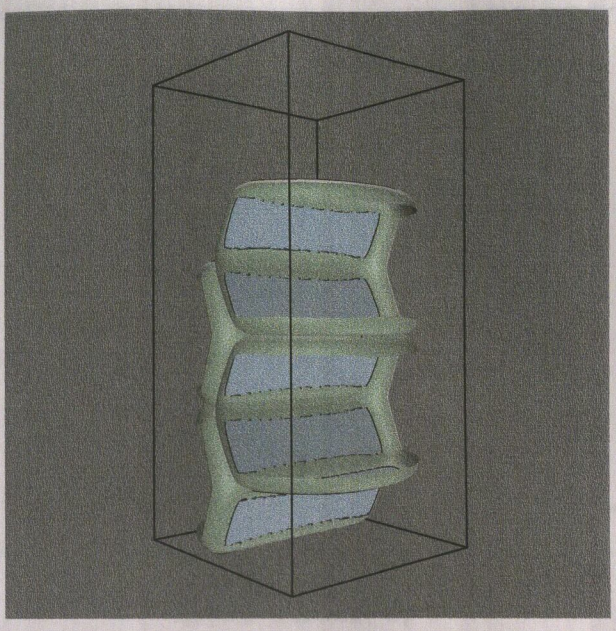

Figure 2.17: The 211 structure repeats periodically in the z-direction. The films on the surface of the cylinder have been removed. The blue films correspond to film-film interfaces where $\gamma = 2$. The green films are the Plateau borders and correspond to liquid-film interfaces where $\gamma = 1$. All the liquid is contained within the green films and the cylinder surface.

When the liquid fraction is varied, it is convenient to fit the results to theoretical expansions of the kind discussed in section 1.2.4, i.e.

$$E = a - b\Phi_l^{\frac{1}{2}} - c\Phi_l$$

For the bamboo (110) structure: a = 5.88, b = 2.5, c = 1.7 and for the 211 structure: a = 6.56, b = 2.6, c = 2.3, Figure 2.18.

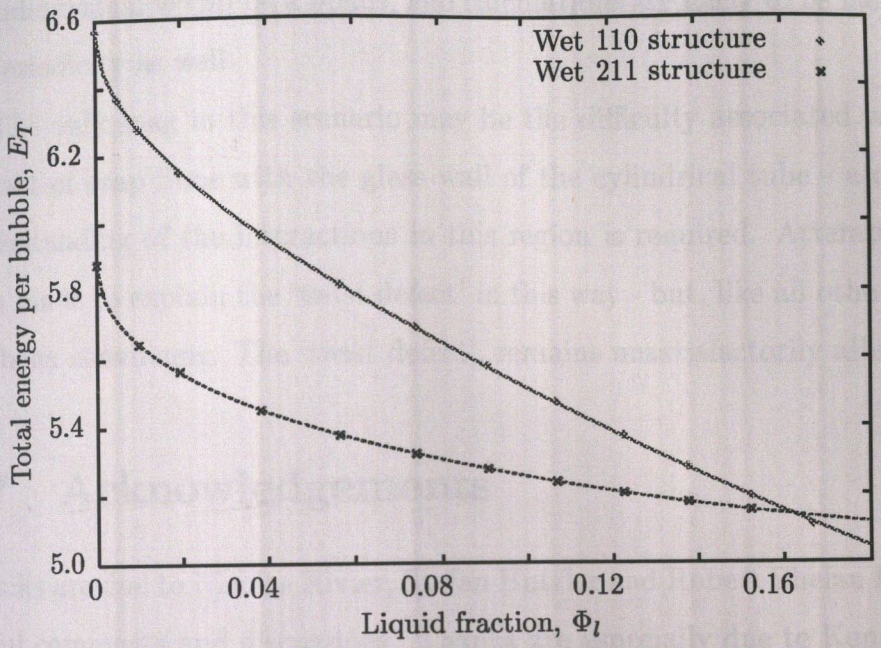

Figure 2.18: The variation of surface energy with liquid fraction for 211 and bamboo structures indicates a topological transition at $\Phi_l \simeq 0.16$. Data points from *Surface Evolver* calculations are fitted to the theoretical energy expansion outlined in section 1.2.4: $E_T = a - b\Phi_l^{\frac{1}{2}} - c\Phi_l$

2.6 Conclusions

Comparisons between numerical and experimental data show that the *Surface Evolver* is a valuable tool capable of accurately describing the properties of 'wet' and 'dry' crystalline cylindrical foam structures.

The potential use of ordered crystalline structures as a testbed for the study of basic foam properties should not be underestimated. In particular, the future utility of these calculations probably lies in the use of some of the structures to test theoretical notions about the dynamics which underlies the rheology of foams. The local processes of topological rearrangement lie at the heart of this problem. To be able to view them occurring repetitively in a

periodic system would be a bonus, and calculations are likely to be facilitated by periodicity as well.

The only snag in this scenario may be the difficulty associated with the contact of soap films with the glass wall of the cylindrical tube - a detailed understanding of the interactions in this region is required. Attempts have been made to explain the 'twist defect' in this way - but, like all others, have not been convincing. The 'twist defect', remains unsatisfactorily alluring.

2.7 Acknowledgements

Thanks are due to Nicolas Rivier, Stefan Hutzler and Robert Phelan for their useful comments and discussions. Thanks are especially due to Ken Brakke for writing the *screw_symmetry* group in the *Surface Evolver*, for providing some of the *Evolver* input datafiles and for his help with all aspects of the *Surface Evolver*.

Chapter 3

Liquid instabilities

In experimental studies of two non-coalescing liquid drops, Monti [42] and co-workers encountered an instability as the drops were pressed together. At the point of instability the two drops move sideways to avoid each other, thus breaking the cylindrical symmetry of the system.

The Surface Evolver is used to simulate this instability numerically by assuming that such instabilities are attributable to minimisation of surface area under a uniform surface tension. Eigenvalue analysis of the variation of the calculated surface energy is used to detect the point of instability as the drop separation distance is altered.

3.1 Introduction

When two liquid drops of identical mass and liquid are brought into close contact they will generally coalesce. However recent experiments [43, 44] have shown that under certain conditions coalescence does not occur, each drop maintains its integrity.

This discovery was the result of an experiment performed in the mi-

crogravity environment of space. During the course of the experiments all attempts to reform a broken liquid bridge were unsuccessful. Pushing the separated drops into close contact did not cause coalescence to occur, Figure 3.1.

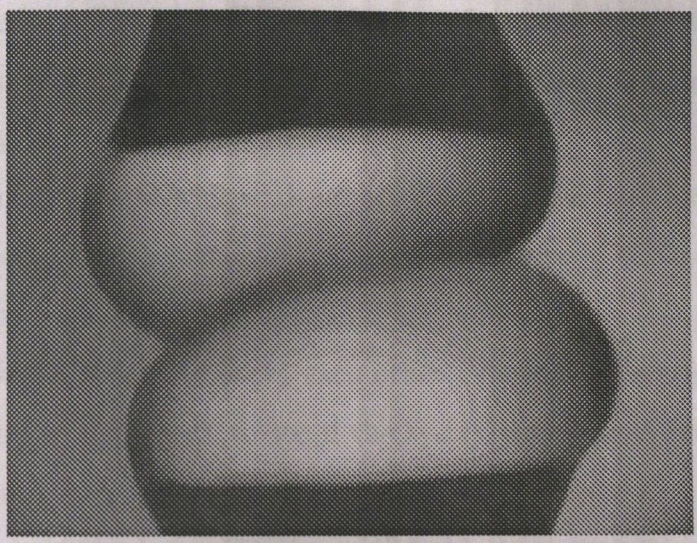

Figure 3.1: Photograph of the instability as seen experimentally. The two drops move out of each others' way to reduce the total energy of the system. (Courtesy of R. Monti.)

This phenomenon is not new. It was studied in detail by many eminent 19th century physicists - most notably Reynolds and Rayleigh. More recently it has been studied by Dell'Aversana and Neitzel [45] and by Valkovska *et al.* [46]. It is also related to 'double bubbles' or 'anti-bubbles' as reported by Strong [47] and Skogen [48].

Theoretical and numerical studies of the space experiment, by Monti *et. al* [49] and Monti and Savino [50], concluded that the non-coalescence was associated with a temperature difference between the two drops. It is assumed that the upper drop is hotter than the lower drop - but it is slightly colder in it's centre and the colder drop is slightly hotter in it's centre. This

gives rise to a temperature gradient which is counteracted by the surface tension. The end result is the continuous flow of liquid on the drops surface, known as Marangoni flow, and a flow of air into and back out of the region between the two drops. It is this flow of air that prevents coalescence. The numerical studies of Monti and co-workers produced a fluid mechanics model of the system described by the continuity and Navier-Stokes equations and the conservation of energy, [50, 51].

This process is now well understood - however we are interested in a different aspect of the experiment. During the course of the experiment an instability occurred, breaking the cylindrical symmetry of the system as the droplets moved sideways to avoid each other. We wish to study the physics of this instability and check to see if the system should exhibit any further instabilities as the drops are brought into yet closer contact.

In as much as the instability is attributable to surface tension acting in equilibrium, we need not be concerned with any of the subtle fluid dynamics of the earlier theoretical analysis. We take non-coalescence for granted, and explore the equilibrium of the two contact drops of incompressible liquid, each with a constant surface tension γ. Gravity is not included.

3.2 Geometrical parameters

Within the stated model, only a few geometrical ratios are significant. We take for simplicity only the case of two liquid drops of equal volume V, attached to two circular disks of diameter D, separated by a distance d, Figure 3.2. The problem may be specified by the two dimensionless ratios

$$\lambda = \frac{V}{D^3} \tag{3.1}$$

$$\mu = \frac{d}{D} \tag{3.2}$$

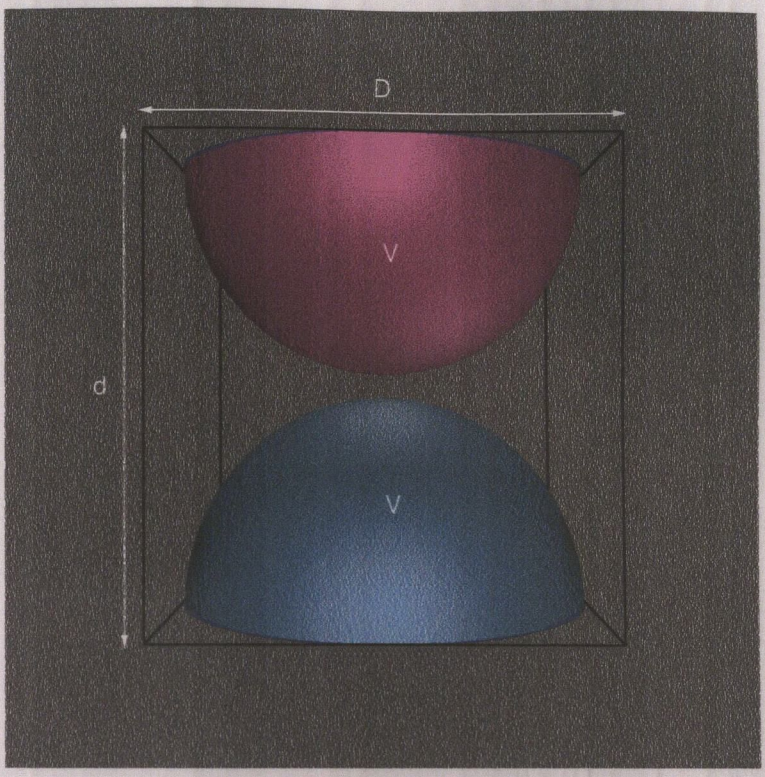

Figure 3.2: The initial setup of the system shows two liquid drops of volume V, fixed to rings of diameter D. They are separated by a distance d, which is progressively reduced to bring the drops into contact with each other.

The energy of the system is given in terms of the total surface area, S, of the bubbles, as

$$E = \gamma S \tag{3.3}$$

By setting $\gamma = 1$ we may write equation 3.3 in dimensionless form

$$\hat{E}(\lambda, \mu) = \frac{S}{D^2} \tag{3.4}$$

so that the goal of our simulation is to determine $\hat{E}(\lambda, \mu)$ and the corresponding bubbles shapes for stable equilibria, and hence to identify the points of instability.

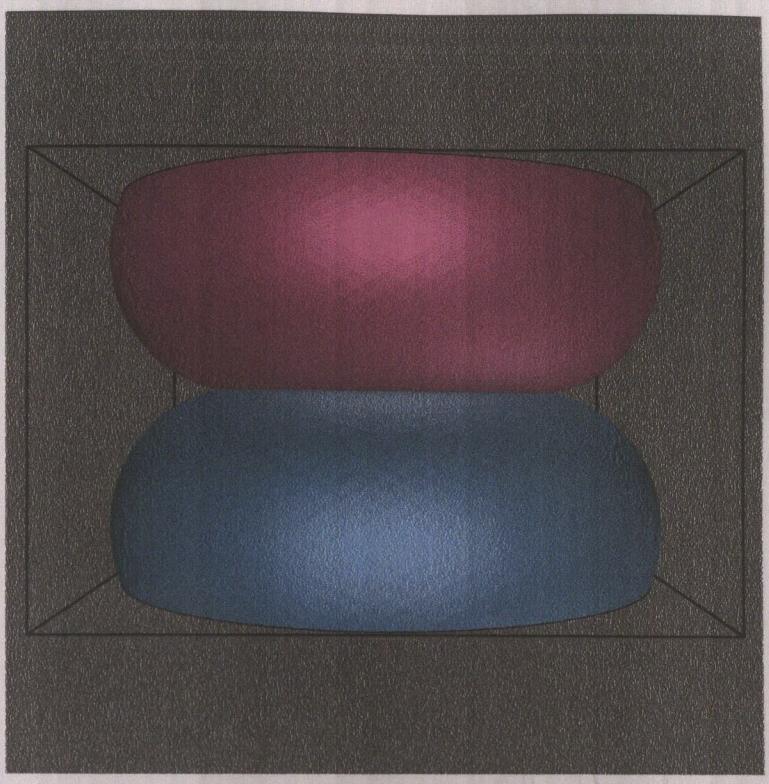

Figure 3.3: When two non coalescing liquid drops are brought into contact, they initially retain cylindrical symmetry and have a circular surface of contact.

3.3 Calculation details

Problems of this kind may be addressed using the *Surface Evolver* program developed by K. Brakke [13, 52]. This represents the curved surface of the two drops in terms of a tessellation which is progressively refined to obtain the required accuracy.

The general workings of the *Surface Evolver* are detailed in Chapter 7. Here we concentrate on the program's ability to detect instabilities, as this is crucial to understanding the methodology of this chapter.

The *Surface Evolver* parameterises a surface in terms of its vertex coordinates. Let $\tilde{\mathbf{x}}$ be an N-dimensional vector of all vertex coordinates for a

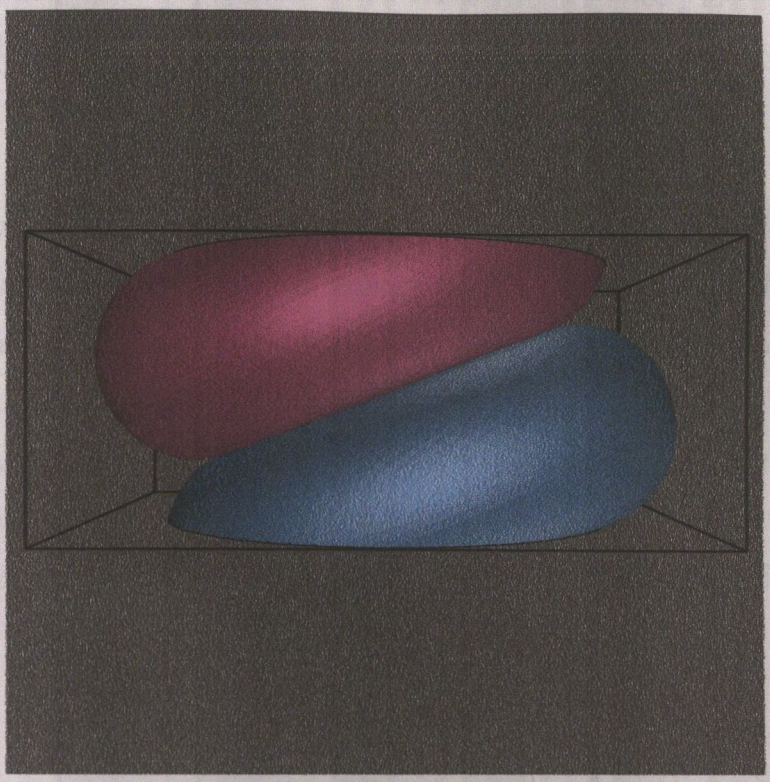

Figure 3.4: As two drops are pressed close together a critical separation distance, d_c, is encountered. Pressing the drops still closer together causes the cylindrical symmetry of the system to be broken as the drops distort moving out of each other way. The surface of contact between the two drops becomes elliptical from this point on.

particular triangulation, $\mathcal{T}$. $\tilde{\mathbf{x}}$ is called the configuration vector and inhabits an N dimensional configuration space. The total energy of the surface $E(\tilde{\mathbf{x}})$ is a scalar function on configuration space.

A surface is unstable if it's energy is far from a local minimum point. Applying a small perturbation to the surface will result in a large increase in energy. Conversely, when a surface is close to a local energy minimum it becomes stable, and applying a small perturbation allows the surface to move closer to its minimum energy. This is the science of perturbation theory [53].

Consider a particular triangulation $\mathcal{T}$ with energy $E(\tilde{\mathbf{x}}) = E_0$. Applying a

small perturbation $\tilde{\mathbf{y}}$ to $\mathcal{T}$ produces a new surface with energy approximated by Taylors theorem

$$E(\tilde{\mathbf{x}}+\tilde{\mathbf{y}}) = E_0 + \tilde{\mathbf{g}}^T\tilde{\mathbf{y}} + \frac{1}{2}\tilde{\mathbf{y}}^T\mathbf{H}\tilde{\mathbf{y}} + \dots \tag{3.5}$$

$\tilde{\mathbf{g}}$ is the vector of first derivatives - the local gradient of the surface and the best linear approximation to its energy. $\mathbf{H}$ is a square matrix of second derivatives called the *Hessian* and is the best quadratic approximation of the local surface. If all the second derivatives of energy are positive, then the surface is stable. Furthermore, if the quadratic approximation to the surface is good, we are close to a local minimum energy, E_{min}. An equilibrium point is found by solving for motion $\tilde{\mathbf{y}}$ that makes the energy gradient, as a function of y, zero.

$$\nabla E = \tilde{\mathbf{g}}^T + \tilde{\mathbf{y}}^T\mathbf{H} \tag{3.6}$$

$$\tilde{\mathbf{g}} + \mathbf{H}\tilde{\mathbf{y}} = 0 \tag{3.7}$$

$$\tilde{\mathbf{y}} = -\mathbf{H}^{-1}\tilde{\mathbf{g}}. \tag{3.8}$$

Then

$$E(\tilde{\mathbf{x}}+\tilde{\mathbf{y}}) \approx E_0 - \frac{1}{2}\tilde{\mathbf{y}}^T\mathbf{H}\tilde{\mathbf{y}} \tag{3.9}$$

so

$$E(\tilde{\mathbf{x}}+\tilde{\mathbf{y}}) - E_{min} < E(\tilde{\mathbf{x}}) - E_{min} \tag{3.10}$$

i.e. the energy of the new surface is closer to the minimum energy. This is one iteration of the Newton-Rapson method - as described by Killingbeck [53] and Brakke [54]. Several iterations of the Newton-Rapson method will swiftly converge the surface energy to a local minimum.

The Hessian matrix $\mathbf{H}$ may be diagonalised by an orthogonal change of basis of the configuration space. The new basis vectors are eigenvectors and

each represents a particular perturbation of the surface. The energy cost of such a perturbation corresponds the magnitude of its eigenvalue, in **H**. By analysing the lowest eigenvalues of a stable configuration we may determine whether the surface is near an instability point.

The specific calculation details for this case are outlined in Chapter 7, section 7.4.

3.4 Results

We first consider the case when the normalised volume parameter $\lambda = 0.262$, which corresponds to two initially hemispherical drops of unit volume. Contact is established for $\mu^{-1} = 1.0$, and a flat circular surface of contact forms between the two drops as they are pressed together, Figure 3.3. An instability is encountered at $\mu^{-1} = 1.53$. The instability causes the axial symmetry of the system to be broken, Figure 3.4. Beyond this point the surface of contact between the two drops becomes roughly flat and elliptical. Identifying the two points at the ends of the major axis of the ellipse, we take the separation of their position in the direction of the cylindrical axis as a convenient measure of the distortion. We normalise this quantity by dividing by D, and we call it J. Its computed variation is shown in Figure 3.5. The distortion J is seen to vary linearly with the square of the drop separation d. The instability is plainly of the classical symmetry-breaking variety, typified by Euler buckling of beams, which exhibits a square root variation in such a plot. Theory of instability analysis based on lowest order energy expansion predicts a slope ratio above and below the point of instability as 1 : -2. This relationship is well satisfied by results in Figure 3.6.

The calculation of eigenvalues of the system just before the onset of the

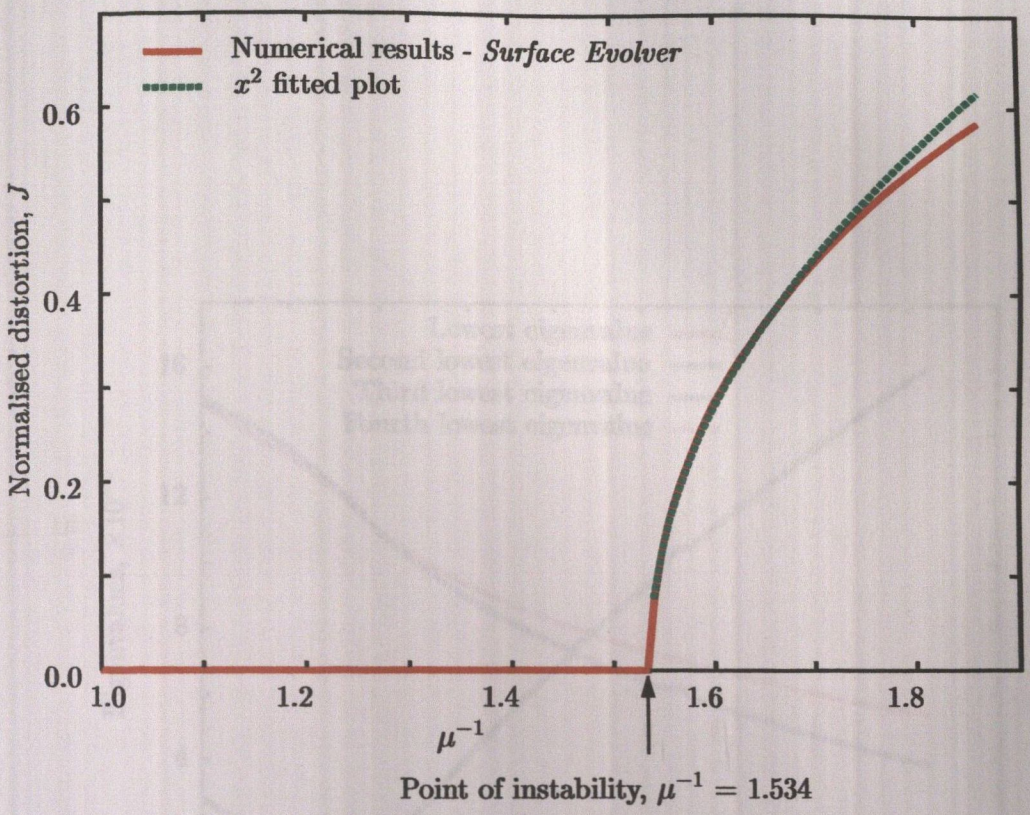

Figure 3.5: The solid curve shows the increase in normalised drop distortion J as the liquid drops are brought into closer contact (μ^{-1}). It is well approximated by a square root function (dashed curve).

instability confirms the double degeneracy of the lowest one. This arises because the direction of distortion is arbitrary. A plot of the lowest eigenvalues can be seen in Figure 3.5.

The value of λ was then altered so the initial drops had greater volume. The point of instability for each new value of λ can be seen in Figure 3.7.

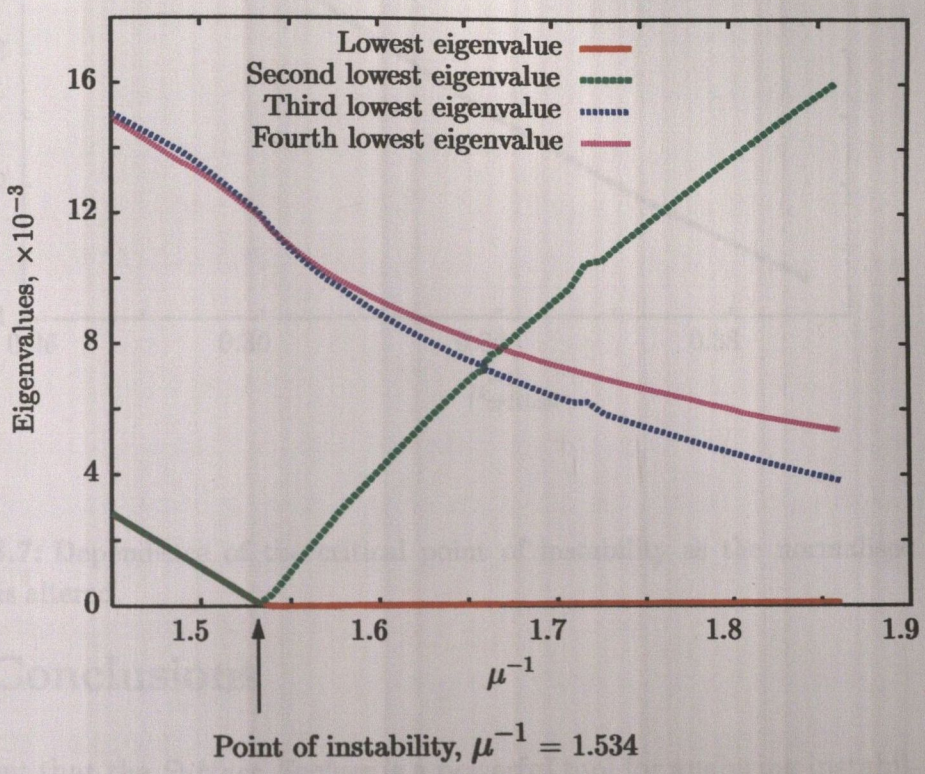

Figure 3.6: Prior to the point of instability the system can be seen to exhibit degeneracy of its two lowest eigenvalues (red and green curves). Degeneracy is lost as the distance between the two drops (μ^{-1}) is reduced beyond the point of instability.

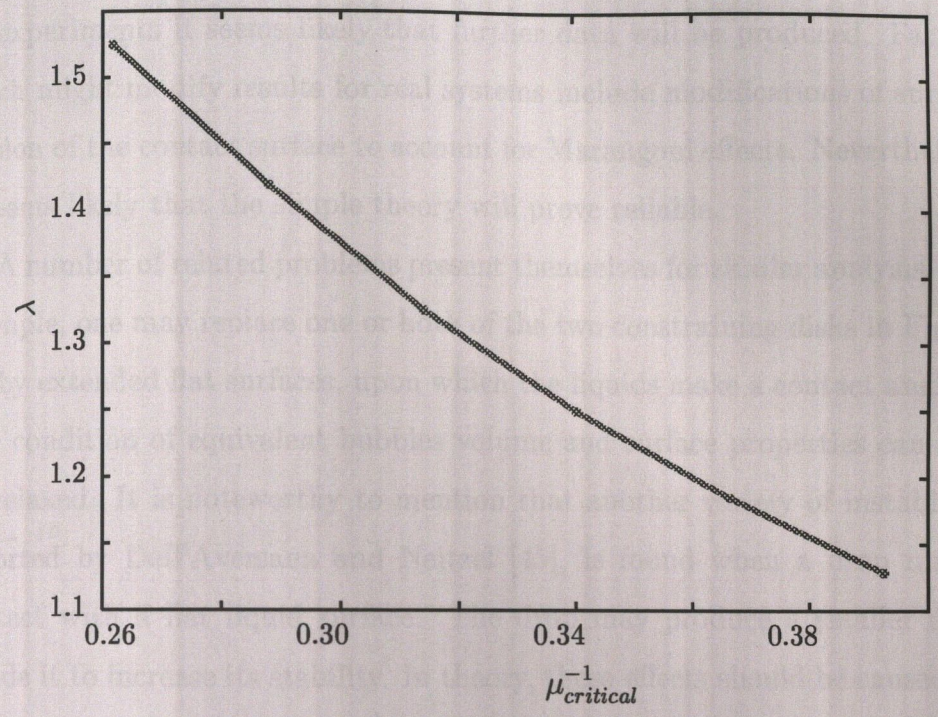

Figure 3.7: Dependence of the critical point of instability as the normalised volume λ is altered.

3.5 Conclusions

It is evident that the *Surface Evolver* is a powerful tool for analysing instabilities of this nature, yet there is little evidence that the scientific community is using it in this context. To that end, a key achievement of these calculations may simply be to inform others of the *Evolver's* potential - Bradley and Weaire [18]. However, applications of the Hessian methods are far from straight forward and there are some small unexplained eigenvalue effects (at $\mu \approx 1.72$ - Figure 3.6) which may require further analysis. It seems likely that they are due to the finite nature of the surface tessellation.

At present, there is no detailed experimental data available for comparison

with these results or predictions, but given the current interest in microgravity experiments it seems likely that further data will be produced. Factors which might modify results for real systems include modifications of surface tension of the contact surface to account for Marangoni effects. Nevertheless, it seems likely that the simple theory will prove reliable.

A number of related problems present themselves for similar analysis. For example, one may replace one or both of the two constraining disks in Figure 3.2 by extended flat surfaces, upon which the liquids make a contact angle θ. The condition of equivalent bubbles volume and surface properties can also be relaxed. It is noteworthy to mention that another variety of instability, reported by Dell'Aversana and Neitzel [45], is found when a drop makes contact with a flat liquid surface. The drop may produce a smaller drop beside it to increase its stability. In theory, these effects should be caused by surface tension forces and therefore reproducible using the *Surface Evolver*.

In addition to their intrinsic interest, such experiments and theory are also relevant to emerging technologies in which fluid structures are created on a microscopic scale. One such example is the stability of microscopic droplets and channels forming on homogeneous and structure surfaces, as described by Lenz and Lipowsky [55]. Many kinds of elementary instability, such as those analysed here, have a role to play in that field. The flexibility of the *Surface Evolver* makes it a likely candidate for use in the study of these instabilities.

3.6 Acknowledgements

Thanks are due to Ken Brakke for his help with aspects of the *Surface Evolver*. The *Surface Evolver* Hessian section is based largely on Brakke's

Hessian tutorial [54]. Thanks also to the European Space Agency and Professor Monti for providing Figure 3.1.

Chapter 4

Vertex Corrections

4.1 Introduction

In this chapter we study some of the basic properties of wet foams. In particular, we find the shape, volume and transport parameters of Plateau borders and tetrahedral junctions in a wet foam.

To do this we must be able to describe the geometrical structure of localised foam, as this structure determines the physical properties of interest. In particular we isolate a single Plateau border and a single tetrahedral junction and perform an accurate analysis of their geometry using the *Surface Evolver*.

Furthermore, we seek to move away from the traditional analysis of static wet foam calculations by combining two unique numerical tools, the *Surface Evolver* and *Fluent*, to analyse the effects of liquid drainage at a localised, single tetrahedral junction level.

4.2 Theory and Calculations

An 'idealised' dry foam, $\Phi_l = 0$, is simply a collection of polyhedral cells, e.g. Kelvin's tetrakaidecahedra, bounded by two dimensional curved walls. It is subject to the Laplace-Young law, section 1.2.1, and when in equilibrium, to Plateau's rules, section 1.2.2. As the liquid fraction, Φ_l, increases, the lines and vertices of the idealised dry foam swell and the foam becomes *wet*, Figure 1.4, Chapter 1. The wet foam then obeys some additional rules, section 1.2.3.

The swollen lines form Plateau borders with length L and asymptotic width δ. The cross sectional area of a Plateau border, Figure 4.1, is

$$A_{Pb} = c_g \delta^2 \text{ where } c_g = \left(\sqrt{3} - \frac{\pi}{2}\right)$$

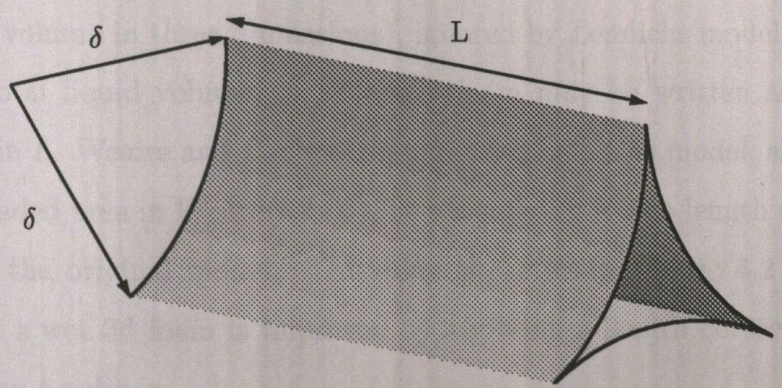

Figure 4.1: A single straight Plateau border with uniform cross-sectional area A_{Pb}, and length L, generated using the *Surface Evolver*.

In Lemlich's model [56], a three dimensional wet foam is made up of long straight Plateau borders of length L and uniform cross section area A_{pb}, meeting four at a time at idealised tetrahedral junctions. Each Plateau border contributes a liquid volume, $V_{Pb} = LA_{Pb}$, to the foam. At low liquid fractions it is assumed the junctions play a small or insignificant role in

determining the physical parameters of the foam. The volume of an idealised foam with n junctions is simply

$$V = 4\sum^{n} A_{Pb} L \tag{4.1}$$

However, the role junctions play in altering the properties of a foam is seen by considering the simplified case of a two dimensional wet foam. In two dimensions, areas replace volumes, and junctions consists of three rather than four Plateau borders - but the principals are the same. In and idealised two dimensional foam, Plateau borders of length L and width δ meet at a junction, Figure 4.2 (A). This is analogous to Lemlichs description of a real 3d foam.

Real foams have minimum surface area in 3d and minimum line length in 2d, Figure 4.2 (B) - the shaded region represents the additional area of each junction (volume in three dimensions), ignored by Lemlichs model.

The total liquid volume, V, of a wet foam may be written as a linear equation in L. Weaire and Phelan [16] extended Lemlichs model, accounting for the shaded area in Figure 4.2 (B), by considering it as a length correction added to the original model. This idea is sketch in Figure 4.2 (C). The volume of a wet 3d foam is improved by applying a length correction, $C_1\delta$, per Plateau border, so

$$V = 4\sum^{n} A_{Pb} (L \pm C_1\delta) \tag{4.2}$$

Lemlich was primarily interested in calculating the electrical resistance of a foam - whereas our primary interest is calculating the liquid flow resistance. The electrical resistance and flow resistance of a real foam depend on L and δ - therefore an idealised model will incorrectly predict these physical properties. The idealised model is enhanced by providing a *length* correction to account for the tetrahedral junctions.

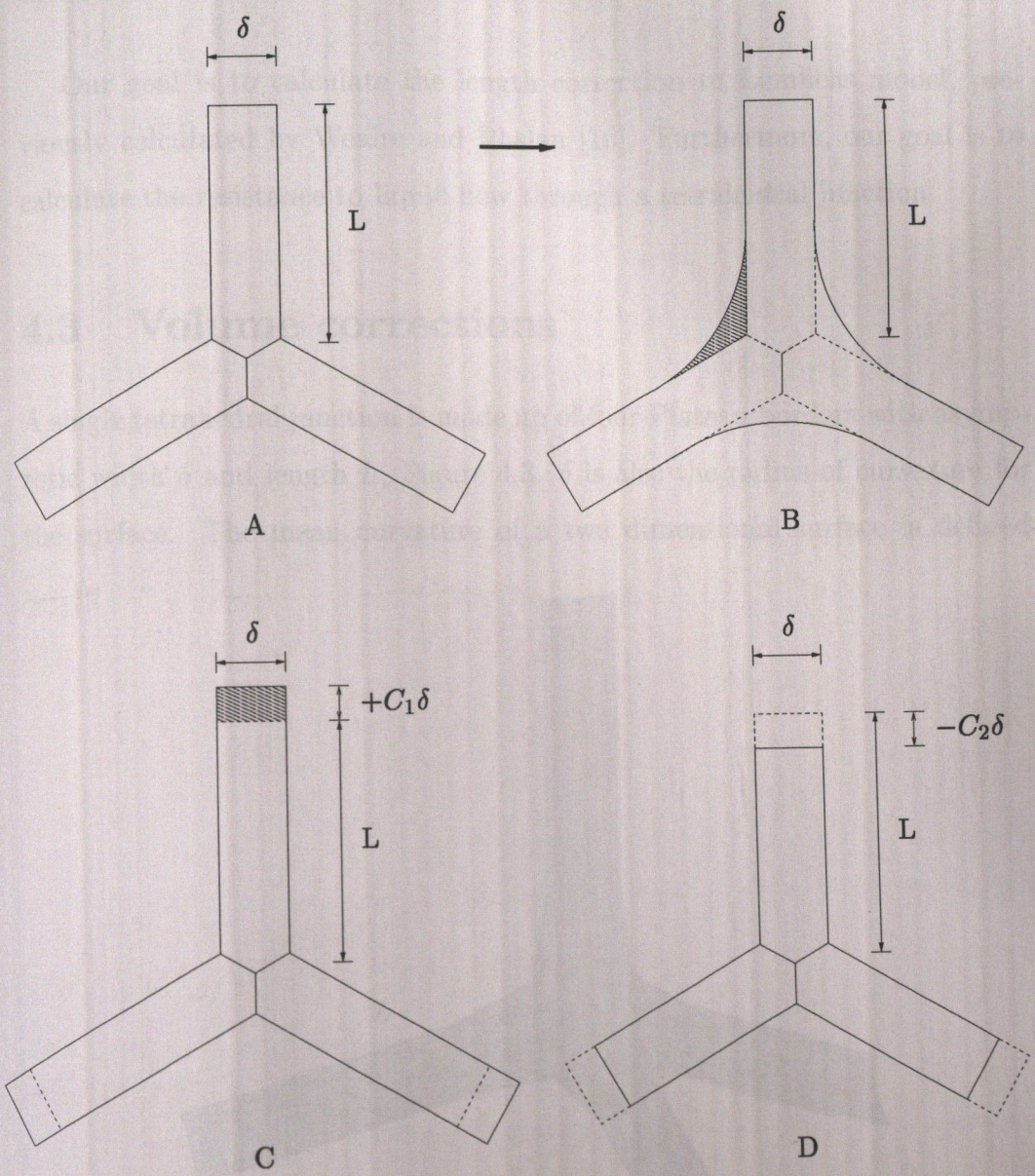

Figure 4.2: A two dimensional junction in a wet foam. In an idealised model, the Plateau borders forming between adjacent foam cells have a uniform width δ and length L, (A). A real foam has minimal line length with shape shown in (B). A wet foam has additional area, per Plateau border, at a junction - shown by the shaded region. This additional area may simply be considered as a correction to the length of a Plateau border, (C), so (B) and (C) represent the same junction. The flow and electrical resistance of a foam may also be consider in terms of an idealised model. An additional length correction accounts for the effects of junctions on these physical properties, (D).

Our goal is to calculate the length correction to Lemlichs model, previously calculated by Weaire and Phelan [16]. Furthermore, our goal is to calculate the resistance to liquid flow through a tetrahedral junction.

4.3 Volume corrections

A single tetrahedral junction is made up of four Plateau borders with asymptotic width δ and length L, Figure 4.3. δ is also the radius of curvature for the surface. The mean curvature of a two dimensional surface is defined

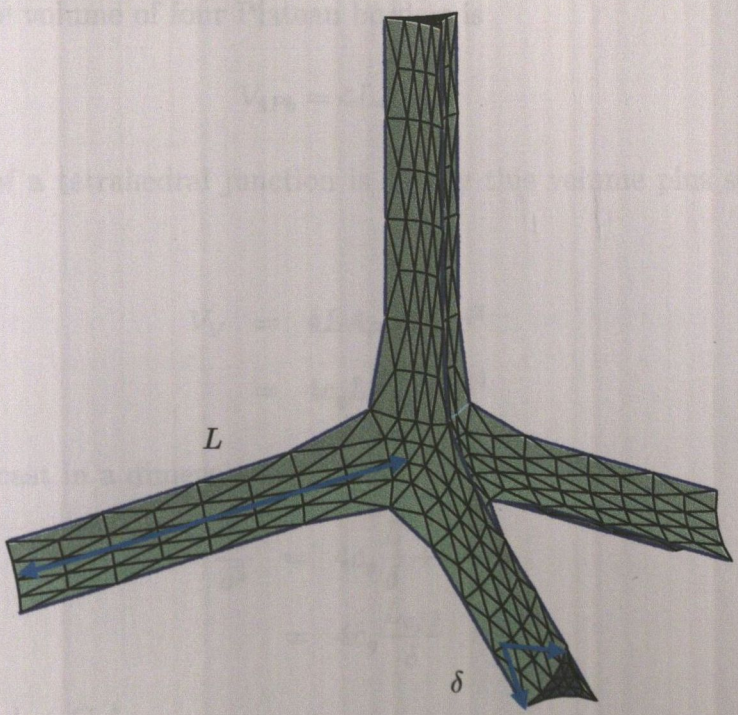

Figure 4.3: A single tetrahedral vertex made up of four Plateau border arms of length L and asymptotic width δ. L is measured to the centre of the junction. Produced using the *Surface Evolver*.

by the Laplace-Young law, section 1.2.1. Its principal radii R_1 and R_2 are

defined by

$$\Delta p = 2\gamma \frac{1}{R_1 + R_2} \tag{4.3}$$

For a tetrahedral junction, and for a single Plateau border, $R_1 = \delta$ and $R_2 \sim \infty$. δ is the radius associated with the mean curvature, $\mathcal{K}$, for the entire surface of a single tetrahedral junction, by the relation $\mathcal{K} = \delta^{-1}$.

The effect of each tetrahedral junction is to contribute an additional amount of volume to each Plateau border, of the order of δ^3, provided $L > \delta$. In the formulation used by Phelan and Weaire [16] the vertex volume may be written as a length correction, L_{eff}, times the Plateau border cross-sectional area, A_{pb}. The volume of four Plateau borders is

$$V_{4Pb} = 4LA_{Pb}.$$

The volume of a tetrahedral junction is simply this volume plus some correction - $C\delta^3$

$$\begin{aligned} V_V &= 4LA_{Pb} + C\delta^3 && (4.4) \\ &= 4c_g L\delta^2 + C\delta^3 && (4.5) \end{aligned}$$

This may be cast in a dimensionless form

$$\begin{aligned} \frac{V_V}{\delta^3} &= 4c_g \frac{L}{\delta} + C && (4.6) \\ &= 4c_g \frac{L_{eff}}{\delta} && (4.7) \end{aligned}$$

where $L_{eff} = L + C\frac{\delta}{4c_g}$.

We seek to verify Phelan's results by calculating the volumes of a tetrahedral junction for various values of L and δ and hence plotting a graph of equation 4.6 to find the value of C. The volume of a single tetrahedral junction is found using the *Surface Evolver*, and Figure 4.4 shows a graph of equation 4.6. Implementation details are provided in section 7.5.1.

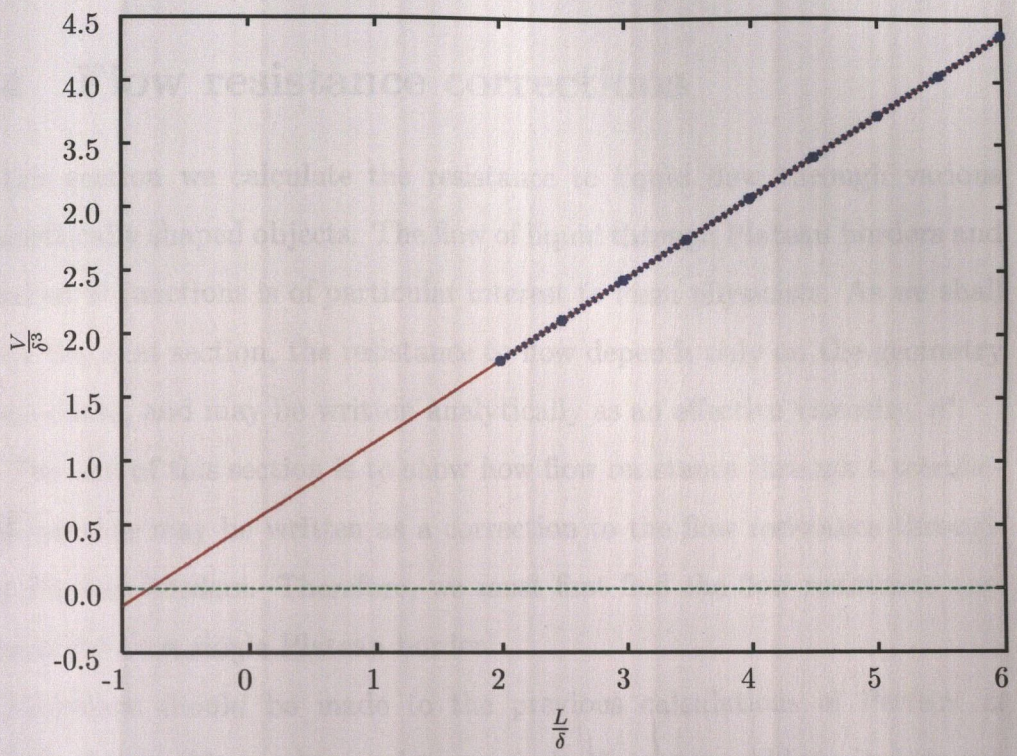

Figure 4.4: Four Plateau borders of length L and cross sectional area A_{Pb} meet to form a tetrahedral vertex. The volume of the tetrahedral vertex may be consider as part of the liquid within the Plateau borders provided their lengths are adjust to an effective length, L_{eff}. The blue line indicates results from the *Surface Evolver*, the red line is a straight line fit.

From Figure 4.4 we calculate the length correction per Plateau border as $A_{Pb}(0.78\delta)$. The total volume per Plateau border, including volume correction, is $A_{Pb}L_{eff}$, where $L_{eff} = L + 0.78\delta$. However, a foam is a network of Plateau borders, and each Plateau border in that network is attached to two tetrahedral junctions. The length correction per Plateau border is therefore

$$L_{eff} = L + 1.56\delta \tag{4.8}$$

and the volume of a Plateau border with length correction is simply

$$V_{Pb} = A_{Pb}\,(L + 1.56\delta) \tag{4.9}$$

This result agrees with the value calculated by Phelan to within 5%.

4.4 Flow resistance corrections

In this section we calculate the resistance to liquid flow through various geometrically shaped objects. The flow of liquid through Plateau borders and tetrahedral junctions is of particular interest to foam physicists. As we shall see in the next section, the resistance to flow depends only on the geometry of the ducts, and may be written analytically as an effective viscosity, η^*.

The aim of this section is to show how flow resistance through a tetrahedral junction may be written as a correction to the flow resistance through four Plateau borders. Therefore, we must first find the flow resistance correction due to a single Plateau border.

Reference should be made to the previous calculations of Pertsov *et al.* [57]. While this is addressed to precisely the same problem, it does not provide a transparent representation or a simple phenomenology (length correction) of the type which we have used. It has proved difficult, therefore, to make any clear comparison with the previous results.

4.4.1 Theory and entrance corrections

We restrict ourselves to considering solutions for the case of an incompressible Newtonian fluid, with constant transport properties, flowing through various ducts. We summarise the theory of duct flow, as described by White [58] and Landau and Lifshitz [59], in the following sections.

The fluid mechanics equations which describe the flow of liquid through a duct are based on the more general continuity and momentum equations

describe by Tannehill *et al.* [60],

$$\frac{\partial \rho}{\partial t} + \nabla \cdot \left(\rho \tilde{\mathbf{V}}\right) = 0 \tag{4.10}$$

$$\frac{\partial (\rho \tilde{\mathbf{V}})}{\partial t} + \tilde{\mathbf{V}} \cdot \nabla (\rho \tilde{\mathbf{V}}) = B_F + S_F \tag{4.11}$$

where ρ is the local density of the fluid, $\mathbf{V}(u, v, w)$ is the local velocity, $\mathbf{p}(x, y, z)$ is the local pressure, B_F are the body forces per volume and S_F are the surface forces per volume.

These equations can be greatly simplified for duct flow. Applying the substantive derivative,

$$\frac{D(\cdots)}{Dt} \equiv \frac{\partial(\cdots)}{\partial t} + \nabla \cdot \tilde{\mathbf{V}}(\cdots), \tag{4.12}$$

to equation 4.10 and assuming the flow is incompressible,

$$\frac{D\rho}{Dt} = 0 \tag{4.13}$$

produces the simplified continuity equation,

$$\nabla \cdot \tilde{\mathbf{V}} = 0 \tag{4.14}$$

The body forces in equation 4.11 are taken as zero, and the viscosity of the liquid is constant giving surface forces of $S_F = -\nabla p + \eta \nabla^2 \tilde{\mathbf{V}}$ Applying equations 4.12 and 4.13 to equation 4.11 produces the simplified Navier-Stokes equation,

$$\rho \frac{D\tilde{\mathbf{V}}}{Dt} = -\nabla \tilde{\mathbf{p}} + \eta \nabla^2 \tilde{\mathbf{V}} \tag{4.15}$$

Furthermore, we assume that we are dealing with Poiseuille type, pressure driven, steady flows, so

$$\frac{D\tilde{\mathbf{V}}}{Dt} = 0 \tag{4.16}$$

There is a no-slip boundary condition at the duct walls, and velocities are low enough to produce Reynolds numbers well inside the non-turbulent flow regime, $Re < 1$.

When liquid enters a straight duct of arbitrary but constant shape, friction against the duct wall causes a viscous layer to form at the inlet and grow in thickness downstream from the entrance, White [58]. This causes an internal flow in the duct which is constrained by the solid duct walls. At some distance downstream these viscous layers must coalesce, at which point the flow will be completely filled with boundary layer, as described by Shah and London [61]. Some small distance further downstream the flow profile becomes fully developed - i.e. the velocity becomes purely axial and varies with lateral coordinates only ($v \equiv 0, w \equiv 0, u \equiv u(y,z)$, i.e. $u(x) = 0$). The continuity and momentum equations reduce to

$$\frac{\partial u}{\partial x} = 0 \tag{4.17}$$

$$0 = -\frac{\partial p}{\partial x} + \eta\left(\frac{\partial^2 u}{\partial y^2} + \frac{\partial^2 u}{\partial z^2}\right) \tag{4.18}$$

In the regime of fully developed flow, the total pressure p is only a function of x, and furthermore, since the velocity u is independent of x, it follows that the gradient $\frac{\partial p}{\partial x}$ must be constant.

Equation 4.18 reduces to the classic Poisson equation, [62], and describes fully developed flow in a duct, with axis oriented in the x direction, with zero flow its surface

$$\frac{\partial^2 u}{\partial y^2} + \frac{\partial^2 u}{\partial z^2} = \frac{1}{\eta}\frac{dp}{dx} = \text{Constant} \tag{4.19}$$

Equation 4.19 may be cast in a dimensionless form for some general duct of width, b, by introducing the substitutions $y^* = \frac{y}{b}$, $z^* = \frac{z}{b}$, $u^* = \frac{\eta u}{b^2(-\frac{dp}{dx})}$, $u^* = 0$ on the duct surface, giving Laplace's equation

$$\nabla^{*2}(u^*) = -1 \tag{4.20}$$

Our ultimate goal is to use numerical techniques to calculate the flow resistance of a tetrahedral junction using a computational fluid mechanics package - *Fluent* [24]. However, it is first necessary to check the validity of results produced by *Fluent*. This is done by calculating the flow resistance in a number of test cases and comparing them with known analytical results.

4.4.2 A circular duct

The velocity profile of liquid flowing through a duct with circular cross sectional area is well known, [58, 59]. The velocity $\tilde{\mathbf{u}}(x, y, z)$ is obtained by solving Laplace's equation, equation 4.20, for a pipe of radius r_0 and cross sectional area A. The problem is best addressed by transforming to polar coordinates (x, r, θ) and choosing the origin at $(0, 0, 0)$. For fully developed flow the velocity $\tilde{\mathbf{u}} = \tilde{\mathbf{u}}(x, r, \theta)$ is purely axial, i.e. $\tilde{\mathbf{u}} = \tilde{\mathbf{u}}(r)$. Writing equation 4.20 in dimensionless form gives $r^* = \frac{r}{r_0}$. The Laplacian operator reduces to

$$\nabla^2 = \frac{1}{r}\frac{d}{\partial r}\left(r\frac{d}{\partial r}\right) \tag{4.21}$$

Solving equation 4.21 gives the dimensionless radial velocity

$$u = \frac{1}{4\eta}\frac{dp}{dx}(r_0^2 - r^2) \tag{4.22}$$

The velocity distribution across the pipe is parabolic in shape with a maximum value u_{max} when $r = 0$

$$u_{max} = \frac{1}{4\eta}\frac{dp}{dx}(r_0^2).$$

The volume flow rate, Q, is defined as the total volume of fluid flowing through a cross-section of the pipe in unit time. A volume $2\pi r dr u$ passes through an annular element $dA = 2\pi r dr$ of the cross sectional area, giving

$$Q = \int u dA. \tag{4.23}$$

Integration gives

$$Q = \frac{(\pi r_0^2)^2}{8\pi\eta}\frac{dp}{dx}. \quad (4.24)$$

$$= \frac{1}{8\pi\eta}\frac{dp}{dx}A^2. \quad (4.25)$$

where the effective viscosity of a circular tube is written as $\eta^* = \chi\eta$ and $\chi = 8\pi$. Note η^* is independent of the tube radius.

The mass flow rate M is defined as the total mass flowing through a cross-section of the pipe in unit time,

$$M = \rho Q$$

The radial velocity, u, the maximum velocity, u_{max}, and the mass flow rate, M, for liquid flowing in a circular pipe are calculable using *Fluent* [24]. A tessellated circular duct of length L and radius r is produced using a precursor meshing package called Gambit [63]. The hollow circular duct is then internally meshed with small tetrahedral cells. Fluent solves the simplified continuity and momentum equations 4.14 and 4.15, for incompressible fluid flow within the circular duct.

The pressure difference between the flow inlet and flow outlet is set and the pressure gradient is written as

$$\frac{dp}{dx} = \frac{\Delta p}{L}$$

The velocity profile at a circular cross sectional plane, $x = L/2$, is parabolic and shows that there is Poiseuille flow as expected, Figure 4.5. The maximum velocity, u_{max}, may be read directly from the Figure. Furthermore, a cross sectional slice along the length of the duct shows the velocity profile down the tube, Figure 4.6.

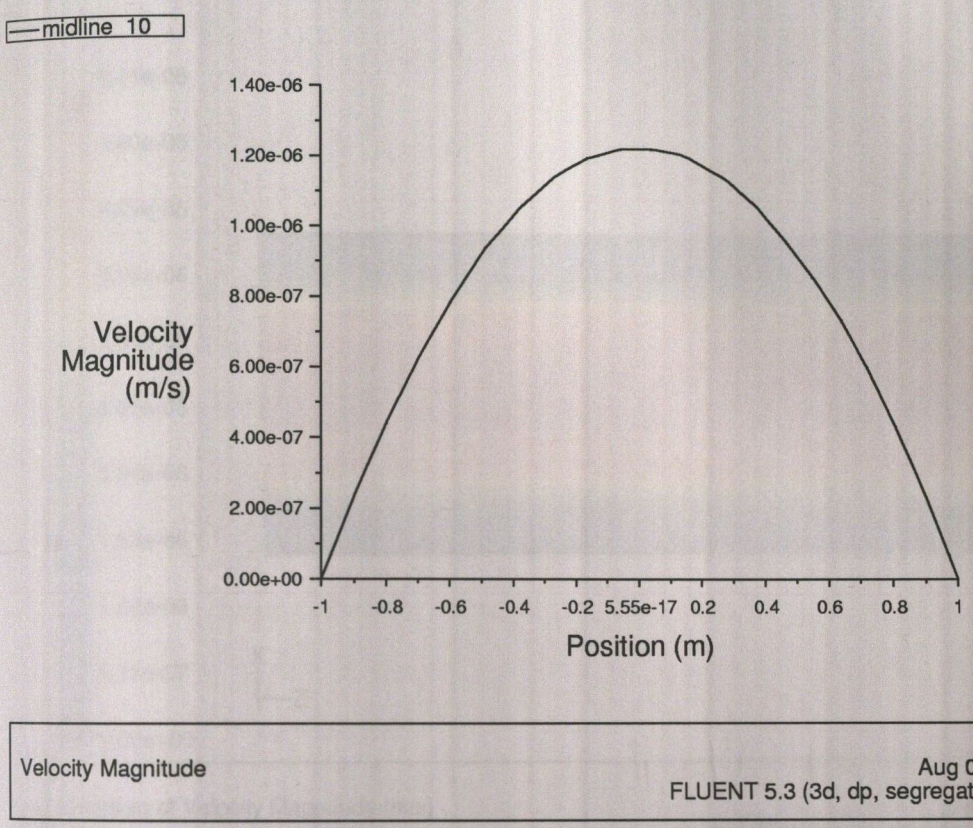

Figure 4.5: A velocity profile of Poiseuille flow in a circular duct is parabolic. The profile is taken at a cross section at $x = \frac{L}{2}$, this ensures the flow is fully developed. The maximum velocity 4.4.2 may be read directly from the graph. The profile is produced using *Fluent*.

Choosing $L = 10m$, $r_\circ = 2m$, $\Delta p = 1.2 \times 10^{-8} Pa$ and using the physical properties of water ($\eta_{Water} = 1.002 \times 10^{-3}$), we may calculate u_{max}^{Fluent} and $u_{max}^{analytical}$ for comparison.

If no analytical solutions to equation 4.20 exist, then it is not be possible to calculate the effective viscosity of the duct without using numerical methods. However, the average velocity of the duct can also be written in terms

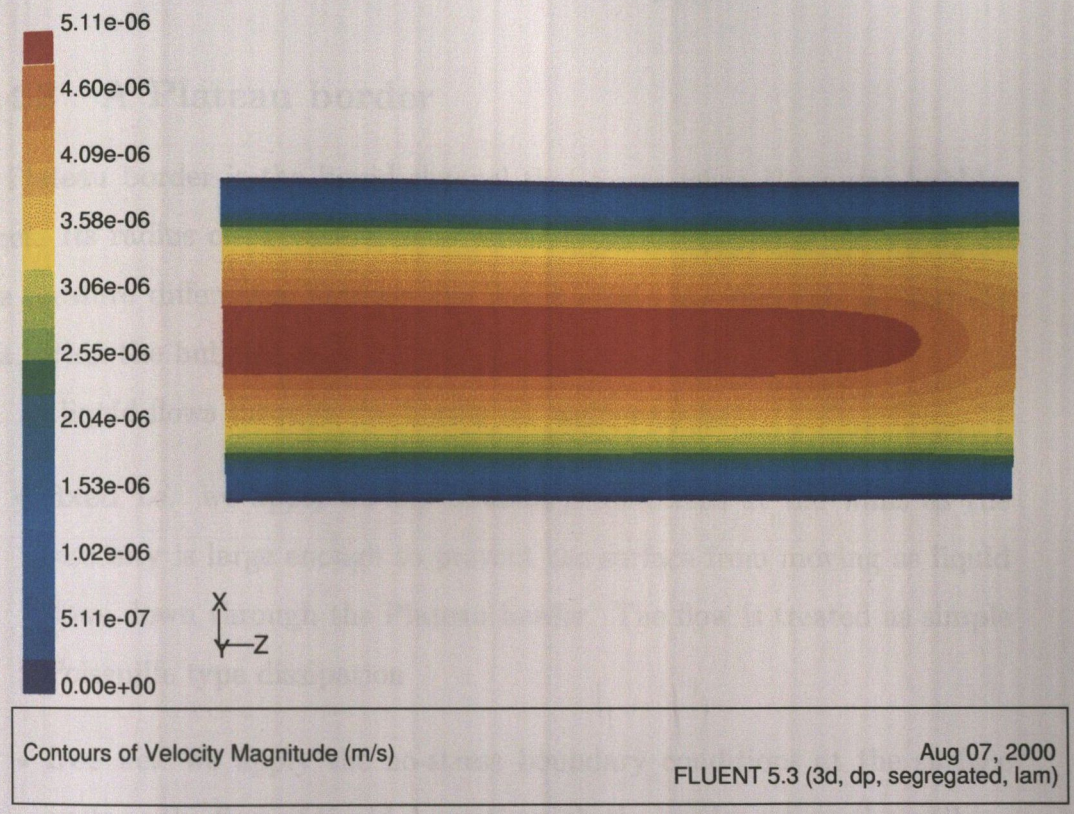

Figure 4.6: Fluid entering a circular duct from the right initially causes a viscous layer to form at the inlet. The flow is still accelerating down the tube near the entrance, as the different colours in the figure suggest. Some short distance downstream, $\approx r_0$, predicted by Shah and London [61], the flow becomes fully developed and the velocity, u, becomes purely axial. This is evident from the parallel strips of constant velocity down the length of the sample.

of the effective viscosity,

$$u = \frac{1}{\chi\eta}\frac{dp}{dx}A. \tag{4.26}$$

and the liquid flow rate may simply be written as

$$Q = Au = \frac{1}{\chi\eta}\frac{dp}{dx}A^2. \tag{4.27}$$

By calculating Q numerically, it is still possible to calculate the effective

viscosity. It is not possible to find an analytical solution to equation 4.20 for more complicated geometries, such as tetrahedral junctions.

4.4.3 A Plateau border

A Plateau border is the liquid channel that forms when three gas bubbles meet. Its radius of curvature, $R = R1 = \delta, (R2 = \infty)$, depends simply on the pressure differences between the liquid within the channel, p_l, and the gas within the bubbles, p_g.

As liquid flows through the border its' walls may be

- **fixed** i.e. we apply no-slip boundary conditions at the walls as the viscosity is large enough to prevent the surface from moving as liquid flows down through the Plateau border. The flow is treated as simple Poiseuille type dissipation

- **free** i.e. we apply the no-stress boundary conditions at the surface walls as the flow of liquid down through the border causes the walls to move and accommodate the flow

We only consider the case of fixed walls. As a consequence we write the average velocity of fluid flowing through a single Plateau border oriented in the x direction as

$$u = \frac{1}{\chi \eta_m} \frac{dp}{dx} A_{Pb} \tag{4.28}$$

η_m is the viscosity of the material flowing through the Plateau border, A_{Pb} is the cross-sectional area of the Plateau border and χ is a constant due to the geometry of the system. Once we know the value of χ we can fully describe the flow of liquid through a single Plateau border - and hence a network of Plateau borders. This will allow us to model liquid drainage in foams.

Peters, [64], used a boundary integral method to solve Laplace's equation for a Plateau border. This allowed him to calculate the effective viscosity of liquid flowing through that geometry. We describe how to solve the equations for fluid flow in a Plateau border using *Fluent*.

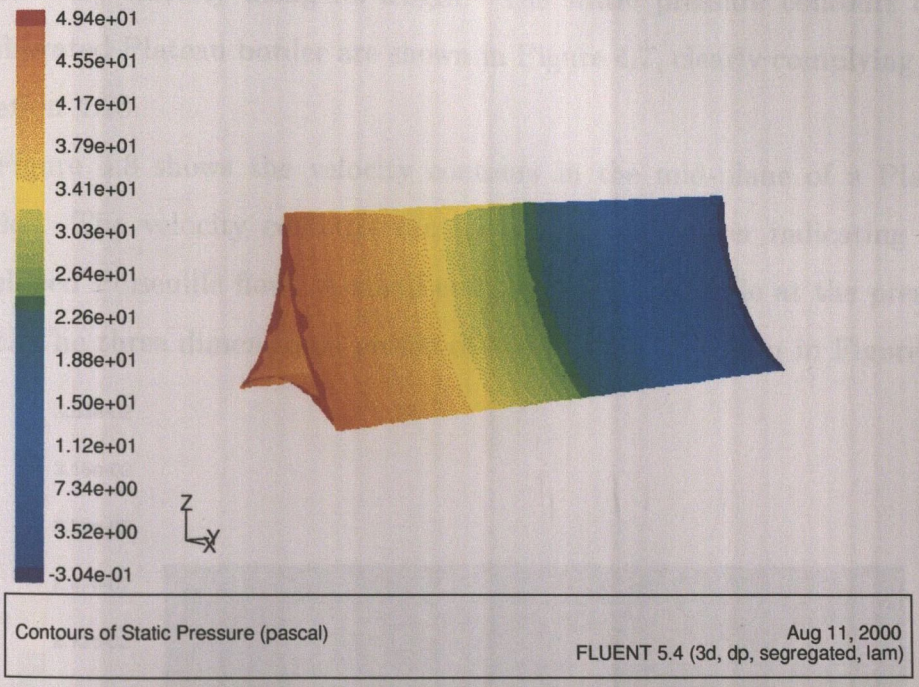

Figure 4.7: The pressure on the walls of a Plateau border should vary linearly with its length according to equation 4.28. The image shows a three dimensional image of the surface pressure. The pressure inlet is the red area on the left of the picture and the pressure outlet is the blue area to the right of the picture. The image was produced by solving the Navier-Stokes equations for incompressible Poiseuille type flow using the numerical fluid mechanics package *Fluent*.

The exact geometry of a Plateau border is produced using the *Surface Evolver* and the geometrical parameters A_{Pb}, δ and V_{Pb} are set at this stage. A special script was written to convert from an *Evolver* surface mesh to a mesh compatible with *Fluent*. This is fed into *Fluent's* precursor package, *Gambit*. The Plateau border interior is then meshed and finally loaded into

Fluent. The pressure difference at the ends of the Plateau border is set and the physical properties of water chosen. The system is iterated to an equilibrium flow profile.

Equation 4.28 suggests that the pressure on the Plateau border walls should vary linearly along its length. The static pressure contours of an equilibrated Plateau border are shown in Figure 4.7, clearly complying with equation 4.28.

Figure 4.8 shows the velocity contours in the mid-plane of a Plateau border. The velocity contours run parallel to each other indicating fully developed Poiseuille flow. A small entrance effect is visible at the pressure inlet. The three dimensional profile of flow in a PB is shown in Figure 4.9.

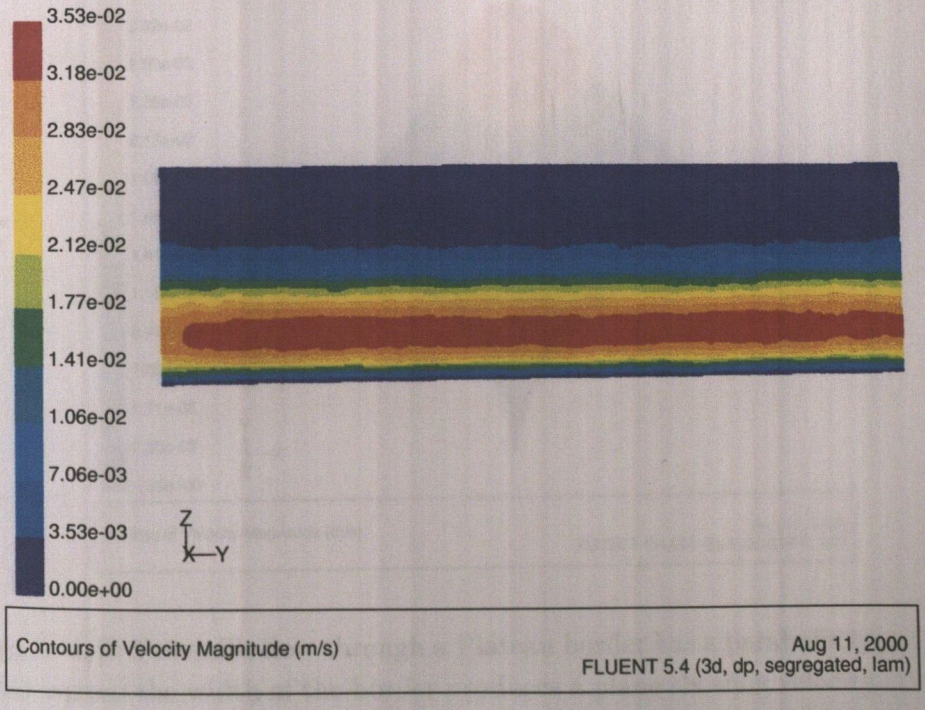

Figure 4.8: The majority of flow in a Plateau border occurs in the centre. A small entrance effect is observed at the pressure inlet (velocity inlet) at the left of the picture. Flow is then fully developed and Poiseuille type as depicted by the distinctly different and parallel colored velocity regions.

This is clearly parabolic in shape, as expected.

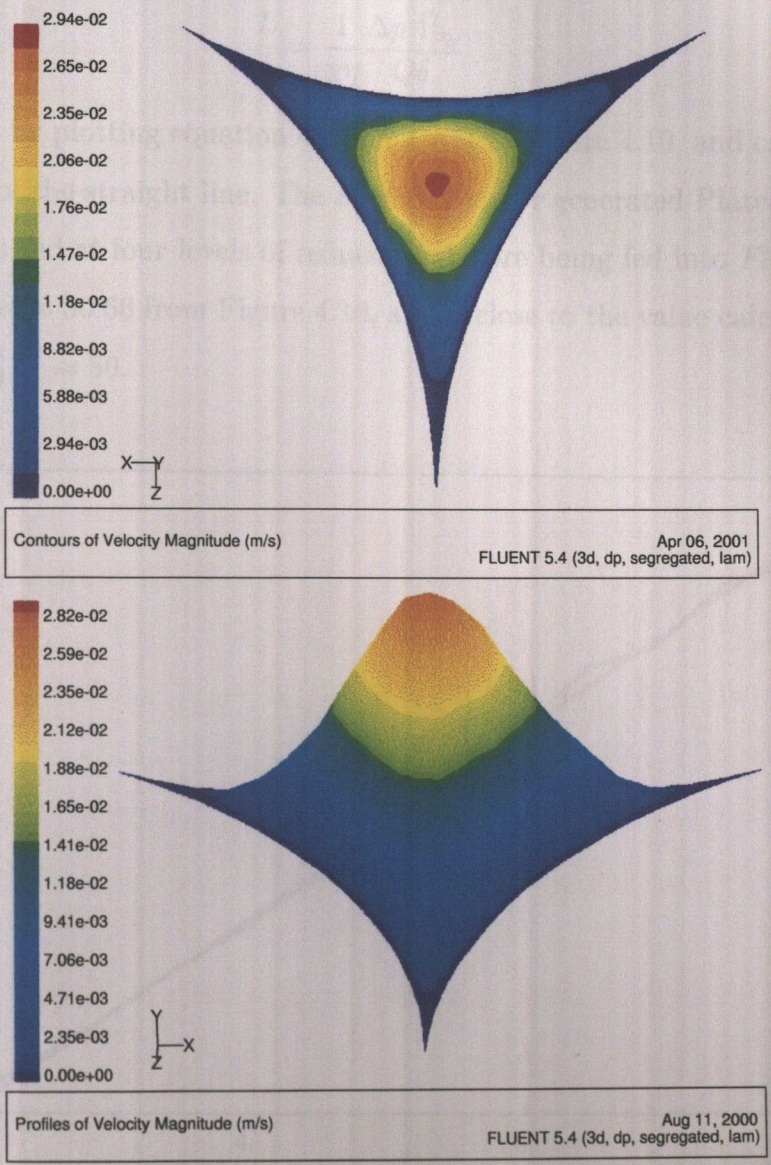

Figure 4.9: Poiseuille flow through a Plateau border has a parabolic type profile. A slice across the width of the border produces a plane showing velocity contours, (top). A plot of contours against position confirms the existance of the parabolic type profile, (bottom).

The *Surface Evolver* and *Fluent* may be used to calculate the liquid flow

rate, Q for different values of L and δ.

$$\frac{L}{\delta} = \frac{1}{\chi\eta}\frac{\Delta p A_{Pb}^2}{Q\delta} \tag{4.29}$$

χ is found by plotting equation 4.29 on a graph, Figure 4.10, and calculating the slope of the straight line. The *Surface Evolver* generated Plateau border was minimised at four levels of refinement before being fed into *Fluent*. χ is found to be ≈ 50.66 from Figure 4.10, and is close to the value calculated by Peters [64], $\chi \approx 50$.

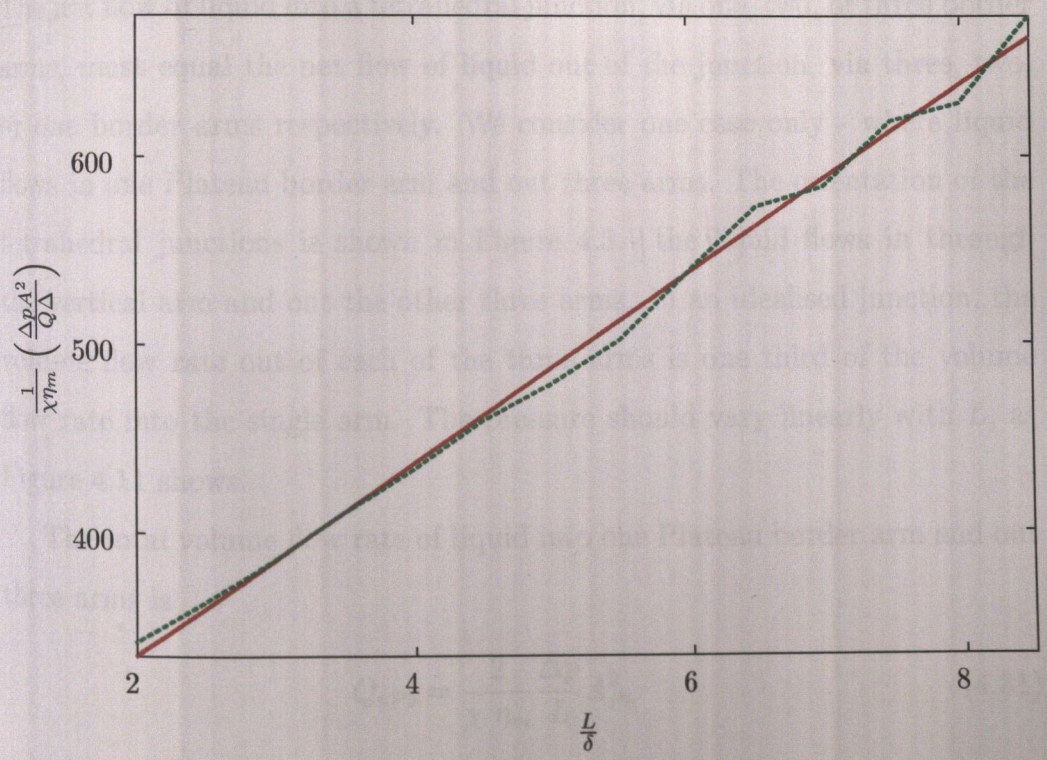

Figure 4.10: Fluent may be used to calculate the flow resistance, χ, of liquid in a Plateau border with fixed walls. The flow is Poiseuille type. χ may be calculated from equation 4.29. The numerical points produced using Fluent are plotted on the green line. A linear fit, $f(x) = ax + ba$, calculates the slope of the graph, and hence the flow resistance as $\chi \approx 50.66$

4.4.4 A tetrahedral junction

A tetrahedral vertex is comprised of four Plateau borders meeting at a single junction. We wish to calculate the flow resistance of a single junction as a correction to the flow resistance of individual Plateau borders. Implementation details are provide in section 7.5.1.

The volume flow rate of liquid in a single tetrahedral junction was defined, by equation 4.30, as

$$Q = \frac{1}{\chi \, \eta_m} \frac{\Delta p}{L} A_{Pb}^2 \tag{4.30}$$

The net flow of liquid into a tetrahedral junction, via one, two, or three border arms, must equal the net flow of liquid out of the junction, via three, two, or one border arms respectively. We consider one case only - where liquid flows in one Plateau border arm and out three arms. The orientation of the tetrahedral junctions is shown in Figure 4.3 - the liquid flows in through the vertical arm and out the other three arms. In an idealised junction, the volume flow rate out of each of the three arms is one third of the volume flow rate into the single arm. The pressure should vary linearly with L, as Figure 4.11 shows.

The total volume flow rate of liquid into one Plateau border arm and out three arms is

$$Q_{4Pb} = \frac{2}{\chi \, \eta_m} \frac{\Delta p}{L} A_{Pb}^2 \tag{4.31}$$

However, the Plateau border arms are swollen in the vicinity of the junction and a length correction of order $\pm C\delta^3$ is applied to each arm to account for this

$$Q_V = \frac{2}{\chi \, \eta_m} \left(\frac{\Delta p}{L \pm C\delta} \right) A_{Pb}^2 \tag{4.32}$$

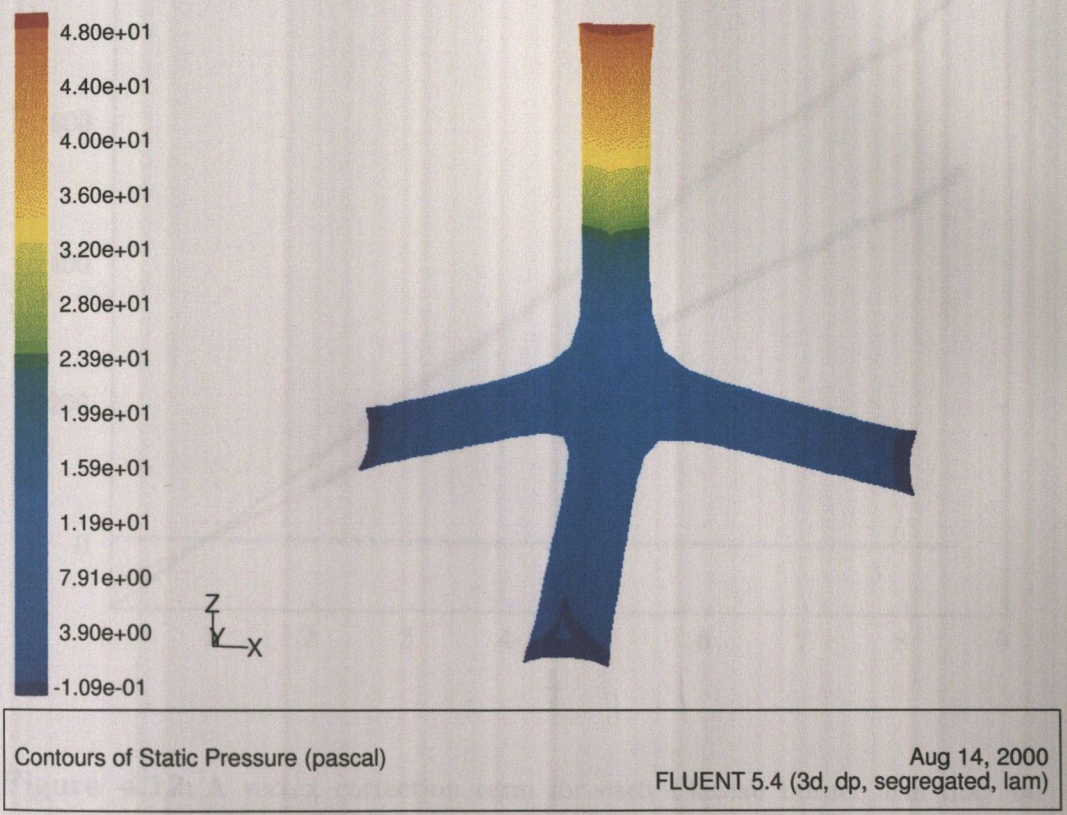

Figure 4.11: A tetrahedral vertex showing the variation of static pressure on its surface. Produced using Fluent via Gambit and the Surface Evolver.

We rewrite this in a dimensionless form

$$\frac{L}{\delta} + \mathcal{C} = \frac{2}{\chi_{Pb}\,\eta_m} \frac{\Delta p}{Q_V} \frac{A_{Pb}^2}{\delta} \tag{4.33}$$

where $\mathcal{C}$ is the intercept with the $X-$axis and $\chi\eta$ is the effective viscosity.

A plot of equation 4.33, fitted against a straight line, is shown in Figured 4.12. From the graph we find $\mathcal{C} \simeq -0.995$. Hence,

$$\frac{L_{eff}}{\delta} = \frac{2}{\chi_{Pb}\,\eta_m} \frac{\Delta p}{Q_V} \frac{A_{Pb}^2}{\delta} \tag{4.34}$$

where $L_{eff} = L - 0.955\delta$. The flow in the borders clearly Poiseuille type, Figure 4.13.

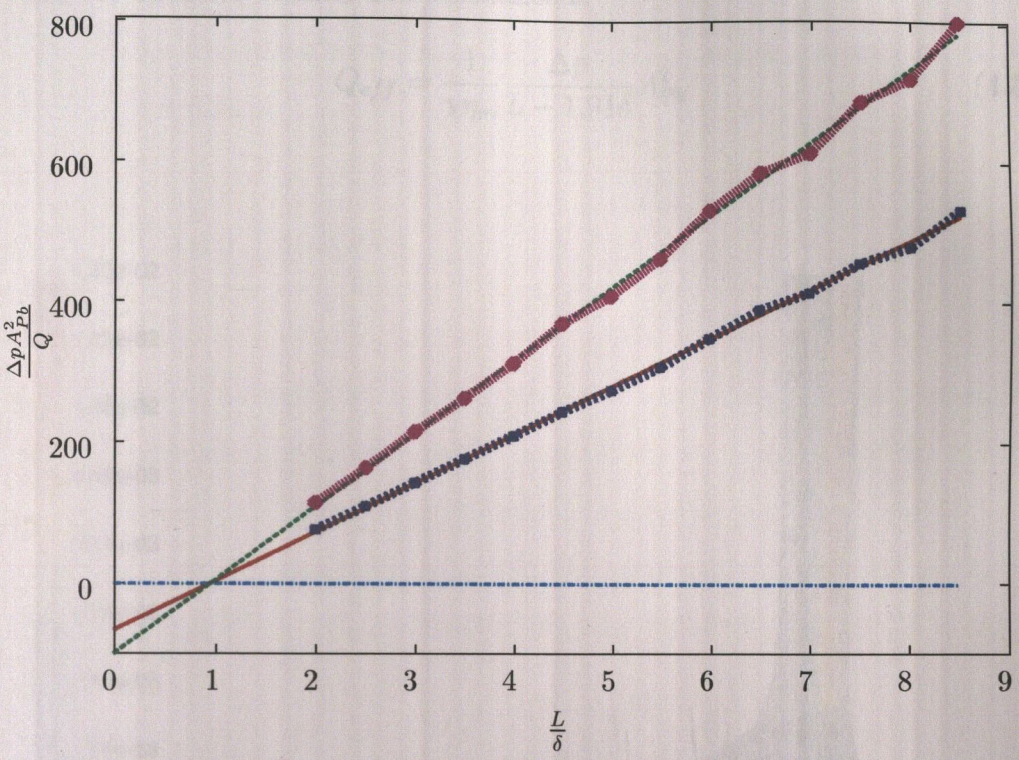

Figure 4.12: A vertex correction term for each Plateau border arm may be written as a length correction of 0.955 δ. The data points are calculated using the *Surface Evolver* and *Fluent*. The dark blue line is calculated for flow in through one Plateau border and out through three borders. The purple line is calculated for flow in through into one Plateau border and out one of the three symmetric borders. The red and green lines are fits of $f(x) = ax + ab$, and $g(x) = cx + cd$. The slope of the red line is $\frac{4}{3}(\chi)$, and the slope of the green line is $2(\chi)$. The flow resistance term for a single Plateau border is calculated as $\chi = 52$, and the intersection with the x axis is calculated as 0.955 δ.

A real foam forms around a network of Plateau borders, with each border connected to two tetrahedral junctions. Therefore, the effective length per Plateau border is

$$L_{eff} = L - 1.91\delta \tag{4.35}$$

and the effective volume flow resistance is

$$Q_{eff} = \frac{1}{\chi \eta_m} \frac{\Delta p}{L - 1.91\delta} A_{Pb}^2 \tag{4.36}$$

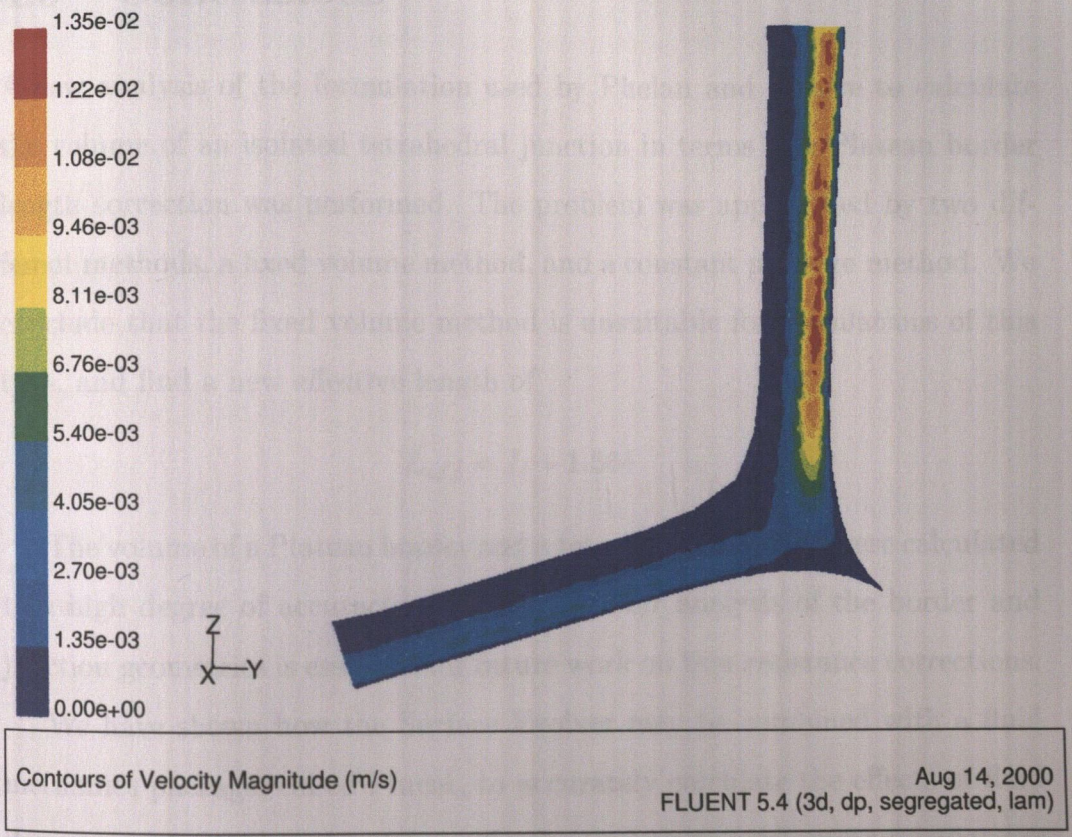

Figure 4.13: A mid-plane cutting two of the arms of a tetrahedral vertex shows contours of the velocity magnitude. The contours should be straight and parallel for fully developed Poiseuille-type flow. Produced using Fluent via Gambit and the Surface Evolver.

This appears to be a truly surprising result. A tetrakaidecahedra with a Plateau border arm length $L = 1$ and radius $\delta = 0.2$ has a liquid fraction of $\Phi_l \approx 0.006$, but its effective Plateau border length for resistance measurements is $L_{eff} \approx 0.62$, which is a very large effect. However, caution is

advised, as rather complicated scaling is required to judge the true magnitude of this resistance correction. This remains as active research within the TCD foams group.

4.5 Conclusions

A new analysis of the formulation used by Phelan and Weaire to calculate the volume of an isolated tetrahedral junction in terms of a Plateau border length correction was performed. The problem was approached by two different methods, a fixed volume method, and a constant pressure method. We conclude that the fixed volume method is unsuitable for calculations of this type, and find a new effective length of

$$L_{eff} = L + 1.56\delta$$

The volume of a Plateau border and a tetrahedral junction were calculated to a high degree of accuracy. Accurate Evolver analysis of the border and junction geometries is essential for future work on flow resistance corrections.

We have shown how the Surface Evolver may be combined with a fluid mechanics package, called Fluent, to accurately calculate the effects of fluid flow on an idealised foams. We confined ourselves to performing calculations on a single Plateau border and a single tetrahedral junction where the fluid flow was Poiseuille type. The results of this calculation raise some serious questions about the validity of the assumptions leading to the derivation of the foam drainage equation. It is clear from these calculations that even tetrahedral junctions with low liquid fractions $\Phi_l < 0.01$ have a meaningful effect on the velocity of liquid flowing through them. Yet, the foam drainage equation is undoubtedly accurate at predicting flow profiles in foams at low liquid fractions (providing we can assume the no slip boundary condition).

The possibilities for new analysis does not stop there. The transport properties of Plateau borders and tetrahedral junctions at higher liquid fractions and under the equally interesting conditions of plug flow (or no stress boundary conditions) may be calculated using Fluent.

The *Surface Evolver* calculates the geometry of a foam due to its surface tension and liquid fraction only. *Fluent*, calculates the equilibrium flow profile for the foam subject to the geometry provided by the Evolver. Our ultimate aim must be to interface the two programs in some way allowing for the equilibrium flow profile and the minimum surface energy of the foam to be calculated together.

4.6 Acknowledgements

Thanks are due to Simon Cox for useful discussion on fluid mechanics and to Robert Phelan and Ken Brakke for comments on aspects of the Evolver.

Part III

Continuous systems

Introduction

In this part of the thesis, we present our code and test simulations used to calculate the effects of liquid drainage on bulk foam systems. We may no longer rely on numerical packages to describe the energy and volume of individual cells as liquid drains through them. In particular, we present and develop a numerical model of a metal foam formation process, and we describe the various profiles that may form in the competition between liquid drainage and solidification.

Chapter 5

Foam Drainage

5.1 Introduction

In Chapter 4, we developed the model of an idealised wet foam. We calculated the shape, volume and transport properties of the Plateau borders and tetrahedral junctions that form the liquid transport network within the foam. The calculations were performed on a localised basis - i.e. we considered a single Plateau border and a single tetrahedral junction. Localised calculations provide us with a better understanding of the properties of localised foam - but we must also be able to understand the properties of bulk foams. In this Chapter we address the fundamental question of how bulk foams drain. It is not possible to use the *Surface Evolver* or *Fluent* to carry out an accurate analysis of a large draining foam sample, we must move away from discrete localised calculations and consider modelling a draining foam as a continuous system.

Wet foams are typically made by blowing gas through a thin nozzle into a liquid, or by shaking or beating a liquid and trapping gas in the process, [3]. The former is atypical but useful for experimental purposes the latter is

the method for production of every day foams. Either way, the excess liquid drains out of the foam. We assume that drainage occurs over short time scales in comparison to the diffusion of gas between cells - so we may neglect coarsening effects.

The groundwork for the essentials of drainage theory was developed by Leonard and Lemlich [65]. Ultimately the theory leads to the formation of a partial differential equation, section A.4, which describes the flow of liquid through a network of Plateau borders. This theory is now well established[1].

Drainage theory plays a key role in the development of:

- Metal foam formation models - metal foams formed via the Fraunhofer process [67, 68, 69] drain predominantly due to gravity, Chapter 6, [70]
- Flowing foams - a model of flowing coalescing foams has been developed by Neethling et al. [71, 72]
- Stokes experiments on foams [73] - the drainage equation must be incorporated into *Fluent* to model the path of a ball falling through a foam
- Bubble sorting - at high liquid fractions, $\Phi_l > 0.2$, bubble motion and bubble sorting effects [74] are observed in a draining foam

Each of these models must be solved using numerical methods, so we must be confident we can accurately solve the drainage equation and yet be free to adapt it to suit the problem at hand. Therefore, we developed fast, efficient, and adaptable numerical solutions, with a view to easy extension to higher dimensions and accessibility to parallelism for fully three dimensional problems. This Chapter is dedicated to these solutions, which where created initially to model the metal foam formation process, Chapter 6.

[1] It has recently been called into question by Koehler et al. [11, 12, 66].

5.2 The foam drainage equation (f.d.e.)

The average velocity, u, of a fluid flowing down a straight Plateau border of cross sectional area A_{Pb} is given by equation 4.28, Chapter 4, where $\chi \sim 50$. This equation describes drainage due to gravity alone, it does not allow for a variation in the size of the Plateau border cross section - as its surface is fixed. This variation leads to a pressure gradient aiding the drainage processes and results in non uniform flow rates.

It is assumed that foams with low liquid fractions, $\Phi_l < 0.1$, are made up of a network of thin Plateau borders, which meet at symmetric tetrahedral junctions. The volume contribution of the junctions is ignored. The velocity is averaged over borders oriented in all spatial directions and the continuity equation is used to describe the rate of flow, the details of which are in Appendix A.4. The flow is Poiseuille-type as described in Chapter 4. The effects of fluid flow on tetrahedral junctions, as described in the previous Chapter, have been ignored by this model - thought it is clear from the previous Chapter that these effects may be significant even at small liquid fractions. Nevertheless, the equation has proved remarkably accurate in predicting experimental results [75, 76, 77].

The drainage equation is accredited to Goldfarb, Kahn and Schreiber [78], but was independently derived by Verbist et al. [9] who formally named it the *foam drainage equation*. The one dimensional form of the equation may be written as

$$\begin{aligned} \frac{\partial A_{Pb}}{\partial t} &= \frac{\partial Q_l}{\partial z} \\ Q_l &= A_{Pb}^2 - \frac{\sqrt{A_{Pb}}}{2}\left(\frac{\partial A_{Pb}}{\partial z}\right) \end{aligned} \tag{5.1}$$

where Q_l is defined as the liquid flow rate.

The *dimensionless* form of this equation, as outlined in Appendix A.5, is

$$\frac{\partial \alpha}{\partial \zeta} = -\frac{\partial \widehat{Q}_l}{\partial \zeta} \tag{5.2}$$

$$\widehat{Q}_l = \left(\alpha^2 - \frac{\sqrt{\alpha}}{2}\frac{\partial \alpha}{\partial \zeta}\right) \tag{5.3}$$

5.2.1 Analytical solutions of the f.d.e.

Three analytical solutions of the dimensionless f.d.e., derived by Verbist *et al.* [9], are described.

(i) **Equilibrium solution:** This is a trivial solution of the f.d.e. and is defined as the absence of flow within the foam.

$$\alpha(\zeta) = \left(\alpha_L^{-\frac{1}{2}} + \zeta_L - \zeta\right)^{-2} \tag{5.4}$$

A foam sample of length L with initial dimensionless liquid fraction α_L will drain to a constant equilibrium profile, described by equation 5.4, and shown in Figure 5.1.

(ii) **Steady drainage:** This is a solution of the equation when the average flow velocity α is constant throughout, i.e.

$$\widehat{Q}_l = \alpha^2 + \frac{\sqrt{\alpha}}{2}\frac{\partial \alpha}{\partial \zeta} \tag{5.5}$$

$$\frac{\partial \alpha}{\partial \zeta} = 0 \tag{5.6}$$

$$\therefore \widehat{Q}_l = \alpha^2 \tag{5.7}$$

This relationship is important as it may be applied to constant regions of the advective front.

(iii) **Solitary-wave solution:** This is known as forced drainage. Initially the foam sample starts with a uniform liquid density. Liquid is then

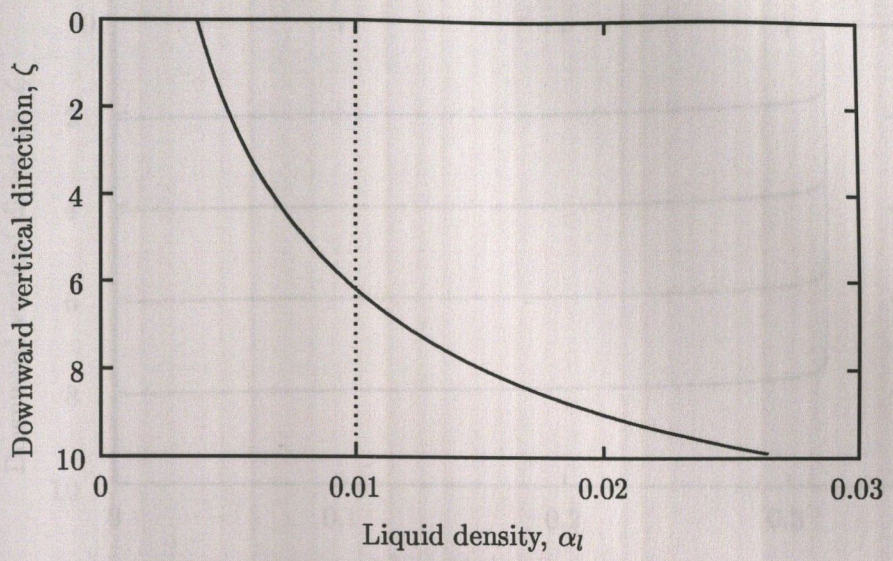

Figure 5.1: A foam with a constant initial liquid fraction, $\alpha_l = 0.01$, dashed line, is not in an equilibrium state. Liquid will drain out of the sample over time and an equilibrium profile is reached when gravitational and capillary forces balance, solid line.

continuously added from the top of the sample with a constant flow rate

$$\widehat{Q}_l = \alpha^2 + \frac{\sqrt{\alpha}}{2}\left(\frac{\partial \alpha}{\partial \zeta}\right) \tag{5.8}$$

This produces the profile shown in Figure 5.2 with analytical solution

$$\alpha(\zeta, \tau) = \begin{cases} v \tanh^2\left(\sqrt{v}\,(\zeta - v\tau)\right) & \zeta \leq v\tau \\ 0 & \zeta < v\tau \end{cases} \tag{5.9}$$

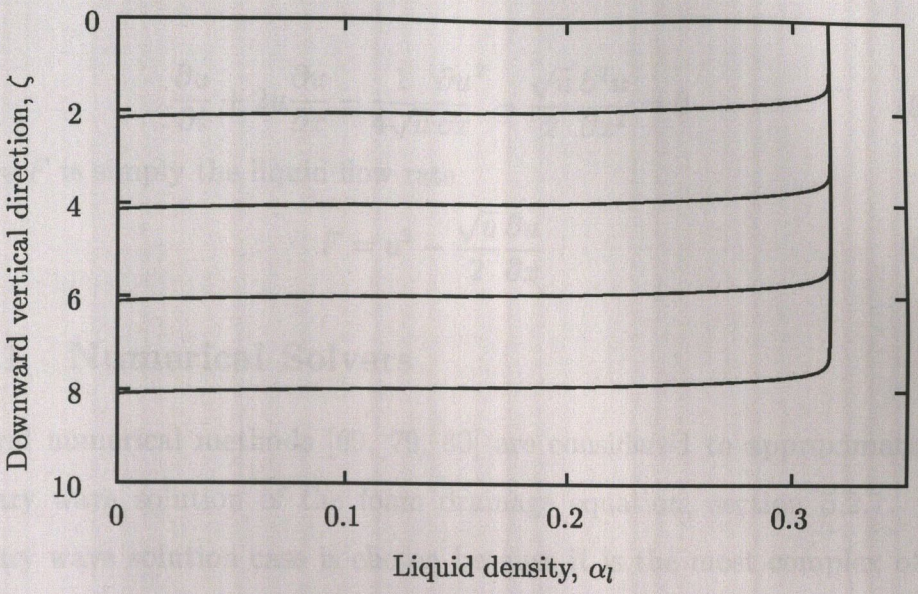

Figure 5.2: Adding liquid at a constant rate, Q_l, to the top of initially dry foam causes a solitary wave to form at the top of the sample and move downwards with an average velocity $u \propto Q_l^{\frac{1}{2}}$. The solid lines show the position of the solitary wave at dimensionless time, $\tau = 60, 120, 180, 240$.

5.3 Numerical analysis of the f. d. e.

Consider the partial differential equation

$$\frac{\partial u}{\partial t} + \frac{\partial F}{\partial x} = 0 \tag{5.10}$$

where $F \equiv F(u)$,$u \equiv u(x,t)$. F may be a linear or non-linear function of u, describing a wide variety of scientific problems. Equation 5.10 is written in conservative form, indicating the conservation of some general physical quantity, u. A desirable property of partial differential equations is the ability to write them in conservative form, as this is exploitable when generating accurate finite difference schemes.

Equation 5.10 describes the conservative form of the foam drainage equa-

tion

$$\frac{\partial u}{\partial t} + 2u\frac{\partial u}{\partial x} - \frac{1}{4\sqrt{u}}\frac{\partial u^2}{\partial x} - \frac{\sqrt{u}}{2}\frac{\partial^2 u}{\partial x^2} = 0 \tag{5.11}$$

where F is simply the liquid flow rate

$$F = u^2 - \frac{\sqrt{u}}{2}\frac{\partial u}{\partial x} \tag{5.12}$$

5.3.1 Numerical Solvers

Several numerical methods [60, 79, 80] are considered to approximate the solitary wave solution of the foam drainage equation, section 5.2.1. The solitary wave solution case is chosen because it is the most complex of the three solutions considered. Furthermore its analytical solution is known and may be compared directly with numerical results to ascertain their accuracy. These numerical methods are all *explicit finite difference schemes*, easily allowing additional terms or pre-factors to be included in the equation. In each case, x and t were discretised spatially and temporally with J and N uniform values of Δx and Δt respectively. F and u may then be calculated at the discretised points $(j\Delta x, n\Delta t)$ where $j \in 0, 1, \cdots, J$, $n \in 0, 1, \cdots, N$. Following convention we write $u_j^n \equiv u(j\Delta x, t\Delta t)$ and consider the upwind differencing, Lax [81], Lax-Wendroff [82] and MacCormack [83] numerical solvers. The following analysis and discussion draws from calculations of the macroscopic traffic equation, which is somewhat similar to the 1d drainage equation, of Helbing and Treiber [79].

One step methods :

Upwind:

$$\begin{aligned} F_j^n &= (u_{j-1}^n)^2 - \frac{\sqrt{u_{j-1}^n}}{2\Delta x}\left(u_j^n - u_{j-1}^n\right) \\ u_j^{n+1} &= u_j^n - \frac{\Delta t}{\Delta x}\left(F_{j+1}^n - F_j^n\right) \end{aligned}$$

Lax:

$$
\begin{aligned}
F_j^n &= (u_{j-1}^n)^2 - \frac{\sqrt{u_{j-1}^n}}{2\Delta x}\left(u_j^n - u_{j-1}^n\right) \\
u_j^{n+1} &= \frac{1}{2}\left(u_{j+1}^n + u_{j-1}^n\right) - \frac{\Delta t}{\Delta x}\left(F_{j+1}^n - F_{j-1}^n\right)
\end{aligned}
$$

Two step methods :

Lax-Wendroff:

$$
\begin{aligned}
F_j^n &= (u_j^n)^2 - \frac{\sqrt{u_j^n}}{2\Delta x}\left(u_j^n - u_{j-1}^n\right) \\
u_{j+\frac{1}{2}}^{n+\frac{1}{2}} &= \frac{1}{2}\left(u_{j+1}^n + u_j^n\right) - \frac{\Delta t}{2\Delta x}\left(F_{j+1}^n - F_j^n\right) \qquad (predictor) \\
F_{j+\frac{1}{2}}^{n+\frac{1}{2}} &= \left(u_{j+\frac{1}{2}}^{n+\frac{1}{2}}\right)^2 - \frac{\sqrt{u_{j+\frac{1}{2}}^{n+\frac{1}{2}}}}{2\Delta x}\left(u_{j+\frac{1}{2}}^{n+\frac{1}{2}} - u_{j-\frac{1}{2}}^{n+\frac{1}{2}}\right) \\
u_j^{n+1} &= u_j^n - \frac{\Delta t}{\Delta x}\left(F_{j+\frac{1}{2}}^{n+\frac{1}{2}} - F_{j-\frac{1}{2}}^{n+\frac{1}{2}}\right) \qquad (corrector)
\end{aligned}
$$

MacCormack:

$$
\begin{aligned}
F_j^n &= (u_j^n)^2 - \frac{\sqrt{u_j^n}}{2\Delta x}\left(u_j^n - u_{j-1}^n\right) \\
\overline{u_j^{n+1}} &= u_j^n - \frac{\Delta t}{\Delta x}\left(F_{j+1}^n - F_j^n\right) \qquad (predictor) \\
\overline{F_j^{n+1}} &= \left(\overline{u_j^{n+1}}\right)^2 - \frac{\sqrt{\overline{u_j^{n+1}}}}{2\Delta x}\left(\overline{u_j^{n+1}} - \overline{u_{j-1}^{n+1}}\right) \\
u_j^{n+1} &= \frac{1}{2}\left(u_j^n + \overline{u_j^{n+1}} - \frac{\Delta t}{\Delta x}\left(\overline{F_j^{n+1}} - \overline{F_{j-1}^{n+1}}\right)\right) \qquad (corrector)
\end{aligned}
$$

Boundary conditions.

The boundary conditions for forced drainage are set as

$$F = 0.1, j = 0, \forall t$$

$$u = 0.0, \forall j \text{ at } t = 0.$$

This ensures that liquid is flowing into the top of the foam at a constant rate.

Consistency.

Consistency describes the extent to which a finite difference representation approximates the partial differential equation (p.d.e.). In particular the difference between the p.d.e. and the finite difference equation should vanish as the grid is refined [60],

$$\lim_{\Delta x \to 0} (\text{Truncation Error}) \to 0.$$

The Upwind, Law-Wendroff and MacCormack methods were all found to be consistent. The Lax method was not consistent and therefore unsuitable for solving the drainage equation - we include it for comparison purposes.

Stability.

Every integration method introduces an associated numerical stability criteria. A method is unstable if a perturbation of the input values at the n^{th} time step grows in size at the $n + 1^{th}$ time step. In an unstable system the perturbation, or error, will continue to grow without bounds. This leads to an incorrect oscillating density profile - where the oscillations grow as the system evolves. The numerical methods previously described are constrained by two types of stability criteria, and must satisfy these criteria to avoid numerical instabilities.

Advective instability: Advective instabilities are associated with the erroneous spreading of the solution throughout the system - Figure 5.5 shows the effects of an advective instability on the Lax method. A stability criteria for equation 5.10 may be obtained by rewriting the equation as

$$\frac{\partial u}{\partial t} = -\frac{\partial F}{\partial u}\frac{\partial u}{\partial x} = -A\frac{\partial \alpha}{\partial z} \tag{5.13}$$

where A is the Jacobian matrix $\frac{\partial F}{\partial u}$.

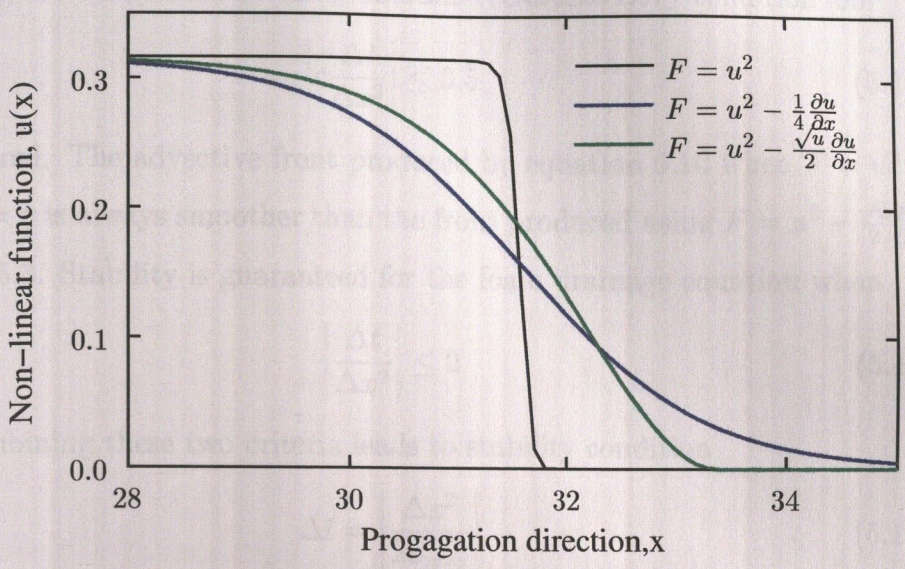

Figure 5.3: Shown is a comparison between advective fronts produced by three different fluxes, F. Black line - the foam drainage equation, Red line - a smoother front produced by linearising the gradient term, Blue line - a sharper front produced by removing the gradient term.

The Courant-Fredrichs-Levy (CFL) condition [60],

$$\left| A_{max} \frac{\Delta t}{\Delta x} \right| \leq 1 \tag{5.14}$$

is applicable for each of the numerical methods considered. For the foam drainage equation, F is the flow rate and u is the Plateau border cross-sectional area, so, $\frac{\partial F}{\partial u}$ is the rate of change of flow with Plateau border cross-sectional area. The advective front produced by equation 5.10 when $F = u^2$ is always a much sharper front than the case when $F = u^2 - \frac{\sqrt{u}}{2}\frac{\partial u}{\partial x}$, Figure 5.3. Hence using $F = u^2$ produces a stricter stability criteria than required for the foam drainage equation producing the CFL condition

$$\left| 2u_{max} \frac{\Delta t}{\Delta x} \right| \leq 1. \tag{5.15}$$

Diffusive stability. The existence of a gradient term in the flow rate indicates a diffusive property in the foam drainage equation. For numerical

stability, the additional diffusive Courant-Freidrichs-Levy condition [60]

$$\left| c\frac{\Delta t}{\Delta x^2} \right| \leq 0.5 \tag{5.16}$$

is required. The advective front produced by equation 5.10 when $F = u^2 - \frac{c}{2}\frac{\partial u}{\partial z}, c = \frac{1}{2}$ is always smoother than the front produced using $F = u^2 - \frac{\sqrt{u}}{2}\frac{\partial u}{\partial x}$, Figure 5.3. Stability is guaranteed for the foam drainage equation when

$$\left| \frac{\Delta t}{\Delta x^2} \right| \leq 2 \tag{5.17}$$

Combining these two criteria leads to stability condition

$$\Delta t = \left| \frac{\Delta x^2}{2u_{max}} \right| \tag{5.18}$$

for the Lax and Upwind methods and

$$\Delta t = \left| \frac{\Delta x^2}{\sqrt{2}u_{max}} \right| \tag{5.19}$$

for the two-step methods. The stability criteria for the two step methods are less strict as small erroneous fluctuations in the predictor step may be damped out by the corrector step.

Accuracy.

The discretisation errors associated with non-linear partial differential equations are generally difficult to estimate, most often due to the non-linearity of the problem. Local linearisation of the p.d.e. often allows for a rough estimate of the errors associated with smooth solutions to be calculated. Fortunately, the exact analytical solitary wave solution is known for the foam drainage equation, section 5.2.1. A direct calculation of the discretisation errors for each numerical method may be calculated and compared.

Analysis of the one step methods shows that the upwind discretisation, Figure 5.4, is more accurate than the Lax discretisation, Figure 5.5, whilst

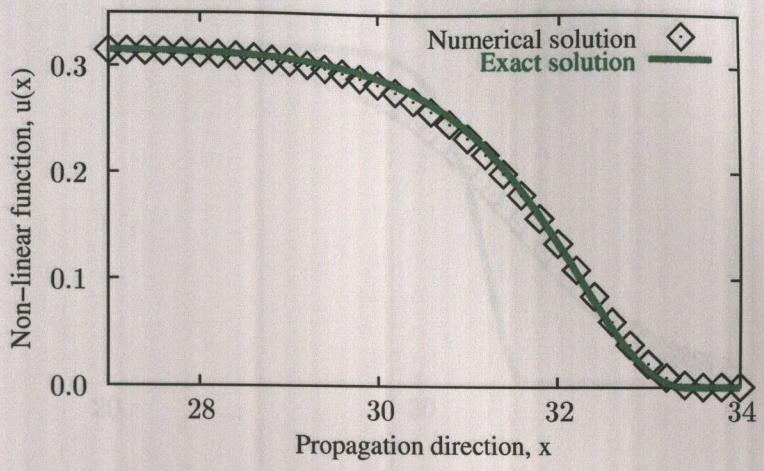

Figure 5.4: The exact and numerical solitary wave solution of the foam drainage equation is shown. The numerical solution is produced using upwind differencing. A small amount of numerical diffusion is visible in the comparison between the solutions. $\Delta x = 0.1$, $\Delta t = 0.01$, $J = 1000$.

analysis of the two step methods shows that Lax-Wendroff, Figure 5.6 and MacCormack, Figure 5.7, discretisation produce equally accurate results. The main discretisation errors in all the methods is numerical diffusion. Numerical diffusion is common in first order methods and results in a stretching, or smoothing, of the advective front. On the plus side, first order methods are monotonic and exhibit no oscillatory effects. The Lax method produces a highly diffusive front, and is completely unsatisfactory for modelling the foam drainage equation. The diffusive effects in the upwind method are minimal and the method produces sufficient accuracy with minimum computational effort.

Dispersive errors due to discretisation are associated with second order methods. The dispersive nature of these methods often causes waves with small amplitudes to propagate behind the advective front, leading to oscillations in the flux and density profiles. Normally, Lax-Wendroff and MacCormack are second order methods, but the existence of the gradient term in

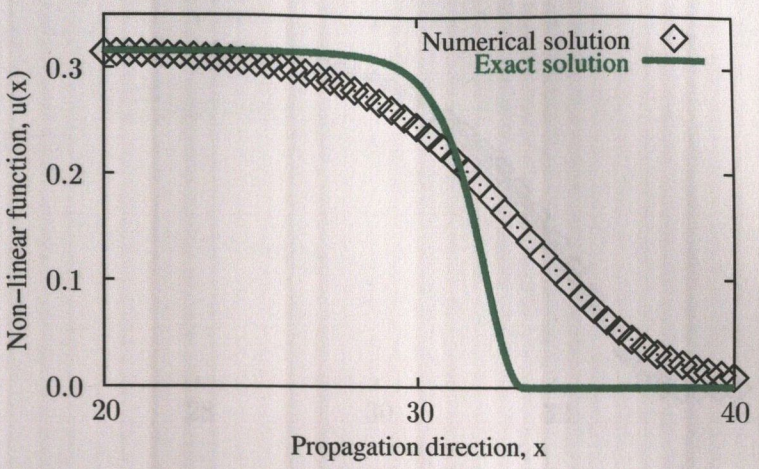

Figure 5.5: The exact and numerical solitary wave solution of the foam drainage equation is shown. The numerical solution is produced using the Lax method. A large amount of numerical diffusion is visible in the comparison between the solutions - indicating that the Lax methods is unsuitable for modelling the foam drainage equation. $\Delta x = 0.1$, $\Delta t = 0.01$, $J = 1000$.

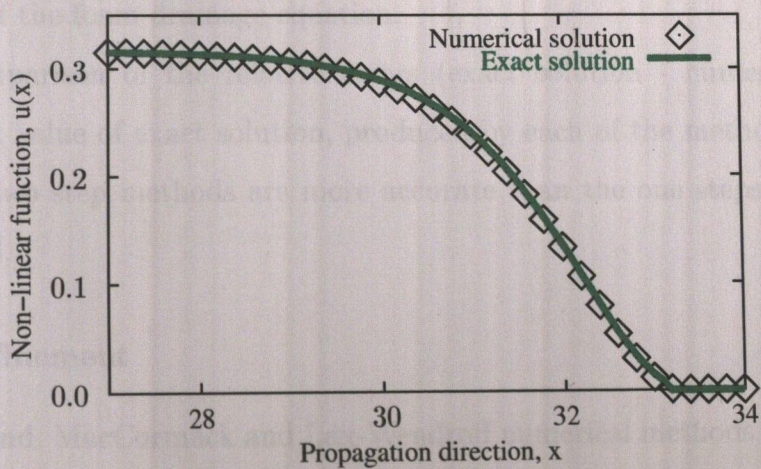

Figure 5.6: The exact and numerical solitary wave solution of the foam drainage equation is shown. The numerical solution is produced using the Lax-Wendroff method. No dispersive effects are visible in the numerical solution. $\Delta x = 0.1$, $\Delta t = 0.01$, $J = 1000$.

the flux equation, equation 5.12, makes them formally first order accurate. As a result no dispersive effects are observed using these methods when sim-

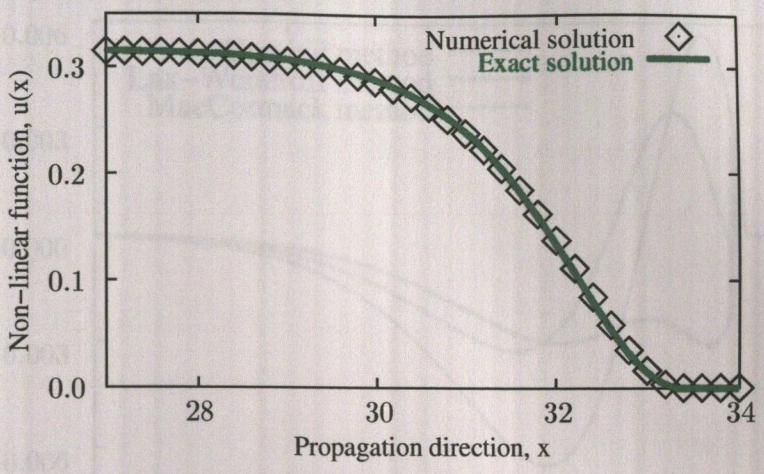

Figure 5.7: The exact and numerical solitary wave solution of the foam drainage equation is shown. The numerical solution is produced using the MacCormack method. No dispersive effects are visible in the numerical solution. $\Delta x = 0.1$, $\Delta t = 0.01$, $J = 1000$.

ulations of the foam drainage equation.

A comparison of the relative errors (exact solution - numerical solution)/max value of exact solution, produced by each of the methods, shows that the two step methods are more accurate than the one steps methods, Figure 5.8.

Mesh refinement

The Upwind, MacCormack and Lax-Wendroff numerical methods are consistent, therefore, refining the mesh decreases the size of the truncation error and provides a closer approximation to the exact solution, Figure 5.9. The mesh is refined by doubling the number of grid points, halving the grid step size Δx. Δt is altered accordingly to meet the CFL conditions.

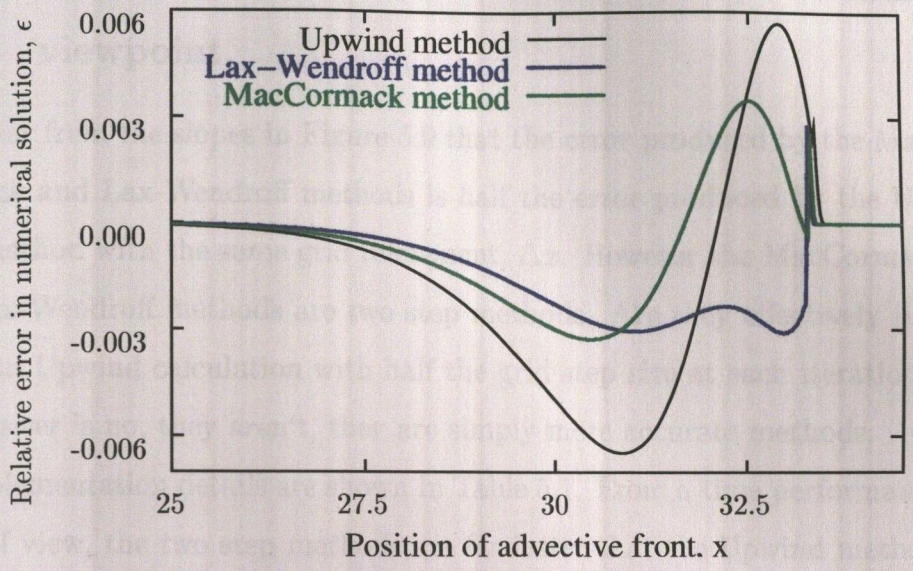

Figure 5.8: The relative difference between the analytical and numerical solitary wave solution of the foam drainage equation with $\Delta x = 0.1$ is shown. The numerical methods are indicated by colour: Upwind - red line, Lax-Wendroff - green line, MacCormack - blue line. Clearly the two step methods are more accurate than the single step method. The error due to Lax is so large it is not shown.

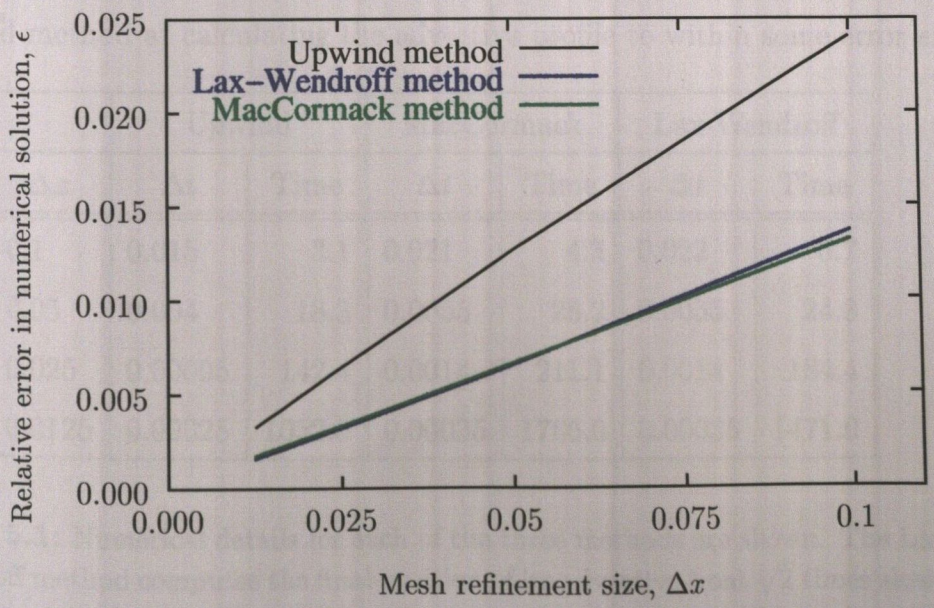

Figure 5.9: As the grid step size Δx decreases, the numerical error, ϵ, from the upwind, Lax-Wendroff and MacCormack methods decreases linearly. It is clear that the truncation errors vanish to zero as the grid step size approaches zero.

5.3.2 Comparison between methods from a performance viewpoint.

It is clear from the slopes in Figure 5.9 that the error produced by the MacCormack and Lax-Wendroff methods is half the error produced by the Upwind method with the same grid refinement, Δx. However the MacCormack and Lax-Wendroff methods are two step methods. Are they effectively just doing an Upwind calculation with half the grid step size at each iteration ? The answer is no, they aren't, they are simply more accurate methods.

Implementation details are shown in Table 5.1. From a time performance point of view, the two step methods are far faster that the Upwind method at calculating a solution to within some truncation error ϵ.

Now $\Delta t \propto 2\Delta x^2$, so each time the step size is halved the run time is increased by a factor of eight. The Upwind method finds the final profile of the advective front $\sqrt{2}$ times faster than the Lax-Wendroff method, but with half the accuracy. The Lax-Wendroff method is $4\sqrt{2}$ times faster than the Upwind method at calculating the advective profile to within some error ϵ.

	Upwind		MacCormack		Lax-Wendroff	
Δx	Δt	Time	Δt	Time	Δt	Time
0.1	0.015	3.1	0.021	4.3	0.022	3.7
0.05	0.004	18.3	0.0055	28.2	0.0055	24.8
0.025	0.00095	142.4	0.0014	211.1	0.0014	184.4
0.0125	0.00025	1052.0	0.00035	1786.0	0.00035	1471.0

Table 5.1: Numerical details for each of the three methods are shown. The Lax-Wendroff method computes the final position of its advective front $\sqrt{2}$ times slower than the upwind method, but with twice the accuracy. It is clearly faster than the MacCormack method.

For a given Δx and J, the three methods require the same number of variables so there is no memory overhead involved when implementing the two step methods numerically. This is important especially when the model is adapted to higher dimensions.

5.4 Conclusions

Several numerical solvers were used to compute the solitary wave solution of the foam drainage equation. The accuracy and performance of the rival solvers was compared and one method was found to significantly save on computation time and memory. We conclude that a numerical method must be selected to maximise the following criteria,

- accuracy - the truncation error of the method should tend to zero as the mesh is refine
- speed - the method is chosen as it computes the solution faster that other methods
- efficiency - the numerical method does not store or need any overhead variables

The future implementation of these methods lies in the coupling of the foam drainage equation with other equations to model systems of interest to foam physicists. Future examples are likely to include solving metal foam problems in three spatial dimensions, and modelling the path of a sphere falling through a foam by coupling the drainage equation to Fluent.

5.5 Acknowledgements

Thanks are due to Simon Cox and Phil Yecko for their useful comments and discussions.

Chapter 6

Metal Foams

6.1 Introduction

In general cellular materials are highly porous and though rigid, have a low specific weight; therefore it is not surprising that they are frequently found as construction materials in nature, for example human bones and plant stalks are cellular. The combination of porosity, rigidity and low specific weight allows plants to support their own weight while including mechanisms for the transport of fluids. It is not surprising that cellular materials have been developed for use in many industrial applications - common examples include the cushioning in seats and insulation boards in the construction industry.

For over forty years, scientists and engineers have been attempting to produce porous metallic structures. Fabrication processes are now well advanced and sheets of metallic foam are commercially available. Their present industrial applications lie in the automobile manufacture industry [26], with possibilities for future use in the lightweight construction of space-frames made from aluminum foam sandwiches [27]. However, many challenges remain in understanding the physical processes of metallic foam formation,

[84].

Metallic foams are particularly interesting cellular materials to study, as they offer a unique combination of the properties of the constituent metal (or metallic alloys) on one hand, with the properties of the porous structure on the other hand, while yielding a rigid lightweight structure. The foams are excellent at energy absorption, have reduced thermal and electrical conductivities and are easy to recycle [27].

Successful attempts have been made to model metallic foam formation. Körner and Singer [85] have developed a model, based on the cellular automaton technique, to simulate the formation and evolution of metal foam produced from metal powder mixed with a blowing agent. In this Chapter we present numerical and analytical analysis [70] of the solidification processes that occur during one particular metallic foam fabrication process. Our aim is to understand how starting parameters modify the final density profile of the solidified foam. Ideally, we wish to find a set of starting parameters that will yield a roughly homogeneous finished product.

6.1.1 Metallic foam formation processes

The current production methods used for the fabrication of metallic foams have recently been reviewed by Banhart and Baumeister [86]. The processes are classified according to the state of the starting metal - liquid, powdered or ionized. We are interested in foams made from metal powders, and in particular those made using the Fraunhofer Process. These foams are produced using a powdered metallurgical method invented and patented at the Fraunhofer Institute in Bremen, Germany, [67, 68, 69].

In the Fraunhofer process, metal powders are mixed with a foaming agent, [86]. The mixture is compressed to yield a dense, semi-finished precursor

product. Prior to foaming, the precursor material may be processed into a variety of shapes and placed in a mold. The precursor is heated to its melting point causing the release of the foaming agent, which is homogeneously distributed with the dense metallic matrix. The melting of the precursor is accompanied by foaming, causing the structure to expand yielding a highly porous metallic foam. The sample is then immediately cooled to trap this foam structure in a solid, closed cell foam. The density of the metallic foam may be controlled by adjusting various foaming parameters - such as the difference between the melting point and heating temperature.

The solidification process now begins - and this is the process we wish to model. We assume the foam has a fixed volume and a uniform liquid density at this *starting* point. Gravity induced foam drainage begins, causing liquid to drain through the network of Plateau borders in the structure. At the same time, and depending on boundary conditions, the foam is cooling from the outside in, causing solidification fronts to form which change the state of the liquid to solid. Clearly drainage must continue until the sample is entirely solidified - and so the evolving sample consists of a solid outer region surrounding by a draining liquid core. The cross section of a metal foam produced using this process is shown in Figure 6.1.

6.2 The physical processes of metallic foam formation

In order to model metallic foam formation, we must make some simple assumptions about the underlying physical processes occurring, while still keeping the key features of the problem. We seek to write down equations which govern the evolution of the system described above, section 6.1.1.

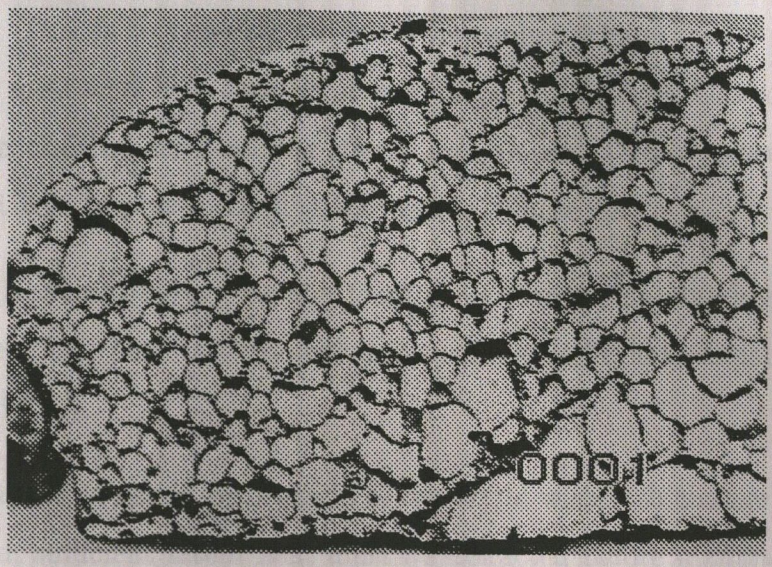

Figure 6.1: A cross sectional cutting of a metal foam reveals the existence of a clearly defined network of solidified Plateau borders (dark regions) formed around bubbles with greatly varying radii (light regions). The aim of our model is to suggest initial conditions that may lead to a more homogeneous final product. Picture courtesy of John Banhart.

The initial configuration of the system is one of an 'idealised' wet monodisperse foam, surrounded by a network of Plateau borders with some uniform cross sectional area A_{Pb}. We assume that all the wet metallic liquid is constrained to flow within this network of Plateau borders. The local liquid fraction, or relative density Φ_l, is the fractional percentage of liquid contained within the closed volume system. As the foam drains, the local relative density must change as liquid moves from one region of the sample to another - and the local bubble diameter, D, must alter in response.

Several cooling processes will occur in the metal foam. We assume that most of the heat will diffuse out of the system along the Plateau border arms via conduction, (there will be some additional cooling due to mass transport of the liquid within the Plateau borders, and this will speed up the cooling

process). This is in contrast to insulating polyurethane foams where the dominant method of heat transfer occurs via gas conduction. Gas conduction, convection and radiative cooling effects are ignored. Two processes have an important role to play in cooling the sample. These are

Specific heat capacity: As the foam cools from some starting temperature, T_{init}, heat is extracted due to the specific heat capacity of the liquid, C_p.

Latent heat: When a local region of the liquid wishes to change state to a solid, sufficient latent heat must be extracted before *a change of state* may occur.

The latter process is the dominant method of heat extraction in this foam solidification process, as the melt is normally only a few degrees Kelvin above the solidification temperature, T_{crit}, of the metal (or metallic alloy), [86]. We assume the viscosity, η, of the liquid, varies smoothly with temperature. Initially, the liquid is fluent, with a correspondingly low viscosity. As the system approaches T_{crit} it becomes viscous and the local viscosity rises. Solid local regions in the foam have a viscosity high enough to cut off further drainage.

The partial differential equation which governs the local liquid fraction is the foam drainage equation, Chapter 5, [3, 8, 9]. This equation had not previously been tested in the context of metal foams - and was altered to account for the viscosity of the foam.

As the foam drains, regions of high and low local liquid density form. This may lead to regions of solidified metal surrounding large holes of gas. Regions of low local density may also form causing film rupture and coalescence. If the local density drops below some critical value, its value is fixed at

that critical value and the local bubble diameter D is increased to simulate coalescence. The total liquid fraction, Φ_l, is altered to maintain the required mass conservation.

6.2.1 Drainage

As the foam drains, the diameter of the gas bubbles, D, and the Plateau border cross-sectional area, Φ_l, alter spatially and temporally in the sample. N is defined as the number of identical independent Plateau borders crossing a plane in a given orientation. The relationship between the liquid fraction, Φ_l and the cross sectional area is

$$\Phi_l = NA \tag{6.1}$$

The drainage equation is obtained from the continuity equation, section A.5,

$$\frac{\partial(NA)}{\partial t} + \nabla(NAu) = 0. \tag{6.2}$$

The volume flow rate per Plateau border Q_l, was defined in Chapter 5 as

$$Q_l = A_{Pb}u \tag{6.3}$$

and the total volume flow rate is defined as

$$Q_l^{TOT} = NA_{Pb}u \tag{6.4}$$

6.2.2 Heat diffusion and mass transport

Consider a liquid or solid foam, where the temperature, T, is not constant throughout, [87], and where the local temperature $T(\tilde{\mathbf{x}}, t)$ varies both spatially and temporally. The vector rate of heat flow $\tilde{\mathbf{Q}}_h$, is defined as

$$\tilde{\mathbf{Q}}_h = -\kappa \nabla T \tag{6.5}$$

where $\kappa(\Phi_l)$ is the thermal conductivity of the liquid. The net rate of heat flow out of a volume of the foam is

$$\frac{dE}{dt} = \int\int \tilde{\mathbf{Q}}_h \cdot \tilde{\mathbf{dS}} \tag{6.6}$$

where $\tilde{\mathbf{dS}}$ is an element of the boundary surface.

The specific heat capacity, C_p, is defined as an association between the amount of heat produced dE with a temperature change of dT,

$$dE = -\int\int\int (C_p \Phi_l \rho dT)\, dV \tag{6.7}$$

where dV is an element of volume.

The rate of heat loss then depends on the rate of temperature change

$$\frac{dE}{dt} = -\int\int\int C_p \Phi_l \rho \frac{\partial T}{\partial t} dV \tag{6.8}$$

However, the liquid within our foam is moving and so we must account for this. Using the substantive derivative, Equation 6.8 is rewritten as

$$\frac{dE}{dt} = -\int\int\int C_p \Phi_l \rho \left(\frac{\partial T}{\partial t} + \tilde{\mathbf{u}} \nabla T\right) dV \tag{6.9}$$

Equation 6.6 is transformed from a surface to a volume integral using Gauss' Divergence Theorem,

$$\begin{aligned} \int\int \tilde{\mathbf{Q}}_h \cdot \tilde{\mathbf{dS}} &= \int\int\int \nabla \cdot \tilde{\mathbf{Q}}_h dV \\ &= -\int\int\int \nabla \cdot (\kappa \nabla T)\, dV \end{aligned} \tag{6.10}$$

Equating equation 6.9 and equation 6.10 gives,

$$\int\int\int \nabla (\kappa \nabla T)\, dV = \int\int\int C_p \Phi_l \rho \left(\frac{\partial T}{\partial t}\right) dV$$

and for any element of volume we have

$$C_p \Phi_l \rho \left(\frac{\partial T}{\partial t} + u \nabla T\right) = \nabla \cdot (\kappa \nabla T) = \nabla \cdot \tilde{\mathbf{Q}}_h \tag{6.11}$$

6.2.3 Viscosity

The viscosity of the metal is conveniently used to describe whether the foam is in a liquid or solid state. When the local temperature of the foam is well above the critical solidification temperature, T_{crit}, we expect high liquid flow rates provided by a small viscosity, $\eta_0 \sim 1$. When the local temperature of the foam is near the critical solidification temperature, we expect low flow rates provided by a high viscosity, $\eta_{max} \sim \infty$. To achieve this we define the viscosity η as a step function

$$\eta = \eta_0 + \frac{(\eta_{max} - \eta_0)}{1 + exp(w_\eta(T - T_{crit}))}. \tag{6.12}$$

The parameter w_η effectively defines the width of the solidification region in the foam - as it controls the narrow range of temperature for which the viscosity changes from η_0 to η_{max}.

6.2.4 Latent heat

A quantity of heat must be extracted from the system before it can change state from liquid to solid. This quantity is defined as the latent heat of solidification, L_f. This is incorporated into the equations by modifying the specific heat of the system,

$$C_p = C_0 + \frac{L_f w_L}{\sqrt{\pi}} \exp\left(-\left(w_L(T - T_{crit})\right)^2\right) \tag{6.13}$$

Equation 6.13 describes a barrier in the specific heat, around the solidification temperature, ensuring sufficient energy is spent in the change of state. w_L defines the range in temperature of this barrier.

6.3 Numerical methods

In this section we describe techniques used to solve the system of coupled equations 6.2, 6.11, 6.12 and 6.13. We assume that our sample is a monodisperse foams where $N = 1$. N only changes due to coalescence - which we ignore in the following discussions.

6.3.1 Dimensionless form of the metal foam equations

Initially we simplify our model by considering only one spatial dimension, z, and write equations 6.2, 6.11, 6.12 and 6.13 in dimensionless form by making appropriate substitutions, [9, 88]. The details involved are quite tedious and are provided in Appendix A.5.

We define $z = \zeta z_0$, $A = \alpha z_0^2$, $\widehat{\Phi}_l = \alpha$, $t = \tau t_0$, $\rho = \hat{\rho}\rho_0$, $g = \hat{g}g_0$, $\eta* = \eta_0\hat{\eta}$, $Q_l = \hat{Q}_l Q_l^0$ and we rewrite equation 6.2 in dimensionless form

$$\frac{\partial \alpha}{\partial \tau} + \frac{\partial \hat{Q}_l}{\partial \zeta} = 0 \quad \text{where} \tag{6.14}$$

$$\hat{Q}_l = \frac{1}{\hat{\eta}}\left(\hat{\rho}\hat{g}\alpha^2 - \frac{\sqrt{\alpha}}{2}\frac{\partial \alpha}{\partial \zeta}\right) \tag{6.15}$$

and

$$z_0 = \sqrt{\frac{C\gamma}{\rho_0 g_0}}, \; t_0 = \frac{\eta^* z_0}{\sqrt{C\gamma}}, \; Q_l^0 = \frac{C^2\gamma^2}{\eta^*\rho_0 g_0}$$

T_0 is the temperature of the infinite cooling bath, T_{crit} the solidification temperature of the metal, and T_{init} is the initial temperature of the entire sample at $t = 0$. We define Θ by $T = \Theta(T_{init} - T_0) + T_0$, $C_p = \hat{C}_p C_0$, $\kappa = \hat{\kappa}\kappa_0\Phi_l$, $Q_h = \hat{Q}_h Q_h^0$ The dimensionless form of equation 6.11 is

$$\hat{\rho}\hat{C}_p\hat{\Phi}_l\left(\frac{\partial \Theta}{\partial \tau} + \frac{\hat{Q}_l}{\alpha}\frac{\partial \Theta}{\partial \zeta}\right) = \frac{1}{Pe}\frac{\partial}{\partial \zeta}\left(\hat{\kappa}\hat{\Phi}_l\frac{\partial \Theta}{\partial \zeta}\right) \tag{6.16}$$

$$\hat{Q}_h = \frac{1}{Pe}\left(\hat{\kappa}\hat{\Phi}_l\frac{\partial \Theta}{\partial \zeta}\right) \tag{6.17}$$

where the Peclet number is defined as $Pe = \frac{z_0^2 \rho_0 C_0}{\kappa_0 t_0}$

The dimensionless viscosity is defined as

$$\hat{\eta} = 1 + \frac{\frac{\eta_{max}}{\eta_0 - 1}}{1 + \exp(w_\eta(\Theta - \Theta_{crit}))} \tag{6.18}$$

and the dimensionless specific heat capacity is defined as

$$\hat{C}_p = 1 + \frac{\hat{L}_f w_c}{\sqrt{\pi}} exp\left(-(w_c(\Theta - \Theta_{crit}))^2\right) \tag{6.19}$$

and $L_f = \hat{L}_f C_0$

An analysis for the two dimensional case is provided in Appendix A.5.

6.3.2 Boundary conditions

No fluid may flow into or out of the sample - the total amount of liquid in the system is conserved, i.e.

$$\widehat{Q}_l = 0 \qquad (1d) \tag{6.20}$$

at the top and bottom of the foam, or

$$\left.\begin{aligned} \widehat{Q}_{l\zeta} &= 0 \\ \widehat{Q}_{l\xi} &= 0 \end{aligned}\right\} \qquad \text{(2d)} \tag{6.21}$$

where $\widehat{Q}_{l\zeta}$ is the flow rate in the vertical z-direction and $\widehat{Q}_{l\xi}$ the flow rate in the horizontal x-direction.

Initially the entire foam sample is at some uniform temperature, T_{init}, such that $\Theta = 1$. The sample may be cooling from any side where $T_0 = 0 \Rightarrow \Theta = 0$. The solidification temperature, T_{crit}, is chosen near the initial temperature of the system.

Five different scenarios are considered

Case I A 1d foam sample is cooled from the top and the bottom with $\Theta_0 = 0$, Figure 6.2 (left)

Case II A 1d foam sample is cooled from the bottom only, no heat is allowed escape from the top of the sample, Figure 6.2 (right)

Case III A 2d foam sample is cooled from both sides and from the top and bottom, Figure 6.15

Case IV A 2d foam sample is cooled from the top and bottom only, no heat is allowed escape from the sides of the sample, Figure 6.17

Case V A 2d foam sample is cooled from the sides only, no heat is allowed escape from the top and bottom of the sample, Figure 6.19

The condition for no heat loss is

$$\frac{\partial \Theta}{\partial \zeta} = 0 \qquad (1d) \tag{6.22}$$

or

$$\left.\begin{array}{l} \frac{\partial \Theta}{\partial \zeta} = 0 \\ \frac{\partial \Theta}{\partial \xi} = 0 \end{array}\right\} \qquad (2d) \tag{6.23}$$

6.3.3 Discretisation

Our numerical code solves equations 6.14, 6.15, 6.16, 6.17, 6.18 and 6.19 using explicit finite differencing schemes describe in Chapter 5.

At each time step

- $\widehat{\eta}$ is calculated from the temperature at the previous time steps
- $\widehat{Q}_l$ is calculated from $\widehat{\eta}$ and $\widehat{\Phi}_l$ at the previous time steps
- $\widehat{\Phi}_l$ is calculated using the updated values of $\widehat{Q}_l$ and $\widehat{\eta}$
- $\widehat{Q}_h$ is calculated from the old values of Θ

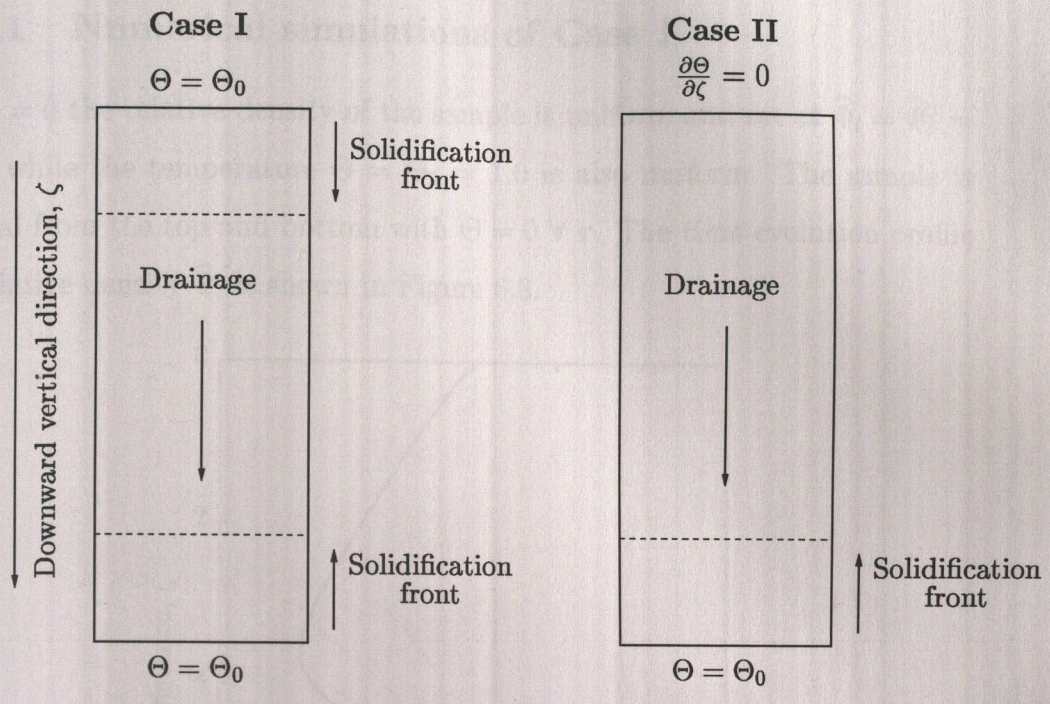

Figure 6.2: A sketch of the first two 1d cases considered. In Case I, the sample is cooled from both the top and bottom. In Case II, the sample is cooled from the bottom only.

- $\widehat{C}_p$ is calculated from the old values of Θ
- Finally the temperature, Θ is found

The two dimensional equations are solved in a similar manner.

6.4 Results for one dimensional calculations

In this section we present results for the two one dimensional cases, Case I & II. A detailed account of numerical results is presented and analytical models are derived for both Cases. The aim of these models is to identify the initial parameters that will produce a homogeneous metallic foam.

6.4.1 Numerical simulations of Case I

At $\tau = 0$ the relative density of the sample is uniform and set at $\widehat{\Phi}_l = \widehat{\Phi}_l^0 = 0.01$ while the temperature $\Theta = \Theta_0 = 1.0$ is also uniform. The sample is cooled from the top and bottom with $\Theta = 0 \; \forall \; \tau$. The time evolution profile of relative density $\widehat{\Phi}_l$ is shown in Figure 6.3.

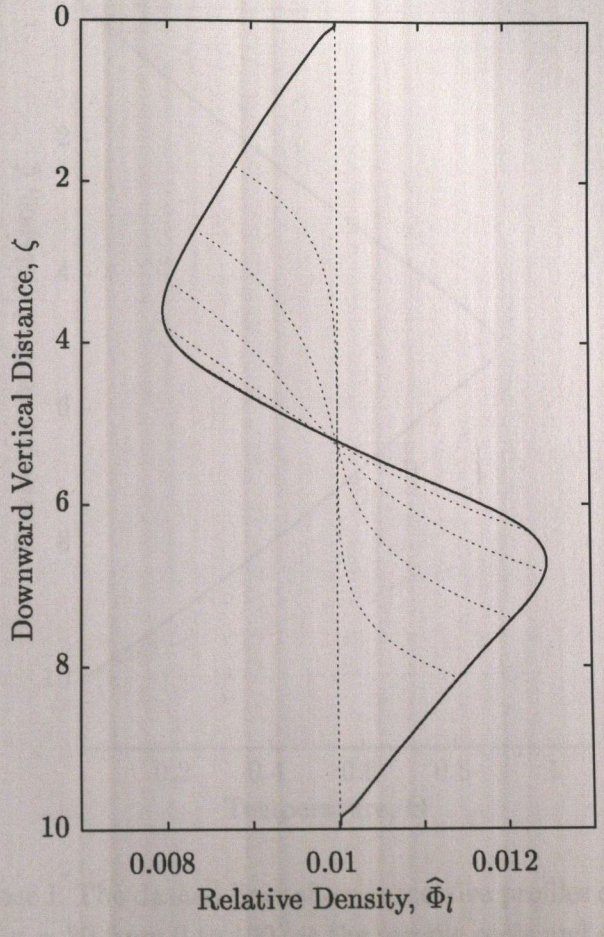

Figure 6.3: Case I. Liquid metal is draining vertically in the sample as cooling fronts, originating at the top and bottom, move through the foam causing solidification. The dashed lines show successive profiles of relative density in increments of $\tau = 20$ up to $\tau = 100$. The solid line shows the final, solidified, relative density profile at $\tau = 133$. $\widehat{\Phi}_l^0 = 0.01$ and $Pe = 1.0$

In the early stages of time evolution, the relative density at the top of

the sample decreases as liquid drains down towards the center of the foam. At the same time, a solidification front moves down from the top of the sample and solidifies the liquid metal - leaving a roughly linear profile of *decreasing* relative density with slope M_d. At the bottom of the foam the

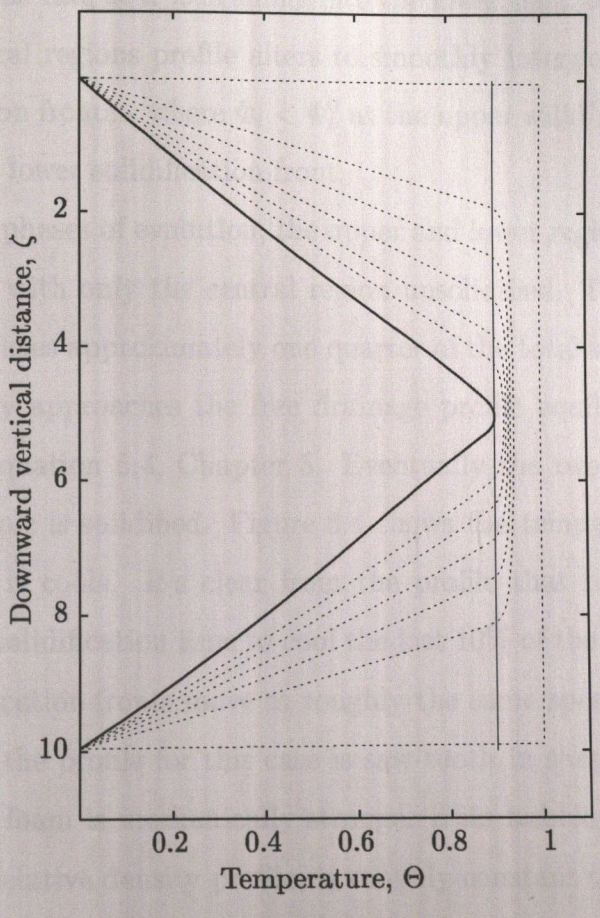

Figure 6.4: Case I. The dashed lines show successive profiles of the temperature, in increments of $\tau = 20$ from 0 to 120, as the sample cools and solidifies. The solid curved line is the final temperature profile of the solidified sample at $\tau = 133$. The solid vertical line is the solidification temperature, $\Theta_{crit} = 0.9$.

relative density is increasing while a solidification front moves up through the sample solidifying the liquid metal. This also yields a roughly linear profile of relative density with slope M_u - but *increasing* in this case. When

$\widehat{\Phi}_l \lesssim 0.05$, $M_d \approx M_u$.

The relative density at the centre of the sample remains approximately constant at early times in the profiles evolution, Figure 6.3. Effectively, liquid is being fed into the central region from the upper part of the sample at roughly the same rate as it is draining into the lower part. At later evolution times the central regions profile alters to smoothly interpolate between the two solidification fronts - where $\Phi_l < \Phi_l^0$ at the upper solidification front and $\Phi_l > \Phi_l^0$ at the lower solidification front.

In the final phases of evolution, the upper and lower regions of the sample are solidified - with only the central region unsolidified. The profile in this region, which takes approximately one quarter of the total solidification time to form, closely approaches the free drainage profile equilibrium profile as described by equation 5.4, Chapter 5. Eventually the two fronts meet and the entire sample is solidified. Figure 6.4 shows the temperature profile for the sample as it cools. It's clear from the profile that it takes roughly a quarter of the solidification time to cool the last 10% of the sample, and that the two solidification fronts move at roughly the same speed.

In general, the profile for this case is saw-tooth in shape and is undesirable. A metal foam is mechanically stronger if its bubble distribution size, and hence its relative density profile, is roughly constant throughout.

Simple checks

A number of basic tests may be performed to ensure the numerical model is accurately describing physical reality. In particular, we would expect the total solidification time of the sample, τ_s, to scale as $\tau_s \propto L_\zeta^2$ - Figure 6.5 shows a plot of L_ζ^2 against τ and this is indeed the case.

Furthermore, we would expect τ_s to scale as $\tau_s \propto \frac{1}{\widehat{\kappa}_0}$ - Figure 6.6 shows a

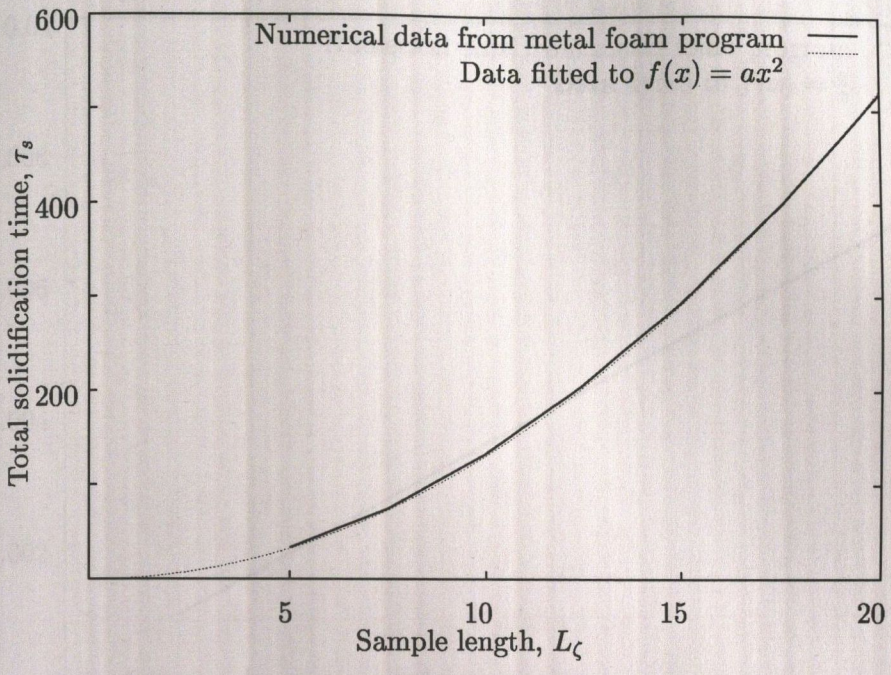

Figure 6.5: Case I. The total solidification time, τ_s, is proportional to the square of the length, L_ζ, of the foam sample. The solid curve shows values produced by the numerical metal foam program. The dashed curve is a square fit of $f(x) = ax^2$. $\widehat{\Phi}_l^0 = 0.01, Pe = 1$

plot of $\widehat{\kappa}_0$ against τ, verifying this.

6.4.2 Numerical simulations of Case II

At $\tau = 0$ the relative density and temperature of the sample are uniform, $\widehat{\Phi}_l = \widehat{\Phi}_l^0 = 0.01$, $\Theta = \Theta_0 = 1.0$ The sample is cooled from the bottom *only* so $\Theta(\zeta = 0) = 0$, but Neumann boundary conditions are applied at the top

$$\frac{\partial \Theta}{\partial \zeta} = 0 \tag{6.24}$$

so no heat can flow in or out of the sample there. The evolution profile of relative density, $\widehat{\Phi}_l$, is shown in Figure 6.7.

In the early stages of evolution, the relative density at the bottom of the

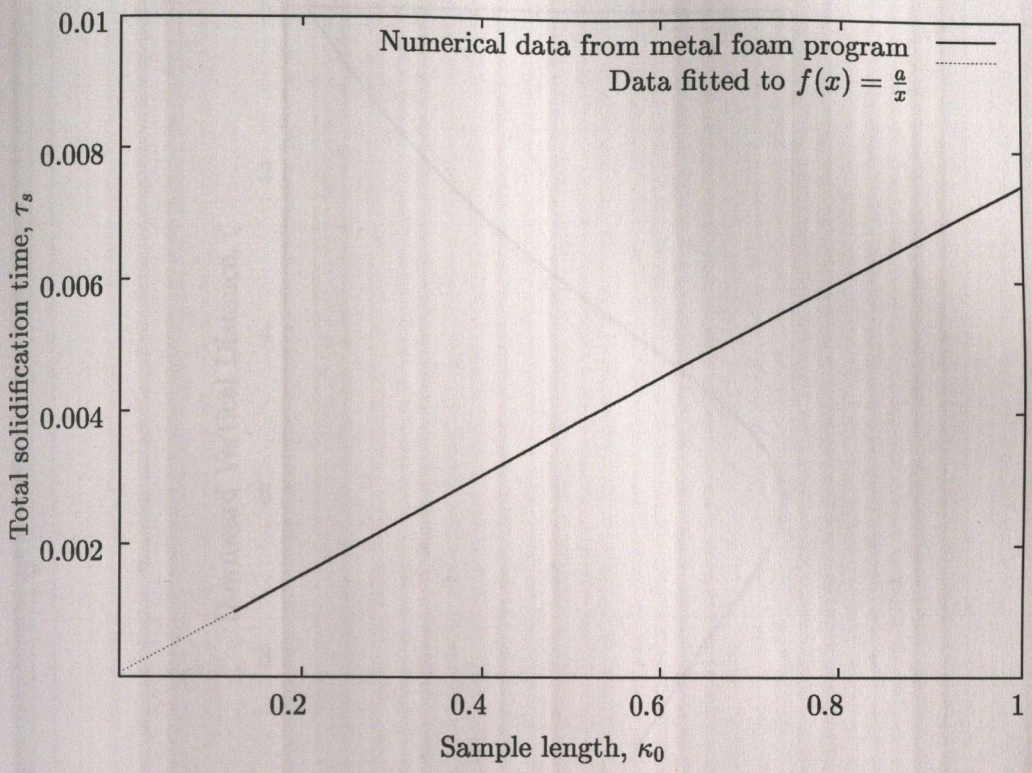

Figure 6.6: Case I. The total solidification time, τ_s, is inversely proportional to the thermal conductivity, $\widehat{\kappa}_0$, of the metal. The solid curve shows values produced by the numerical metal foam program. The dashed curve is an inverse fit of $f(x) = \frac{a}{x}$. $\widehat{\Phi}_l^0 = 0.01, Pe = 1$

sample increases as liquid drains down through the foam. At the same time a solidification front moves up from the bottom of the sample. This produces a roughly linearly *increasing* profile of relative density.

The remaining part of the sample has the relative density profile of a foam draining under free drainage - but with the length of the free drainage sample, $L_{effective}$, shrinking as the solidification front moves up through the foam.

In the final phases of evolution the lower part of the sample has solidified while the profile of the rest of the sample approaches the equilibrium solution

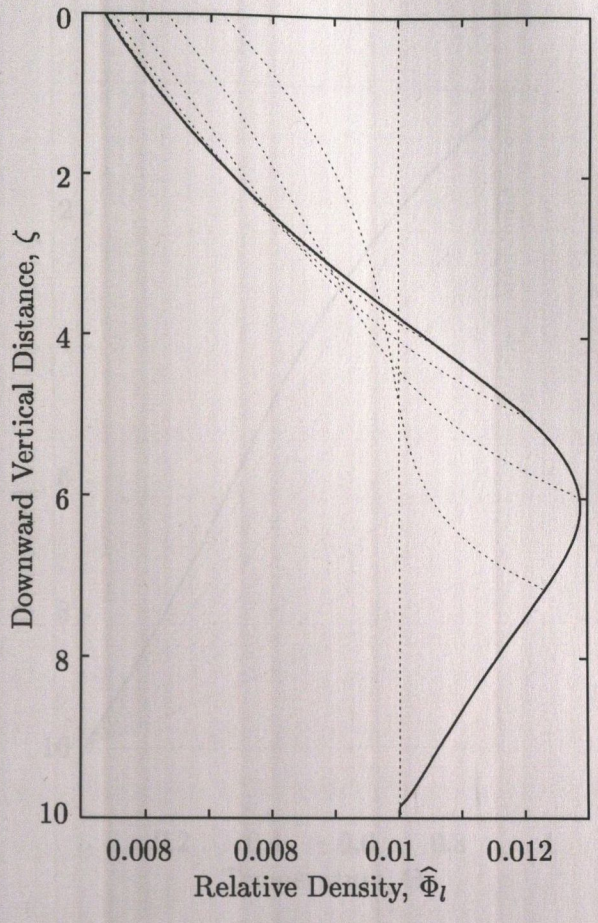

Figure 6.7: Case II. Liquid metal drains vertically in the sample as a solidification front, originating at the bottom, moves up through the foam. The dashed lines show successive profiles of relative density in increments of $\tau = 50$ from 0 to $\tau = 200$ The solid line shows the final, solidified, relative density profile at $\tau = 430$. $\widehat{\Phi}_l^0 = 0.01$ and $Pe = 1.0$

of a foam under free drainage. It is clear from Figure 6.7 that drainage has ceased long before the sample has completely solidified.

6.4.3 Analytical approximation of Case I

The apparent linearity of the relative density profiles at the top and bottom of the foam sample in Figure 6.3, and the success of the tests in section 6.4.1,

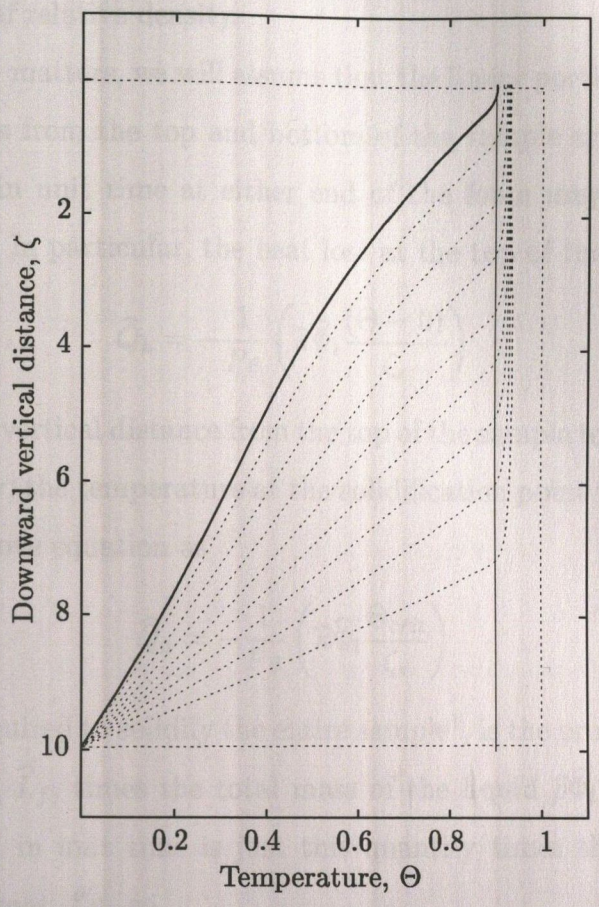

Figure 6.8: Case II. The dashed lines show successive profiles of the temperature, in increments of $\tau = 50$ from 0 to 400, as the sample cools and solidifies. The solid curved line is the final temperature profile of the solidified sample at $\tau = 430$. The solid vertical line is the solidification temperature, $\Theta_{crit} = 0.9$

suggest that it may be possible to derive an analytical description of the solidification process. Liquid may not leave the confines of the sample, it may only solidify, so the system must conserve mass.

There are a number of steps in calculating the variation of the relative density profile. We must find a time dependent equation which governs the distance the solidification fronts travel in unit time. The quantity of liquid which has drained in unit time is also calculated. From this we can calculate

the variation of relative density.

To simplify matters, we will assume that the linear portions of the relative density profiles from the top and bottom of the sample are identical. Then the heat lost in unit time at either end of the foam may be described by equation 6.17. In particular, the heat lost at the top of the sample is

$$\widehat{Q}_h = -\frac{1}{Pe}\left(\widehat{\kappa}\widehat{\Phi}_l \frac{(\Theta - 0)}{\zeta_s}\right) \tag{6.25}$$

where ζ_s is the vertical distance from the top of the sample to the solidification front. However, the temperature at the solidification point is Θ_{crit} so we may rewrite the above equation as

$$\widehat{Q}_h = -\frac{1}{Pe}\left(\widehat{\kappa}\widehat{\Phi}_l \frac{\Theta_{crit}}{\zeta_s}\right) \tag{6.26}$$

The energy required to solidify the entire sample[1], is the product of the latent heat of fusion, $\widehat{L}_f$, times the total mass of the liquid $\widehat{\rho}\widehat{\Phi}_l$. The amount of heat extracted in unit time is just this quantity times the velocity of the solidification front, $\frac{\partial \zeta_s}{\partial \tau}$, so

$$\widehat{L}_f \widehat{\rho}\widehat{\Phi}_l \frac{\partial \zeta_s}{\partial \tau} = \frac{1}{Pe}\left(\widehat{\kappa}\widehat{\Phi}_l \frac{\Theta_{crit}}{\zeta_s}\right) \tag{6.27}$$

Integrating equation 6.27 and taking the square root gives

$$\zeta_s = \sqrt{\frac{1}{Pe}\left(\frac{2\widehat{\kappa}\Theta_{crit}}{\widehat{L}_f \widehat{\rho}}\right)\tau}. \tag{6.28}$$

Equation 6.27 enables the position of the front to be found as a function of time. The position of the solidification front moving up from the bottom of the sample may be found in a similar manner by replacing ζ_s with $L - \zeta_s$ and reproducing the previous derivation.

[1] We ignore the role the specific heat capacity plays in the extraction of heat from the system as it is minor compared to the role played by the latent heat.

Consider the solidification front moving down from the top of the sample. The volume of liquid drained from the top of the sample to the solidification front at position ζ_s may be approximated as

$$V = -\frac{1}{2}\zeta_s^2 \frac{d\widehat{\Phi}_l}{d\zeta}. \tag{6.29}$$

where $\frac{d\widehat{\Phi}_l}{d\zeta}$ is the slope of the roughly linear density profile of the advancing solidification front, see Figure 6.9. The relative density at this point is simply $\widehat{\Phi}_l - \zeta_s \frac{d\widehat{\Phi}_l}{d\zeta_s}$

It is clear from Figure 6.3 that at early evolution times the relative density in the central region of the sample remains unchanged. The liquid draining through this region must have a constant flow rate - and has drained from the top of the foam. For each local region of the foam, the local flow rate, $\widehat{Q}_l$, is just the amount of liquid transferred from one region to the next in unit time. If the flow rate at the centre of the sample, $\zeta_{\frac{L}{2}}$, remains constant at $\widehat{Q}_l^0$, then the total flow rate, and hence the total volume of drained liquid past $\zeta_{\frac{L}{2}}$ must be the flow rate per unit time, multiplied by the total elapsed time τ.

So, at the solidification front

$$\frac{1}{2}\zeta_s^2 \left(-\frac{d\widehat{\Phi}_l}{d\zeta}\right) = N\widehat{Q}_l\tau \tag{6.30}$$

Using ζ_s from equation 6.28, and ignoring the diffusive term in equation 6.15, we obtain

$$\frac{\widehat{\Phi}_l}{d\zeta} = -\left(\frac{2N\tau}{\widehat{\kappa}}\right)\left(\frac{1}{\zeta_s^2}\right)\widehat{Q}_l^0 \tag{6.31}$$

$$= \left(\frac{2N\tau}{\widehat{\kappa}}\right)\left(\frac{Pe\widehat{L}_f\widehat{\rho}}{2\widehat{\kappa}\Theta_{crit}\tau}\right)\left(\frac{1}{\widehat{\eta}}\left(\widehat{\rho}\widehat{g}(\widehat{\Phi}_l^0)^2\right)\right) \tag{6.32}$$

$$= \left(\frac{Pe\widehat{L}_f\widehat{\rho}^2\widehat{g}(\widehat{\Phi}_l^0)^2}{\widehat{\kappa}\widehat{\eta}\Theta_{crit}}\right) \tag{6.33}$$

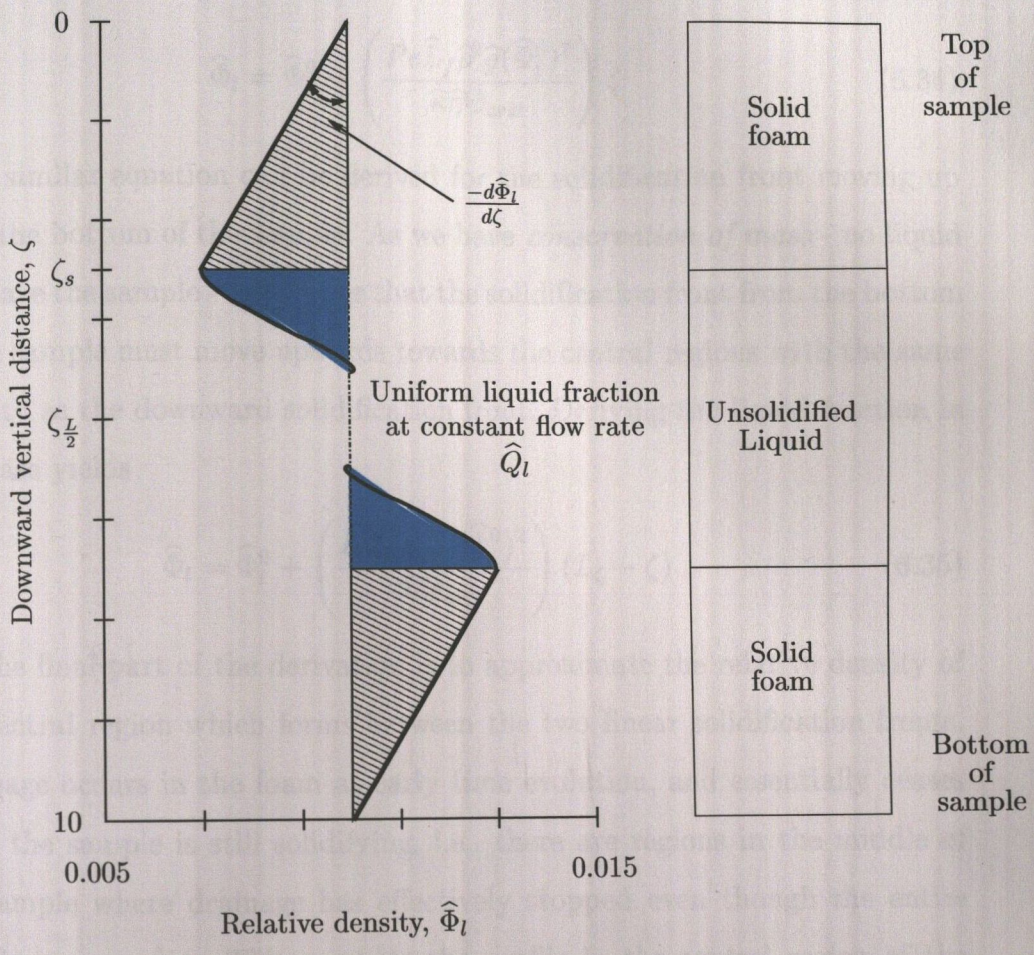

Figure 6.9: A schematic diagram of the relative density profile for Case I at an early evolution time. The relative density at the top of the sample is *decreasing* linearly while the relative density at the bottom of the sample is *increasing* linearly. The total decrease of liquid in the upper part of the sample is shown as the top shaded and cyan triangles, while the total increase in liquid in the lower regions is shown as the lower shaded and cyan triangles, where $\zeta = \zeta_s$. However, the total loss/gain of liquid in equation 6.29 is approximated as the areas under the shaded triangles only.

- the slope of the relative density at the top of the foam.

Integrating equation 6.30 yields the variation of relative density in the

top portion of the sample at early time evolution

$$\widehat{\Phi}_l = \widehat{\Phi}_l^0 - \left(\frac{Pe\widehat{L}_f \widehat{\rho}^2 \widehat{g} (\widehat{\Phi}_l^0)^2}{\widehat{\kappa}\widehat{\eta}\Theta_{crit}} \right) \zeta \tag{6.34}$$

A similar equation can be derived for the solidification front moving up from the bottom of the sample. As we have *conservation of mass* - no liquid can leave the sample - we assume that the solidification front from the bottom of the sample must move upwards towards the central regions with the same velocity as the downward solidification front. Deriving the liquid fraction in this case yields

$$\widehat{\Phi}_l = \widehat{\Phi}_l^0 + \left(\frac{Pe\widehat{L}_f \widehat{\rho}^2 \widehat{g} (\widehat{\Phi}_l^0)^2}{\widehat{\kappa}\widehat{\eta}\Theta_{crit}} \right) (L_\zeta - \zeta) \tag{6.35}$$

The final part of the derivation is to approximate the relative density of the central region which forms between the two linear solidification fronts. Drainage occurs in the foam at early time evolution, and essentially ceases while the sample is still solidifying, i.e. there are regions in the middle of the sample where drainage has effectively stopped even though the entire sample is not solid. This suggests the profile in the central region of the foam is a trivial solution of the foam drainage equation, where the flow rate throughout this region is $\widehat{Q}_l = 0$. The solution of the foam drainage equation in the case of a sample of length L_ζ with a liquid fraction of $\widehat{\Phi}_l^L$ at $\zeta = L$ is

$$\widehat{\Phi}_l = \frac{1 \quad \zeta)^2}{\left(\widehat{\Phi}_l^L + L - \zeta \right)^2} \tag{6.36}$$

The equilibrium profile at the centre of our metal foam sample may be written as

$$\widehat{\Phi}_l = \frac{1}{\left(\widehat{\Phi}_l^0 + \frac{L}{2} - \zeta \right)^2} \tag{6.37}$$

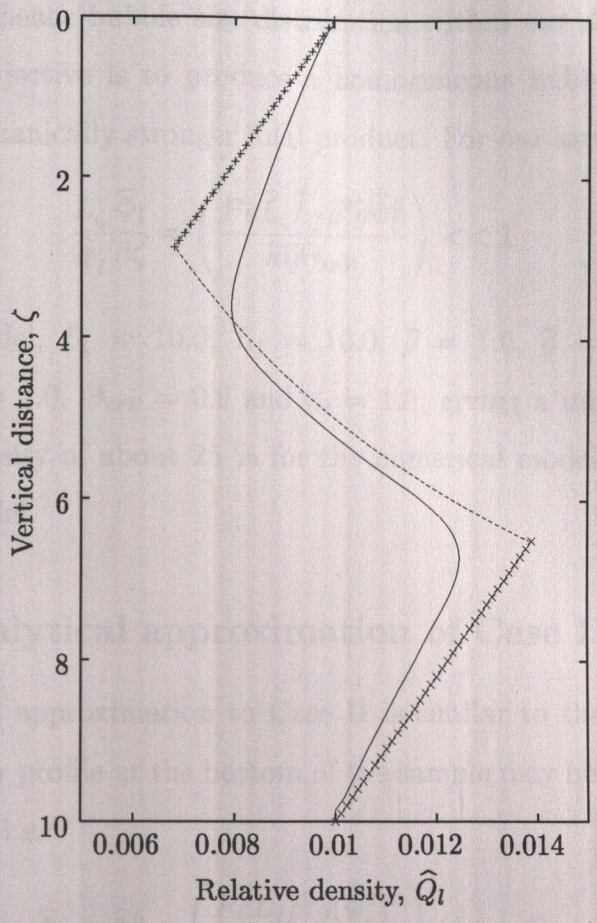

Figure 6.10: Case I. The numerical (solid line) and analytical relative density profiles of the solidified metal foam sample are shown. The approximations used in the analytic method cause it to over calculate the slope of the density profiles.

where the relative density is clearly $\widehat{\Phi}_l^0$.

The various analytical solutions are combined to approximate the variation of relative density throughout the sample. The combined analytical solution is compared with the full numerical solution in Figure 6.10. It is clear that the agreement between the two methods is good. It should now be possible to use our analytical results to make some useful predictions and conclusions about the final profile of a metal foam without performing numerical calculations. Equation 6.30 describes the variation of the relative

density - and hence bubble size distribution within our sample. As stated earlier, the objective is to produce a homogeneous bubble distribution to provide a mechanically stronger final product. For our sample, we require

$$\frac{L_\zeta}{\widehat{\Phi}_l}\frac{\widehat{\Phi}_l}{d\zeta} = \left(\frac{Pe\widehat{L}_\zeta\widehat{L}_f\widehat{\rho}^2\widehat{g}\widehat{\Phi}_l^0}{\widehat{\kappa}\widehat{\eta}\Theta_{crit}}\right) << 1 \tag{6.38}$$

In our model, $L_\zeta = 10.0$, $L_f = 10.0$, $\widehat{\rho} = 1.0$, $\widehat{g} = 1.0$, $\widehat{\Phi}_l^0 = 0.01$, $N = 1.0$, $\widehat{\kappa}_0 = 1.0$, $\Theta_{crit} = 0.9$ and $\eta_0 = 1.0$, giving a maximum deviation from homogeneity of about 25 % for the numerical model and 40% for the analytical model.

6.4.4 Analytical approximation of Case II

The analytical approximation to Case II is similar to that of Case I. The relative density profile at the bottom of the sample may be approximated by equation 6.35, i.e.

$$\widehat{\Phi}_l = \widehat{\Phi}_l^0 + \left(\frac{Pe\widehat{L}_f\widehat{\rho}^2\widehat{g}(\widehat{\Phi}_l^0)^2}{\widehat{\kappa}\widehat{\eta}\Theta_{crit}}\right)(L_\zeta - \zeta) \tag{6.39}$$

and the relative density profile from the top of the sample may be described by an equilibrium profile, $\widehat{\Phi}_l(\widehat{\Phi}_s, \zeta_s)$. These two profiles meet at $\zeta = \zeta_s$, $\widehat{\Phi} = \widehat{\Phi}_s$, so we can write an analytical solution if we can calculate ζ_s and Φ_l^s.

We again appeal to conservation of mass (liquid). The total amount of liquid

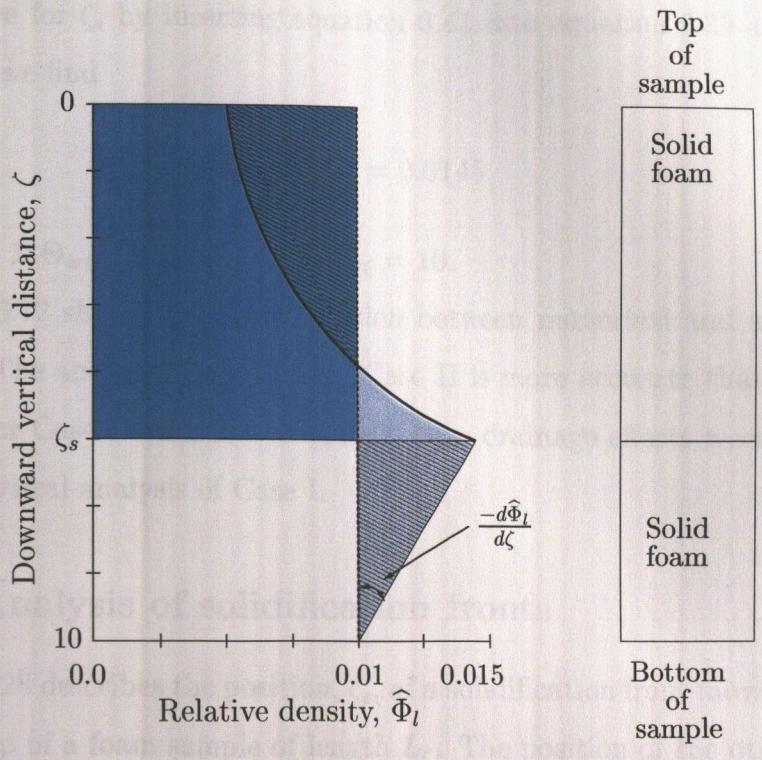

Figure 6.11: Case II. A schematic representation of the drainage profile during early time evolution. The relative density at the bottom of the sample increases linearly while the remaining profile approximates that of a free draining foam.

under the equilibrium profile, Figure 6.11, (the non shaded blue and cyan regions) is equal to the total amount of liquid under in the shaded and non shaded cyan regions, minus the total amount of liquid under the shaded and non shaded blue regions. Mathematically this equates to

$$\zeta_s\sqrt{\widehat{\Phi}_s}\left(\zeta_s+\frac{1}{\sqrt{\widehat{\Phi}_s}}\right)^{-1}=\zeta_s\widehat{\Phi}_0-\frac{1}{2}C(L_\zeta-\zeta_s)^2 \tag{6.40}$$

At the solidification point, equation 6.39 describes the relative density $\widehat{\Phi}_l$ at ζ_s, and may be written as

$$\widehat{\Phi}_s=\widehat{\Phi}_l^0+C(L_\zeta-\zeta_s) \tag{6.41}$$

where $C=\left(\frac{Pe\widehat{L}_f\widehat{\rho}^2\widehat{g}(\widehat{\Phi}_l^0)^2}{\widehat{\kappa}\widehat{\eta}\Theta_{crit}}\right)$

We solve for ζ_s by inserting equation 6.41 into equation 6.39 and using *Maple* [89] we find

$$\zeta_s = 5.94, \widehat{\Phi}_s = 0.0145 \tag{6.42}$$

when $Pe = 1, \Theta_{crit} = 0.9, \widehat{\Phi}_l^0 = 0.01, L_\zeta = 10$.

Figure 6.12 shows a good correlation between numerical and analytical solutions. The analytical solution for Case II is more accurate than the one produced for Case I - this is because diffusive drainage effects were ignored in the analytical analysis of Case I.

6.4.5 Analysis of solidification fronts

Equation 6.28 describes the position, ζ_s, of a solidification front moving down from the top of a foam sample of length L_ζ. The position of the other front moving up from the bottom of the sample is simply $L_\zeta - \zeta_s$. According to our simplified analytical theory of Case I, these two fronts should meet exactly in the middle of the sample, Figure 6.13.

The position of the solidification fronts may be calculated using our numerical code, and a comparison of the analytical and numerical description of the processes is shown in Figure 6.13. The numerical fronts do not meet exactly in the centre of the sample as the moving liquid is itself contributing a term to the heat flux equation. The greater the liquid fraction the greater the contribution of moving liquid to heat flux, and the more pronounced the shift off center becomes. Nevertheless, it is obvious from the plot that the analytical and numerical fronts are in close agreement.

Equation 6.28 may also be used to estimate the total solidification time.

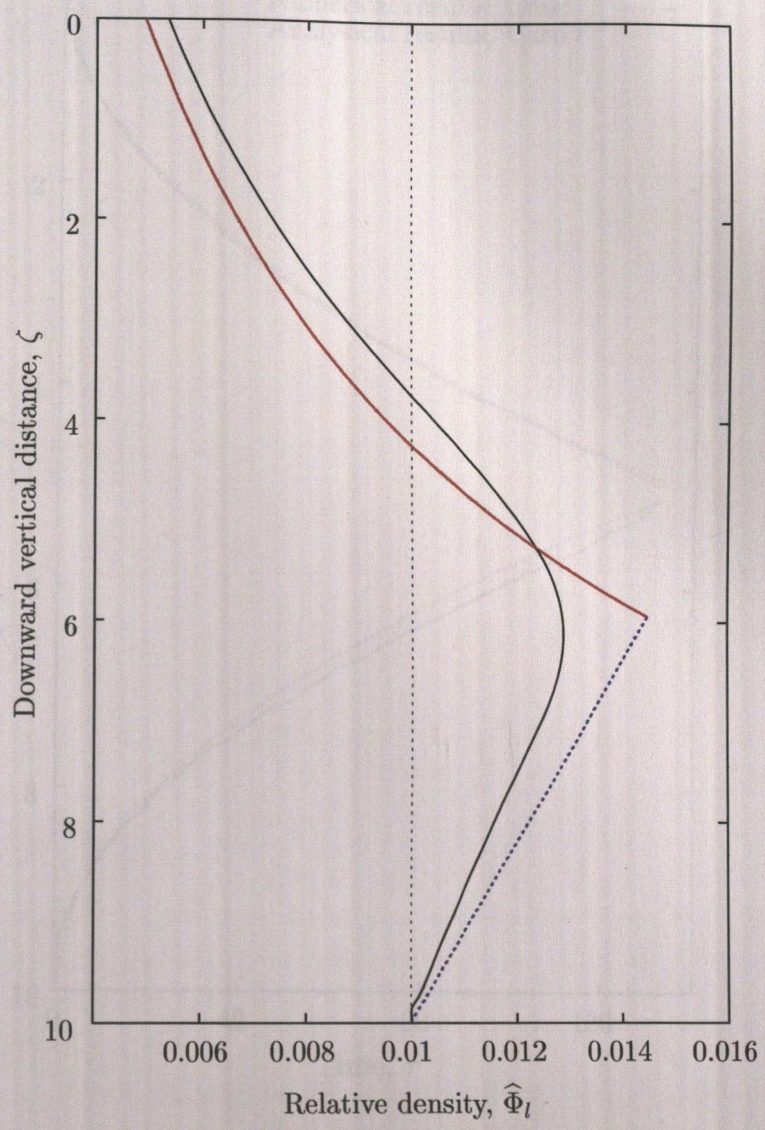

Figure 6.12: Case II. The solid black lines shows the solidified relative density profile produced from the numerics. The blue and red lines show the two distinct parts of the analytic approximation. The dashed line shows the initial relative density profile.

The sample is totally solidified when both fronts reached $\zeta = \frac{L_\zeta}{2}$

$$\tau_s = \frac{Pe\widehat{L}_f\widehat{\rho}\zeta^2_{\frac{L_\zeta}{2}}}{2\widehat{\kappa}\Theta_{crit}} = \frac{Pe\widehat{L}_f\widehat{\rho}L^2_\zeta}{8\widehat{\kappa}\Theta_{crit}} \tag{6.43}$$

With the stated parameters of our numerical model, the time taken for

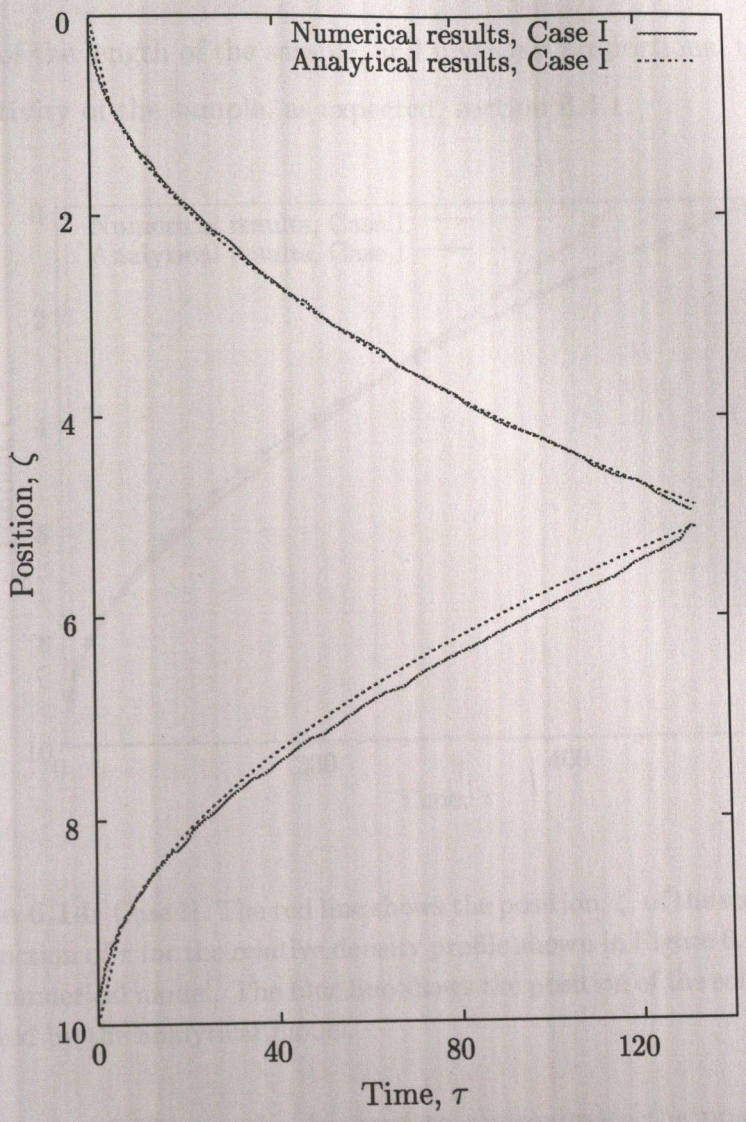

Figure 6.13: The solid line shows the position, ζ, of the solidification fronts against time, τ, for the profile shown in Figure 6.3, as calculated by the numerical model. The dashed line shows the position, ζ, of the solidification fronts against time, τ, as produced by the analytical model. There is close agreement between the two plots.

the entire sample to solidify is $\tau_s^{numerical} \approx 133$, while the analytical model suggests $\tau_s^{analytical} \approx 139$ from equation 6.43. Furthermore, equation 6.43 clearly indicates that the total solidification time, τ_s, is proportional to the

square of the length of the sample, and inversely proportional to the thermal conductivity of the sample, as expected, section 6.4.1.

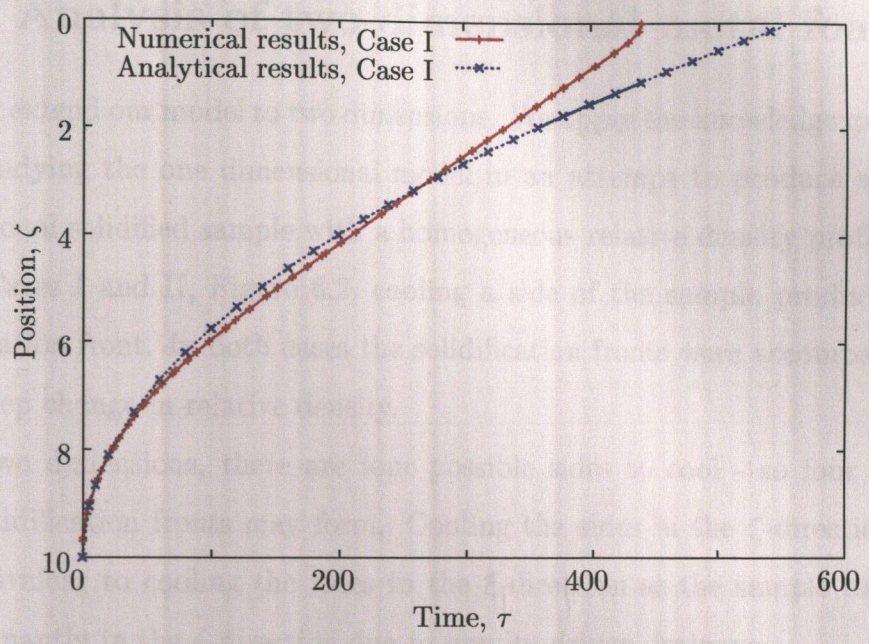

Figure 6.14: Case II. The red line shows the position, ζ, of the solidification front as a function of τ for the relative density profile shown in Figure 6.12, as calculated by the numerical model. The blue line shows the position of the solidification fronts produced by the analytical model.

Equation 6.28 may also be used to approximate the position, ζ_s, of the solidification front moving up through the foam sample of length L_ζ, in Case II. This front must solidify the entire sample. A comparison between analytical and numerical calculations, Figure 6.14, shows a good agreement at early evolution only. Nevertheless, an approximate solidification time can be obtained, from equation 6.28, for Case II

$$\tau_s = \frac{Pe\widehat{L}_f\widehat{\rho}\zeta_{L_\zeta}^2}{2\widehat{\kappa}\Theta_{crit}} = \frac{Pe\widehat{L}_f\widehat{\rho}L_\zeta^2}{2\widehat{\kappa}\Theta_{crit}} \tag{6.44}$$

With the stated parameters of our numerical model, the time for the entire

sample to solidify is $\tau_s^{numerical} \approx 430$, while our analytical model suggests $\tau_s^{analytical} \approx 555$ from equation 6.43.

6.5 Analysis of two-dimensional metal foams

We now extend our model to two dimensions. We apply the knowledge gained from studying the one dimensional model in an attempt to produce a two dimensional solidified sample with a homogeneous relative density profile.

In Cases I and II, Figure 6.2, cooling a side of the sample produced a solidification front. In both cases the solidification fronts were accompanied by a steep change in relative density.

In two dimensions, there are four possible sides to cool - so four possible solidification fronts may form. Cooling the sides in the ζ-direction is not equivalent to cooling the sides in the ξ-direction as the sample drains predominantly in the ζ-direction due to gravity driven drainage.

We consider three cases

Case III, where the sample is cooled from all sides with boundary conditions, $T = T_{init} = 0$, Figure 6.15

Case IV, where the sample is cooled from the top and bottom, $T = T_{init} = 0$, and insulated on the sides, $\frac{\partial T}{\partial z} = 0$, Figure 6.17

Case V, where the sample is cooled from the sides , $T = T_{init} = 0$, and insulated at the top and bottom $\frac{\partial T}{\partial x} = 0$, Figure 6.19

6.5.1 Numerical simulation of Case III

In Case III, Figure 6.15, the sample drains predominantly in the ζ-direction causing a large shift in the relative density. In the early stages of evolution the

relative density at the top of the sample decreases as liquid drains towards the middle of the sample, while the relative density at the bottom of the sample increases.

As the sample cools, solidification fronts move down from the top, up from the bottom, and in from the sides of the sample causing the liquid metal to solidify with a linear relative density profile in the in the ζ and ξ directions.

The relative density at the sides of the sample, away from the gravity driven drainage fronts, remains roughly constant as little drainage occurs in the ξ direction. The solidification fronts from the sides of the sample quickly move inwards preventing these regions from draining in the ζ direction.

At early stages of evolution, the relative density profile at the center of the sample remains roughly constant as fluid is draining out of the central regions as quickly as it drains into them. In the final phases of evolution, the entire sample - bar the centre - has solidified. This can clearly be seen in a temperature profile, Figure 6.16. The solidified relative density profile in the center of the sample is similar to a free drainage profile.

6.5.2 Numerical simulation of Case IV

In Case IV, Figure 6.17, drainage occurs predominantly in the ζ-direction causing a large shift in the relative density of the sample. In the early stages of evolution the relative density at the top of the sample decreases roughly linearly as liquid drains towards the middle of the sample. At the same time a solidification front moves down from the top of the sample. At the bottom of the sample the relative density increases while a solidification front moves upwards. The increase in relative density is roughly linear.

The relative density in the middle of the sample remains roughly constant

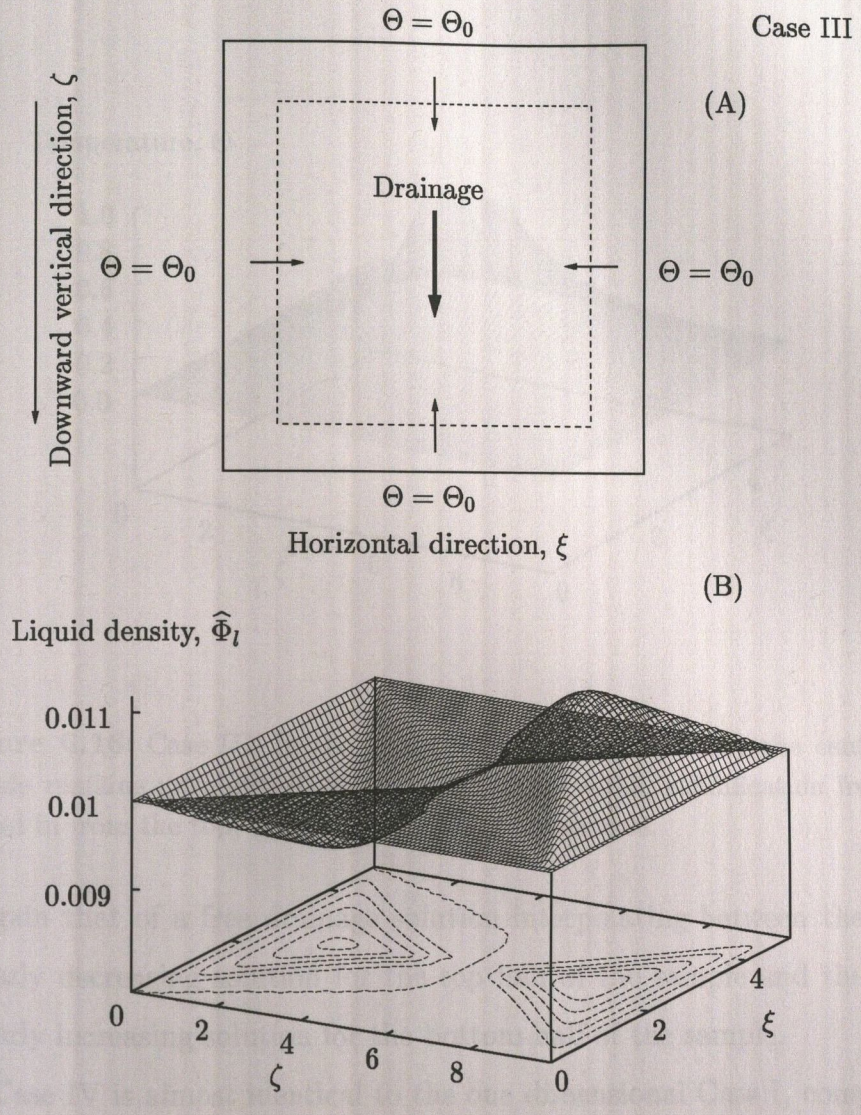

Figure 6.15: Case III. (Top) shows a schematic of a two dimensional sample being cooled from all sides. Four solidification fronts form at the sides of the sample and move inwards as it cools - dashed lines. The sample drains predominantly in the ζ-direction due to gravity driven drainage, but also drains in the ξ-direction. (Bottom) shows the final relative density profile of the sample - which is highly inhomogeneous.

until the final phases of evolution. The final profile of the central region

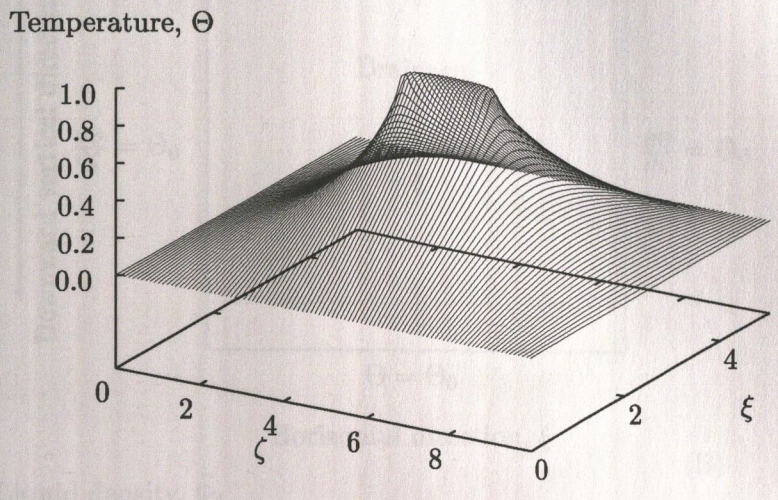

Figure 6.16: Case III. In the final phases of evolution, only the centre of the sample remains unsolidified. $\Theta_{init} = 1.0$, $\Theta_{crit} = 0.9$, solidification fronts have moved in from the top, bottom and sides of the sample.

is again that of a free drainage solution interpolating between the roughly linearly decreasing solution for the top half of the sample and the roughly linearly increasing solution for the bottom half of the sample.

Case IV is almost identical to the one dimensional Case I, compare Figure 6.3 with Figure 6.17. The ξ direction plays no significant role in the formation of the solid foam in Case IV as virtually no drainage occurs in the ξ direction, and no solidification fronts form.

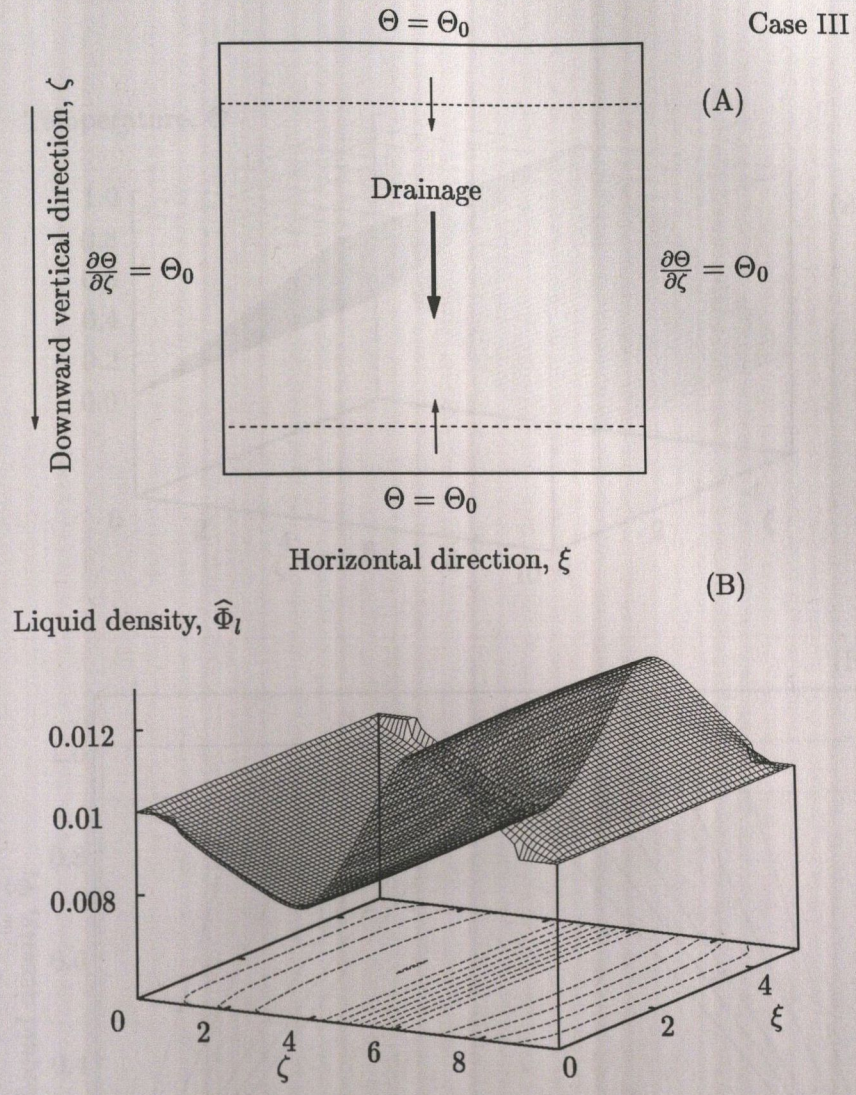

Figure 6.17: Case IV. (A) shows a schematic of a two dimensional sample being cooled from the top and bottom only. Solidification fronts form at these sides of the sample and move inwards as it cools - dashed lines. The sample drains predominantly in the ζ-direction due to gravity driven drainage, but also drains in the ξ-direction. (B) shows the final relative density profile of the sample. The relative density profile viewed from the ζ-direction is identical to the profile of Case I.

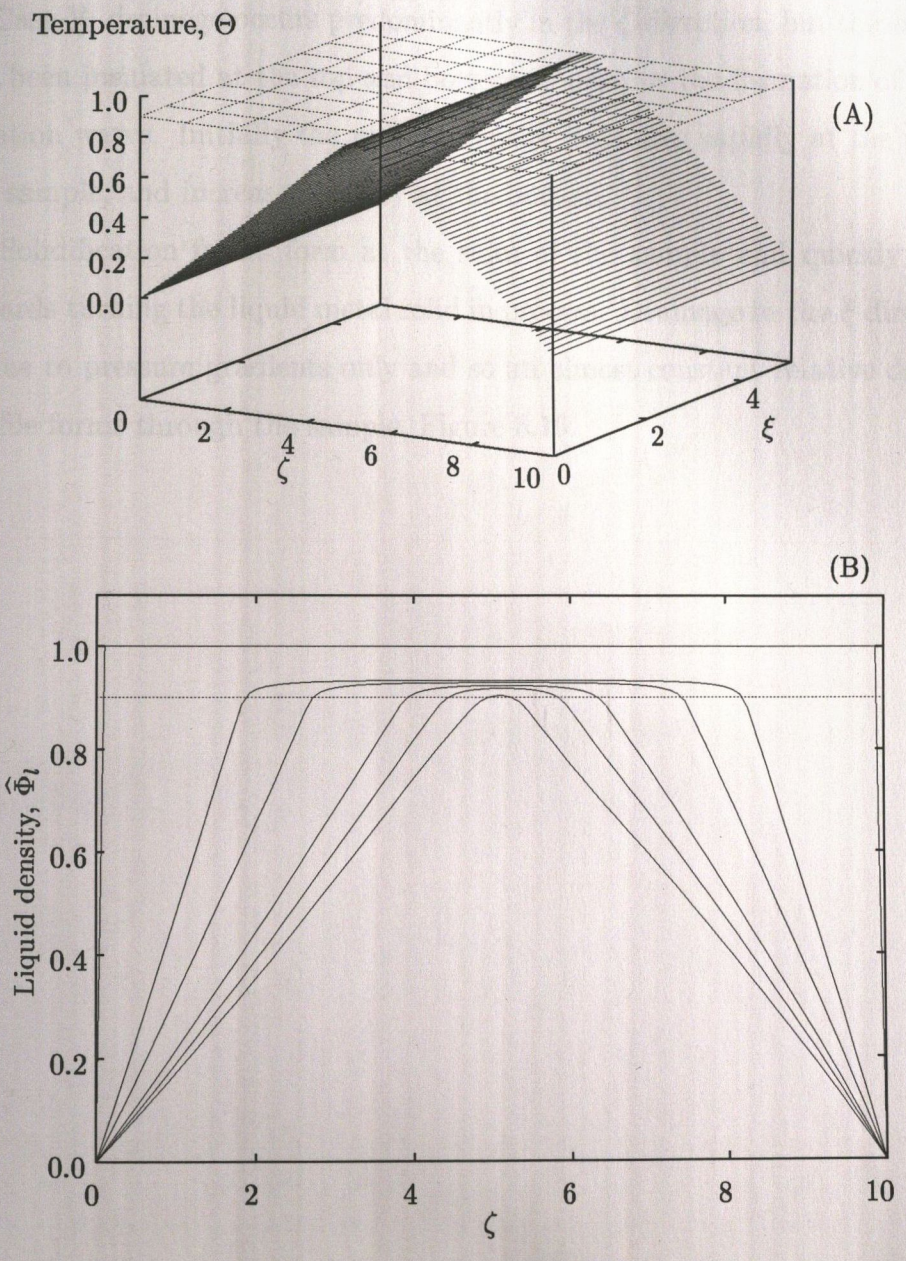

Figure 6.18: Case IV. (A) A 3d view of the final temperature profile. (B) A side on view of the temperature profiles from $\tau = 0$ to $\tau = 100$, in increments of 20. The temperature profile is identical to its one dimensional counterpart, Case I, Figure 6.4. The final profile is at $\tau = 133$.

6.5.3 Numerical simulation of Case V

In Case V, drainage occurs predominantly in the ζ-direction, but the sample has been insulated at the top and bottom to prevent the formation of solidification waves. Initially the relative density decreases rapidly at the top of the sample, and increases rapidly at the bottom.

Solidification fronts form at the sides of the sample and quickly move inwards turning the liquid metal solid in process. Drainage in the ξ direction is due to pressure gradients only and so an almost constant relative density profile forms through the sample, Figure 6.19.

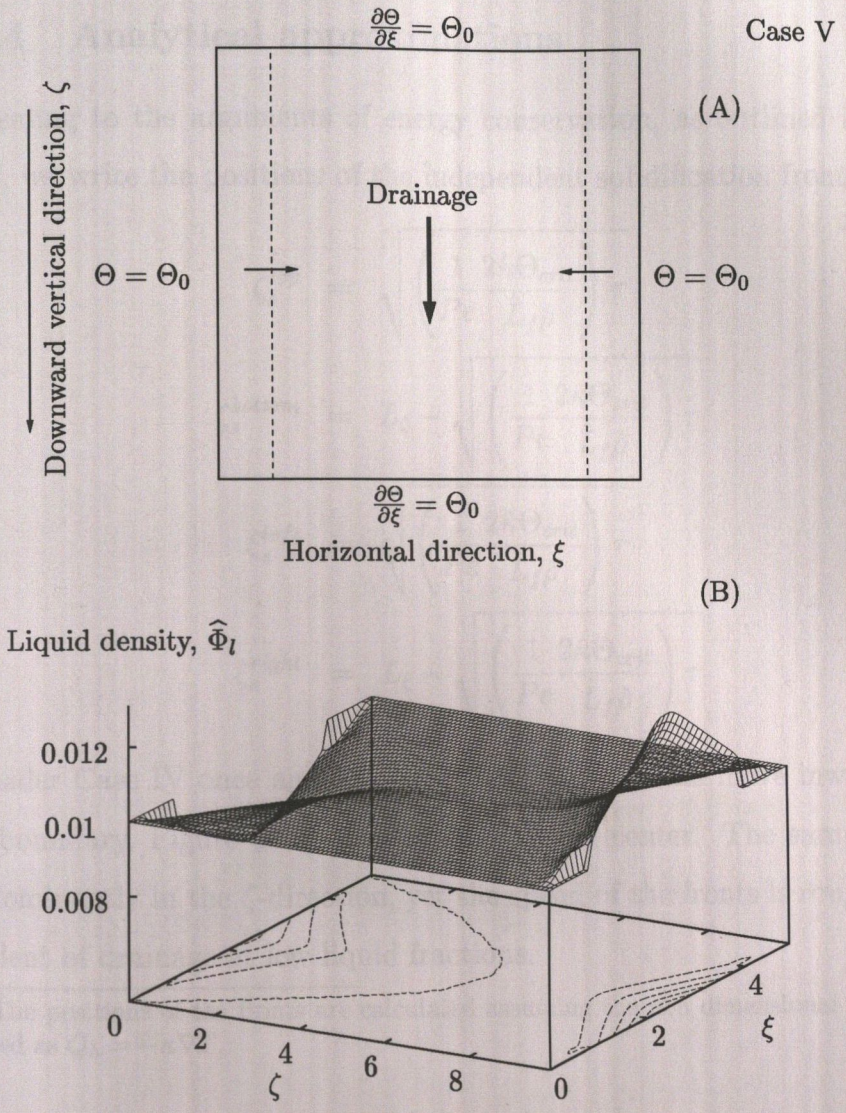

Figure 6.19: Case V. (A) Shown is a schematic of a two dimensional sample being cooled from its vertical sides only. Solidification fronts form at the sides of the sample and move inwards as it cools - dashed lines. The sample drains predominantly in the ζ-direction due to gravity driven drainage, but also drains due to pressure gradients in the ξ-direction. (B) Shown is the final relative density profile of the sample - which is highly inhomogeneous at the ends but completely homogeneous in the center.

6.5.4 Analytical approximations

Appealing to the arguments of energy conservation, as outlined in section 6.4.3, we write the positions of the independent solidification fronts[2] as

$$\begin{aligned}
\zeta_s^{top} &= \sqrt{\left(\frac{1}{Pe}\frac{2\hat{\kappa}\Theta_{crit}}{\hat{L}_f\hat{\rho}}\right)\tau} \\
\zeta_s^{bottom} &= L_\zeta - \sqrt{\left(\frac{1}{Pe}\frac{2\hat{\kappa}\Theta_{crit}}{\hat{L}_f\hat{\rho}}\right)\tau} \\
\xi_s^{left} &= \sqrt{\left(\frac{1}{Pe}\frac{2\hat{\kappa}\Theta_{crit}}{\hat{L}_f\hat{\rho}}\right)\tau} \\
\xi_s^{right} &= L_\xi - \sqrt{\left(\frac{1}{Pe}\frac{2\hat{\kappa}\Theta_{crit}}{\hat{L}_f\hat{\rho}}\right)\tau}
\end{aligned} \tag{6.45}$$

Consider Case IV once again. Four solidification fronts move inwards from the boundary, Figure 6.20, and combine in the center. The sample drains predominantly in the ζ-direction, yet the speed of the fronts is roughly independent of drainage at low liquid fractions.

[2]The positions of the fronts are calculated assuming the non dimensional heat flow is defined as $Q_h = -\kappa\nabla T$

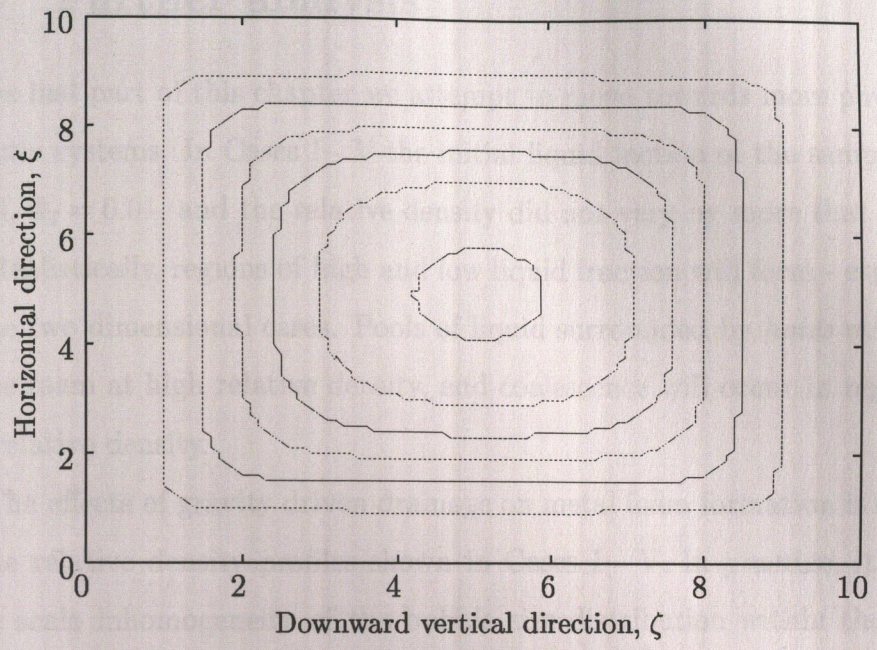

Figure 6.20: Case III. The four solidification fronts combine and move inwards changing the liquid to solid and stopping further drainage as they go. The contours are shown for $\tau = 20$ to $\tau = 100$, at $\tau = 20$ intervals. The innermost contour is at $\tau = 127$, just before the entire foam solidifies at $\tau = 133$. $L_\zeta = L_\xi = 10$, $Pe = 1$, $\Theta_{init} = 1$, $\Theta_{crit} = 0.9$.

In Cases III, IV & V, $L_\zeta = 2L_\xi$. In each case there is a competition between the solidification waves - which depend upon the dimensions of the sample in a particular direction. The time, τ, taken for the solid foam to form is found by applying and solving equations 6.45 to Cases III, IV & V as appropriate. In Case III, $\tau_s^{numerical} \approx 33$ and $\tau_s^{analytic} \approx 35$. For Case IV, $\tau_s^{numerical} \approx 133$ and $\tau_s^{analytic} \approx 139$, which is identical to Case I. For Case V, $\tau_s^{numerical} \approx 33$ and $\tau_s^{analytic} \approx 35$. This simple analysis clearly produces accurate results in two dimensions.

The final profile of Case IV is identical to the final profile of Case I, and may be approximated in the same manner as the one dimensional case.

6.6 Further analysis

In the last part of this chapter we attempt to move towards more physically realistic systems. In Cases I - V the initial liquid faction of the samples was small, $\Phi_l = 0.01$, and the relative density did not vary by more that 40% or so. Realistically, regions of high and low liquid fraction will form - especially in the two dimensional cases. Pools of liquid surrounded by *holes* may form in the foam at high relative density, and coalescence will occur in regions of low relative density.

The effects of gravity driven drainage on metal foam formation is evident in the relative density profiles shown in Cases I - V. In practice, it causes large scale inhomogeneity of the bubble size distribution within the foam, Figure 6.1, reducing the mechanical properties of the finished product - or rendering the sample useless altogether. For this reason, physicists are interested in understanding foam formation in the microgravity environment of space where $g \approx 0.001ms^{-2}$, [90]. A European Space Agency topical team was set up to discuss possible experiments experiments on the International Space Station.

6.6.1 Coalescence

If the relative density is allowed to drop below some critical value, $A < A_{crit}$, the coalescence of films between bubbles will occur. This causes a large change in the local bubble diameter, D, - and hence the overall mechanical stability of the finished product. In practice, this will cause the liquid fraction to decrease locally once coalescence has occurred. Numerically, we allow coalescence to occur by preventing the local liquid fraction from dropping below some critical value - and then fixing it at this value. We simulate the

convergence of two bubbles by increasing N at this point,

$$N_{correction} = \frac{N\,A}{A_{crit}}. \tag{6.46}$$

We define the local bubble cross sectional area in one and two dimensions as $\left(\frac{D}{2}\right)^2$. The gas fraction is defined as $\Phi_g = 1 - \Phi_l$, where $\Phi_g = N\left(\frac{D}{2}\right)^2$.

$$D = \sqrt{\frac{1-\Phi_l}{N\pi}}$$

and setting $A = A_{crit}$ and D accordingly.

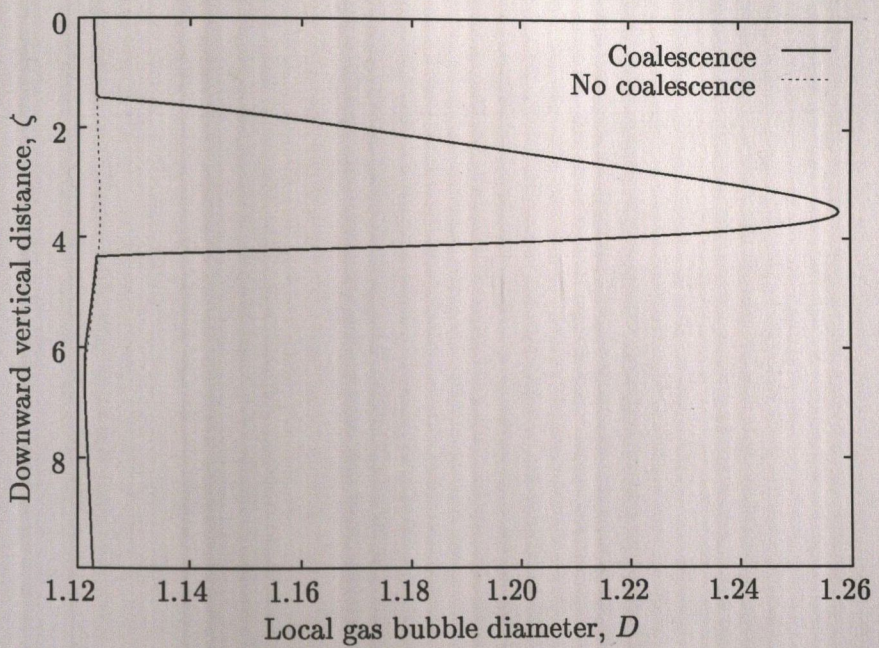

Figure 6.21: Case I. Coalescence occurs when the local liquid fraction drops below some critical value. The adjoining film between two bubbles bursts forming a larger single cell, and reducing the energy of the foam in the process. The local liquid fraction is reduced and the local bubble diameter increases. The variation in the relative density profile is sufficient to produce a slight fluctuation of local bubble diameter.

The variation in bubble diameter for Case I is shown in Figure 6.21. The onset of coalescence effects occurs once the local liquid fraction drops

below $\Phi_{crit} = 0.9\ \Phi_l$. Figure 6.22 shows the same set up for Case III. The relative density is clearly prevented from falling below $0.9\ \Phi_l$ and the bubble diameter is adjusted accordingly. Both these cases are somewhat artificial, but the effects are evident nonetheless.

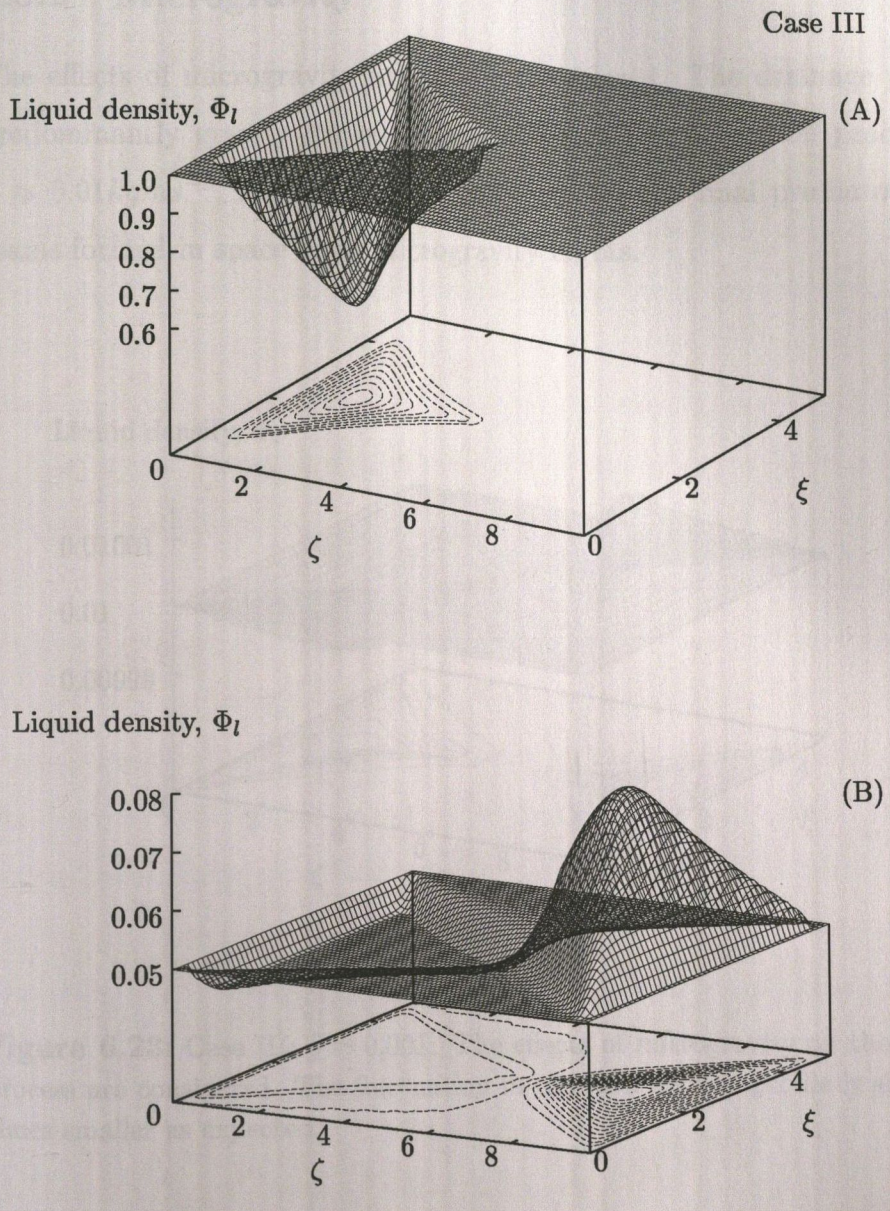

Figure 6.22: Case III: The effects of coalescence on the final bubble diameter distribution, (A), and relative density profile, (B), are shown.

6.6.2 Microgravity

The effects of microgravity are briefly considered. The drainage process is predominantly gravity driven. By looking at the formation process when $g \approx 0.01 kgms^{-2}$, Figure 6.23, we may predict the final profile of metallic foams formed in space or in microgravity flights.

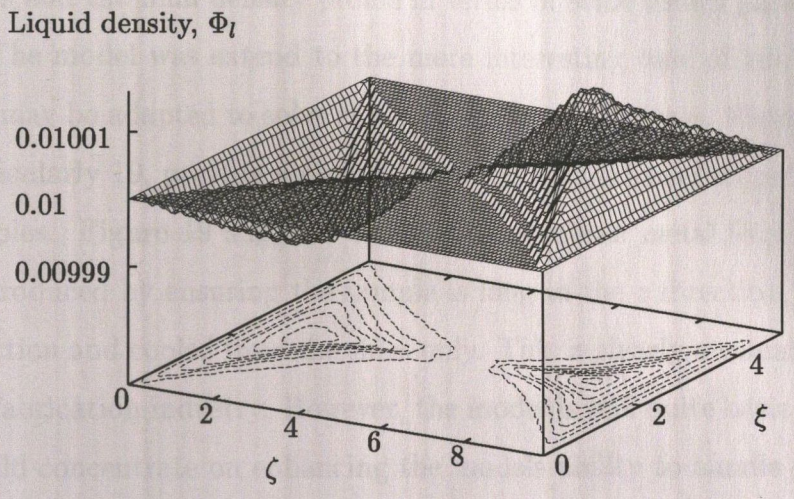

Figure 6.23: Case III: $\widehat{g} \approx 0.001$. The effects of microgravity on the formation process are considered. The fluctuation in the final density profile is simply 1000 times smaller as expected.

6.7 Conclusions

We have produced an idealised numerical and analytical model of a metal foam formation process. This one dimensional model, which couples the equations of liquid drainage and conductive heat transfer, predicts solidification times for the solid foam which are proportional to its length squared and

inversely proportional to its conductivity as required. The model allows for an ad hoc treatment of coalescence, and could produce regions of collapsed foam or pools of liquid depending on its input parameters.

This simple model is capable of tracking the solidification fronts that move through the foam sample as it cools. The analytical model shows good agreement with the numerics and reasonably predicts the final relative density profile in some of the cases. This allows us to predict the solidification times and the final density profile in terms of some initial parameters.

The model was extend to the more interesting case of two dimensions - and may be adapted to solve three dimensional problems. Figures 15, 17 and particularly 19, provide an insight into the formation of more realistic foam samples. Figure 19 suggests that a homogeneous metal foam sample may be produced by ensuring the sample is long in the z direction, thin in the x direction and cooled from the sides only. This is clearly a valuable insight for the fabrication industry. However, the model is still quite basic - future work should concentrate on enhancing the models ability to handle coalescence.

We conclude that this model has provided a good first starting point in predicting the relative density profiles of one and two dimensional foams, and in bridging the gap between present theory and experiment.

6.8 Acknowledgements

Thanks are primarily due to Simon Cox for his development of some of the analytic theory presented in this Chapter. Thanks are also due to Phil Yecko, Guy Verbist and John Banhart for their useful discussions.

Part IV

Calculation details

Chapter 7

Numerical methods

7.1 Introduction

Several numerical tools were used to compute the results in this thesis. This Chapter contains a description of the tools used and instances of their use. The *Surface Evolver*, sections 7.2 - 7.5, and *Fluent*, section 7.6, are the most important of these tools.

7.2 The Surface Evolver

The *Surface Evolver* [13] is the primary tool used for calculations in Chapters 2, 3 and 4.

7.2.1 History

In the early '90s it become evident that the scientific community required computer software capable of modelling and displaying complex three dimensional objects. Principle requirements were for a package capable of modelling Kelvin's structure, and comparing its energy with the energy of rival struc-

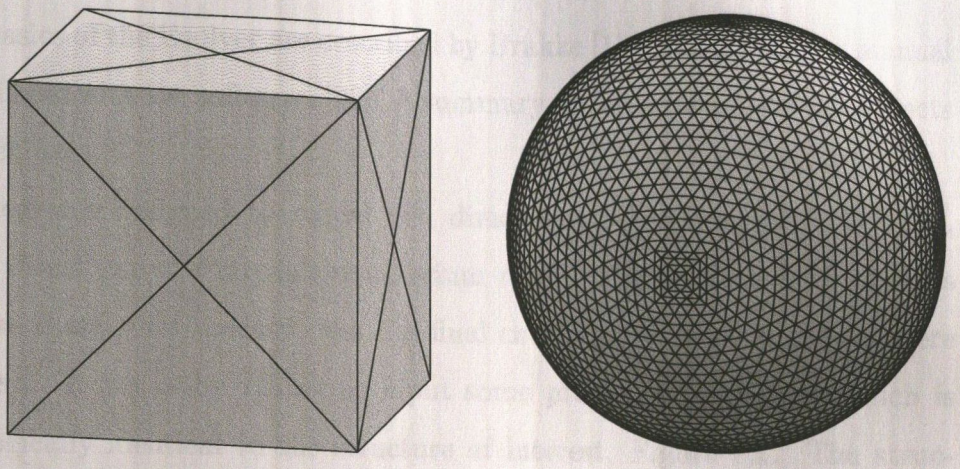

(a) R0 (b) R4

Figure 7.1: Two topologically identical objects: (a) shows a cube composed of flat sided triangular faces, while (b) shows a sphere, also composed of flat sided triangular faces. Both are generated using the Surface Evolver, the cubes surface energy is minimised as it is 'evolved' into the sphere.

tures. The *Surface Evolver* was written by Professor Kenneth Brakke as part of the Geometry Center Project (initially known as the Geometry Supercomputing Project), and is capable of modelling these structures. Applications include simulating the profile of fuel in a rocket tank in microgravity, [91], and calculating the forces on solder joints in printed circuit boards, [92], as well as uses in knot theory.

The software is capable of modelling wet foams, [15], but is unable to model the movement of the fluid within the foam. This must be done by feeding the Evolver output to other programs such as *Fluent* [24].

7.2.2 Evolver Basics

The basics of the Evolver are described by Brakke [13], and a full user manual is available with the software, [93]. A summary of the most important aspects is given here.

Programs designed to model two dimensional foam samples, [94, 95], made direct use of Plateau's equilibrium rules. The Surface Evolver does not use these rules, nevertheless the final converged structure must adhere to them. It works by taking as input some predefined structure which is topologically identical to the structure of interest, Figure 7.1. The structure is made up of *vertices* (or points) in three dimensional space. Vertices are linked together to form ordered pairs of straight *edges*, edges are liked together to form ordered flat *facets* (or faces) with a fixed orientation. A continuous surface is approximated by a mesh of facets.

The normal vector (and hence orientation) of a facet is defined by the right hand rule applied to its loop of edges. A *body* is defined as a list of facets with normals all pointing outwards or inwards, resulting in a body with positive or negative volume respectively.

The surface mesh may be subject to any number of constraints or additional energy terms. Constraints may be geometrical, e.g. restricting selective vertices and edges to a line, or they may be specific integral quantities such as body volumes.

The initial mesh is refined internally by the Evolver to ensure that each facet is made up of only three edges. Mesh refinement causes the parent facets to be subdivided into four child facets, with identical orientation to their parent, and subject to the same constraints and energy terms.

The surface energy is minimised, subject to all constraints, by evolving the surface down a local energy gradient via any number of optional techniques.

Typical methods include gradient descent and conjugate gradient - however, Hessian methods, section 7.2.5, ensure that the surface energy is truly at a local minimum.

Given a flat facet f, with edges $\vec{e}_1, \vec{e}_2, \vec{e}_3$ oriented in a counterclockwise order, the energy of f due to surface tension T may be written as

$$E = \frac{T}{2}||\vec{e}_1 \times \vec{e}_2|| \tag{7.1}$$

Given a vertex v_1, the force exerted on v due to surface tension T may be written as

$$\vec{F}(v_1) = \frac{T}{2}\frac{\vec{e}_2 \times (\vec{e}_1 \times \vec{e}_2)}{||\vec{e}_1 \times \vec{e}_2||} \tag{7.2}$$

A single iteration step in the Evolver

- calculates the forces on all vertices as described by equation 7.2
- sets forces to zero for fixed constraints
- calculates the motion of vertices required to constrain the volumes, forces are then projected to body constraints
- vertices are moved by volume restoring motion and all forces are calculated
- constraints are enforced on vertices
- all volumes, pressures, areas and energies are recalculated

7.2.3 Convergence

The energy of a structure is minimised at each refinement level via any number of processes described above. It is important that a sufficient number of

minimisation steps occur and that the best possible mesh - one with roughly equilateral triangles - is obtained.

The mesh for the entire surface, or selected parts of the surface, may then be refined quadrupling the number of surface facets and the total energy is once again minimised. Technically, the only limitation on the continued process of refinement followed by minimisation is computational power. A power law is used to extrapolate a final energy for the structure based on current and previous energies, and in general it is clear when a surface has converged.

However, under certain circumstances it is not easy to judge when a converged stability point has been reached, (see Brakke [52]). 'Hand tuning' of the convergence process may be required, especially when using constraint functions, or when modelling wet foams. 'Hand tuning' techniques for achieving convergence include

- Area normalisation. The resistance to motion at each vertex is calculated as a force/area rather than just force. This is a better approximation to motion by mean curvature, e.g. soap films
- Area weeding. The removal of small facets and edges from a mesh. If the distribution in facet area is a few orders of magnitude, energy minimisation may be stalled
- Equiangulation. The edge connectivity of adjacent facets may be altered to obtain more equiangular triangles
- Minimisation techniques. Switching from gradient descent to conjugate gradient, or from conjugate gradient to Riebere conjugate gradient to prevent stalling

- Vertex averaging. Each vertex is replaced with the average of the centroids of its adjacent facets. This helps reduce the variation in facet area - providing a smoother mesh

- Saddle. This seeks a minimum energy along the eigenvector of the lowest negative eigenvalue of the Hessian. Avoids stalling problems experienced by conventional minimisation techniques due to a zero or close to zero local gradient. (See section 7.2.5)

- Surface Tension techniques - in wet foams. Decreasing one surface tension against the other as refinement levels are increased. Prevents facets crossing - which is undetected by the Evolver - which would destroy the surface minimisation

- Hessian techniques. Constraining Hessian iterations to move each vertex only perpendicular to the surface prevents vertices from moving off in strange directions that make convergence difficult. (See section 7.2.5)

7.2.4 Accuracy - an example

In theory any surface may be reproduced to machine precision accuracy provided sufficient computational resources are available. As an example consider the cube, in Figure 7.1 (a) with fixed volume $\frac{4\pi}{3}$. There are no other constraints on this cube so it should evolve into the structure which has the least surface energy for its topology - a sphere. This sphere has unit radius with total surface energy 4π.

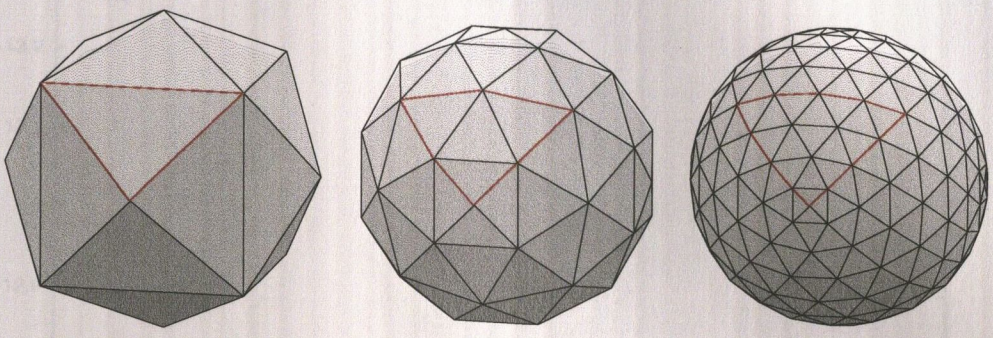

(a) R_0 (b) R_1 (c) R_2

Figure 7.2: The stages of minimisation of a sphere with radius 1: (a) shows the converged inputted plain sided structure, while (b) and (c) show the structure converged with one and two levels of refinement respectively. Note the flat red face in (a), refinement causes this parent facet to be replaced by four flat child facets in (b), and these child facets are further refined to replace themselves with four child facets of their own in (c).

The surface is minimised in each refinement level (R-level) until the mesh converges to some predefined value. In this case, until the difference in energy between two conjugate gradient steps is less than $1e-6$. The surface is then refined and the surface energy is minimised, Figure 7.2. Note how a flat facet in Figure 7.2 is replace by four facets after one level of refinement. Once minimised these four facets will not remain planar, but rather will move to a position which allows the volume constraints to be satisfied while providing the minimum surface energy at that R-level.

The surface energy of a sphere converges after several levels of refinement and minimisation, Figure 7.3. The number of facets, minimised surface energy, and percentage difference from analytical energy at each refinement level is shown in Table 7.2.4.

Figure 7.3 and Table 7.2.4 clearly show that the *Surface Evolver* is capable

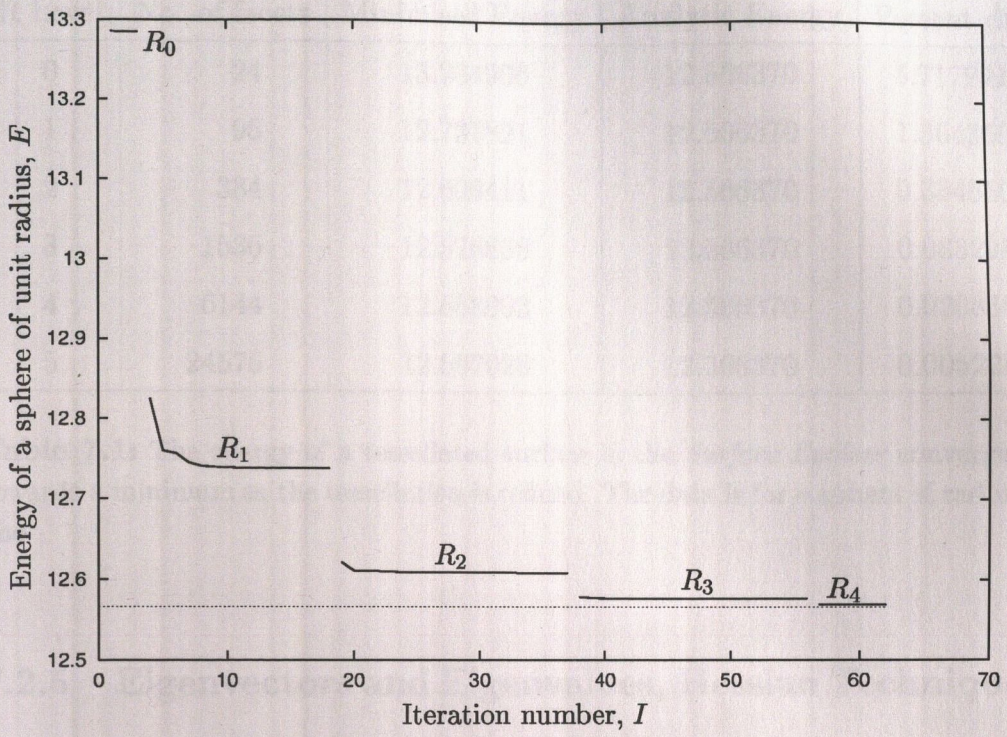

Figure 7.3: Minimisation of a sphere of unit radius. The total number of conjugate gradient steps required to minimised the surface energy at each level of refinement, R_0 - R_5, is shown. The dashed line shows the analytical solution.

of accurately calculating the energy of a sphere.

R Level	No. of facets	Minimised Energy	Analytic Energy	Percent diff
0	24	13.264906	12.566370	5.717921
1	96	12.737821	12.566370	1.364360
2	384	12.608411	12.566370	0.334550
3	1536	12.576838	12.566370	0.083298
4	6144	12.568993	12.566370	0.020868
5	24576	12.567028	12.566370	0.005228

Table 7.1: The energy of a tessellated surface in the *Surface Evolver* converges towards a minimum as the tessellation is refined. The data is for a sphere of radius one.

7.2.5 Eigenvectors and Eigenvalues, Hessian Techniques

The *Surface Evolver* parameterises a surface in terms of its vertex coordinates. Let $\tilde{\mathbf{x}}$ be an N-dimensional vector of all vertex coordinates for a particular triangulation. $\tilde{\mathbf{x}}$ is called the configuration vector and it inhabits an N dimensional configuration space. The total energy of the surface $E(\tilde{\mathbf{x}})$ is a scalar function on configuration space.

Constraints are scalar functions on configuration space which restrict $\tilde{\mathbf{x}}$ to lie on a particular level set. Global constraints determine a hyper-space by removing one degree of freedom from the configuration space. Level-set constraints are separate constraints and are applied only to the vertices they act on - removing one degree of freedom from them. The intersection of all constraint hyper-spaces is called the feasible set and is the set of all possible configurations satisfying all the constraints.

Consider applying a small perturbation $\tilde{\mathbf{y}}$ to a surface in a particular

configuration $\tilde{\mathbf{x}}$. The energy of the surface may be expanded giving

$$E(\tilde{\mathbf{x}}+\tilde{\mathbf{y}}) = E_0 + \tilde{\mathbf{g}}^T\tilde{\mathbf{y}} + \frac{1}{2}\tilde{\mathbf{y}}^T\mathbf{H}\tilde{\mathbf{y}} + \dots \tag{7.3}$$

Here E_0 is the original energy, $\tilde{\mathbf{g}}$ is the vector of first derivatives - the local gradient of the surface and the best linear approximation to the energy. $\mathbf{H}$ is a square matrix of second derivatives called the Hessian and is the best quadratic approximation of the local surface.

If the quadratic approximation to the surface is good, then we are close to a local minimum energy. An equilibrium point is found by solving for motion $\tilde{\mathbf{y}}$ that makes the energy gradient zero.

$$\nabla E = \tilde{\mathbf{g}}^T + \tilde{\mathbf{y}}^T\mathbf{H} \tag{7.4}$$

$$\tilde{\mathbf{g}} + \mathbf{H}\tilde{\mathbf{y}} = 0 \tag{7.5}$$

$$\tilde{\mathbf{y}} = -\mathbf{H}^{-1}\tilde{\mathbf{g}}. \tag{7.6}$$

The matrix $\mathbf{H}$ may be diagonalised by an orthogonal change of basis of configuration space. Each eigenvector represents a particular perturbation of the surface and its eigenvalue is related to the energy cost of such a perturbation. Negative eigenvalues indicate an unstable surface. By analysing the lowest eigenvalues of a stable configuration we may determine whether the surface is near an instability point.

For a more in-depth explanation consult the *Surface Evolver* tutorial on Hessian techniques, [54].

7.3 Energy calculations for wet structures

In this section we describe how the energy contribution of Plateau border films on the walls of a cylinder are calculated for the case of a wet bamboo structure and a wet 211 structure.

7.3.1 Wet bamboo structure

An Evolver simulation of a wet bamboo structure is shown in Figure 7.4. We wish to accurately calculate the volume and energy of the Plateau border which is shown as the volume enclosed within the green and magenta facets, (the magenta facets and the outlined white facets have been added in to aid visualisation and play no part in the computations). The yellow edges are at

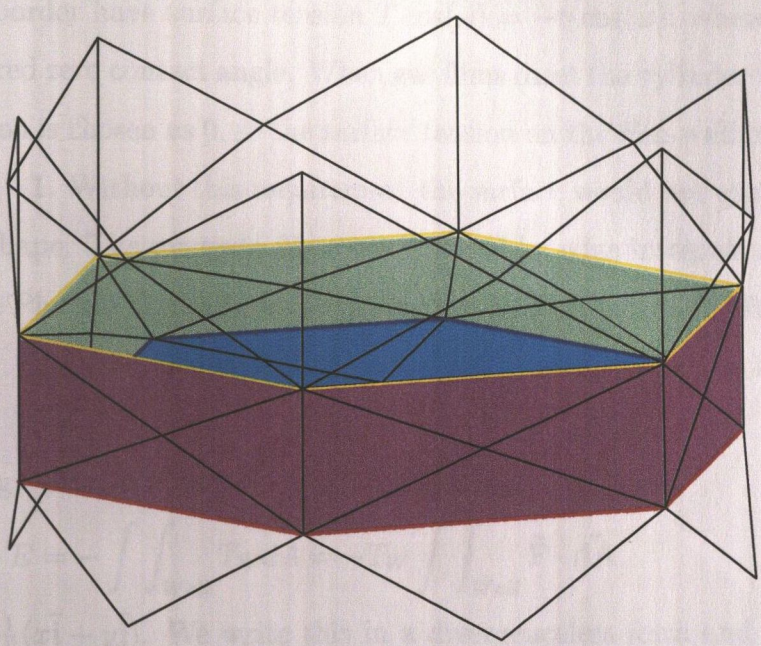

Figure 7.4: A *Surface Evolver* simulation showing a wet 110 foam. The blue facets are a gas-gas interface with $\gamma = 2$, the green facets are a gas-liquid interface with $\gamma = 1$, and the magenta facets are films on the surface wall where $\gamma = -1$. The magenta facets are replaced by edge integrals on the yellow and red edges.

$z = h_2$ and the red edges at $z = h_1$. The volume of a cylinder with radius R, height z, and axis in the $\tilde{\mathbf{k}}$ direction, may be calculated using the edge integrals of the previous section.

A boundary integral around the yellow edges at height h_2 finds the volume, V_2, of a cylinder with that height. We subtract from that the volume,

V_1, of a cylinder of height h_1 by taking a boundary integral around the red edges in Figure 7.4, giving $V_{2-1} = V_2 - V_1$. That still is not the volume of the Plateau border. The Evolver calculates the volume of gas in the cylinder between h_2 and h_1 and we subtract that from $V_{h_2-h_1}$ to get the Plateau border volume, V_{Pb}. Figure 7.5 shows the surface used in the computations. Further details are provided in Appendix A.2.

The energy of the Plateau border films is found by assuming the walls around the border have surface tension $T\cos(\omega) = -\gamma\cos(\omega)$, where $\omega = 0$ for the required zero contact angle. When gas films meet the cylinder wall the surface tension is chosen as 0, so the surface tension on the film-wall interface must be $\gamma = -1$. Without this requirement the surface would not evolve into the correct shape. The magenta films are replaced by edge integrals and the energy of the Plateau border films on the surface walls is subtracted from the total energy. The energy calculated is then just the energy of the internal films.

The energy contribution due to the contact angle, [96], is

$$E = -\int\int_{Wall} T_W dA = -T_W \int\int_{Wall} \tilde{\mathbf{F}} \cdot \mathbf{d\tilde{A}}.$$

Where $\tilde{\mathbf{F}} = \frac{1}{R}(x\tilde{\mathbf{i}} + y\tilde{\mathbf{j}})$. We write this in a divergenceless form and solve it as an integral over the boundary of the wall using Stokes theorem,

$$\tilde{\mathbf{F}} = -T\left(\frac{R^2}{x^2+y^2}\right)\frac{1}{R}(x\tilde{\mathbf{i}} + y\tilde{\mathbf{j}}) = -T\frac{R}{(x^2+y^2)}(x\tilde{\mathbf{i}} + y\tilde{\mathbf{j}})$$

Solving $\nabla \times \tilde{\omega} = \tilde{\mathbf{F}}$ gives the vector field

$$\tilde{\omega} = -T_W \frac{Rz}{x^2+y^2}\left(-y\tilde{\mathbf{i}} + x\tilde{\mathbf{j}}\right)$$

This vector field may only be applied to edges with a constant $\tilde{\mathbf{k}}$ component. This is sufficient for calculations in this case, as the Plateau border has only radial components, but would be of no use in calculations when a Plateau border forms with components in the $\tilde{\mathbf{k}}$ direction.

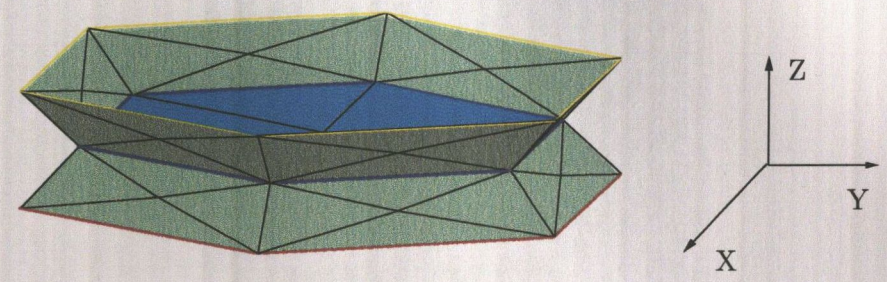

Figure 7.5: A *Surface Evolver* simulation showing only the facets involved in calculations. The total energy calculated is for interior films minus the energy due to the Plateau border interface with the cylinder wall. The total energy contribution due to the films of the gas bubble and the border is calculated by simply adding the energy of the surface films for the dry foam case. $\Phi_l \approx 0.006$

7.3.2 Wet 211 structure

An *Evolver* simulation of a wet 211 is shown in Figure 7.6. We need to calculate the volume, area and energy of this structure - and proceed in a manner similar to the previous section. The divergenceless form of the vector field $\tilde{\mathbf{F}}$ is

$$\tilde{\mathbf{F}} = \frac{R^2}{2(x^2+y^2)} x\tilde{\mathbf{i}} + y\tilde{\mathbf{j}} \qquad \text{For volume} \tag{7.7}$$

$$\tilde{\mathbf{F_W}} = -T\frac{R}{(x^2+y^2)}(x\tilde{\mathbf{i}} + y\tilde{\mathbf{j}}) \qquad \text{For energy} \tag{7.8}$$

However, when we solve these for $\tilde{\omega}$, we need to pick a vector potential which can be applied to edges with components in the $\tilde{\mathbf{i}}$, $\tilde{\mathbf{j}}$ and $\tilde{\mathbf{k}}$ directions. The problem with solving for such a vector field is that it is not always valid everywhere, and we must be very careful when implementing it.

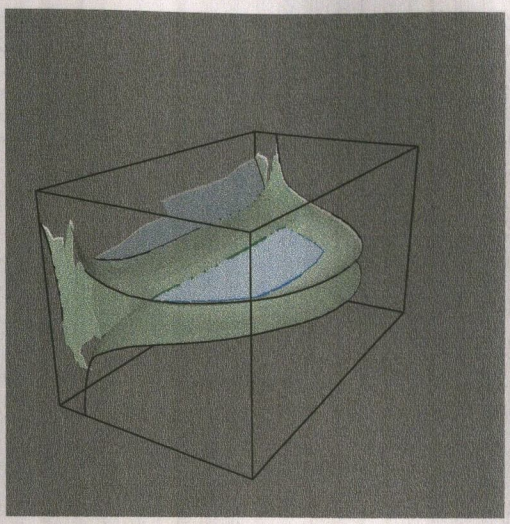

Figure 7.6: A wet 211 crystalline structures where $\Phi_l = 3\%$. The green films show liquid-film interfaces where $\gamma = 1$, the blue films show film-film interfaces where $\gamma = 2$. The energy and area contribution due to faces on the surface of the cylinder is calculated using surface and line integrals on the edges on the cylinder surface. The 211 structure repeats periodically through a translation of height $\frac{h}{2}$ in the $z - direction$ and a rotation of 180°.

Solving for $\tilde{\omega}$ we get

$$\tilde{\omega}_V = \frac{R^2}{2(x^2+y^2)} \arctan\left(\frac{(x+y)}{(x-y)} - \frac{\pi}{4}\right)\tilde{\mathbf{k}}$$

used in volume calculations and

$$\tilde{\omega}_W = \frac{R^2}{(x^2+y^2)} \arctan\left(\frac{(x+y)}{(x-y)} - \frac{\pi}{4}\right)\tilde{\mathbf{k}}$$

used in energy calculations.

7.4 Hessian techniques - Liquid drops

In this section we present details of calculations used to find instability points for two liquid drops in contact. Included is a numerical feasibility study,

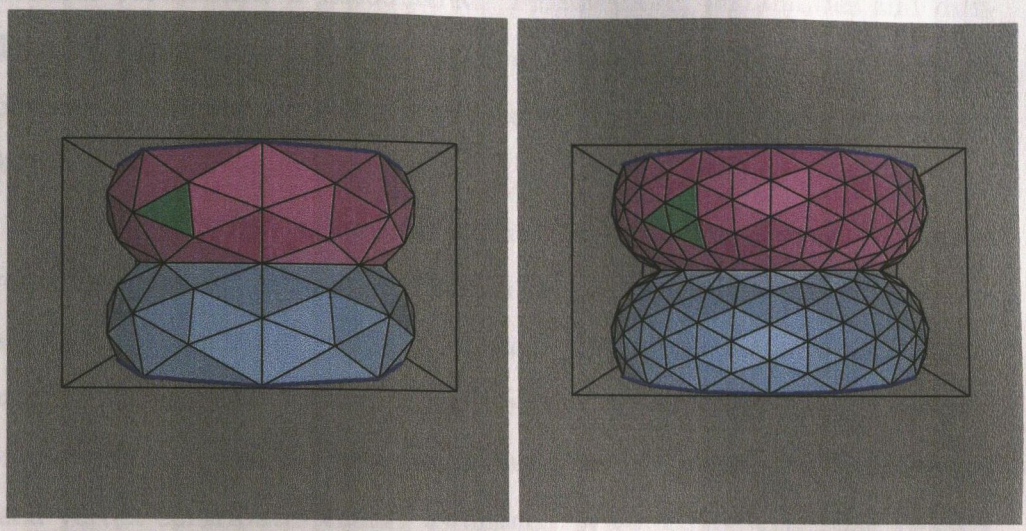

Figure 7.7: *Surface Evolver* simulations of two liquid drops in contact. (Left) a minimised surface at one level of refinement, note the single flat green facet. (Right) a minimised surface at two levels of refinement. The single green parent facet has been replaced by four flat child facets.

which assesses the accuracy of using the *Surface Evolver* for this type of calculation.

Consider a surface $\mathcal{S}$, Figure 7.7, with energy $E_{\mathcal{S}}$ approximated by a particular triangulation $\tilde{\mathbf{x}}$. The total energy, $E(\tilde{\mathbf{x}})$, of this surface is a function of $\tilde{\mathbf{x}}$ - the N-dimensional vector of all its vertex coordinates. The best approximation to this surface is found by minimising the energy of this triangulation - using techniques described in section 7.2.5. A closer approximation to the energy is found by increasing the number of vertices, and hence triangles, describing $\mathcal{S}$ in a process known as refinement.

In theory, $\mathcal{S}$ may be approximated by an infinite number of vertices. In practice, refinement is limited by computational resources. Nevertheless, a numerical refinement study is required to ensure $\mathcal{S}$ is triangulated by a sufficient number of vertices. In general this is done by comparing the minimised energies of different refinement levels until a convergence in energy between

successive refinements is encountered. Furthermore, instabilities add difficulty to a refinement study. The point of instability is likely to depend on a particular triangulations ability to accurately describe a surface - as Table 7.4 shows.

The surface energy is brought close to a minimum at each refinement level using gradient descent and Hessian techniques are then used to ensure a stable minimum energy point is reached. The liquid drops are fixed onto two disks via a number of constrained vertices. These vertices are prevented from moving, and hence contribute no energy to the system or to the Hessian. (Each vertex contributes energy as defined by equation 7.1). The Hessian matrix must be positive definite, however the sideways movement of vertices often makes this difficult to achieve. Allowing vertices to move only perpendicular to a surface while calculating the Hessian can ensure a positive definite matrix is formed.

Refinement Level	Vertices		Facets	d_{crit}	Energy	Energy difference, %
	Total	Constrained				
1	77	10	144	1.032	8.627	-
2	297	18	576	1.021	8.389	2.83
3	1169	34	2304	1.019	8.327	0.74
4	4641	66	9216	1.018	8.313	0.17
5	18367	130	36864	1.018	8.304	0.10

Table 7.2: The energy and instability point of the surface in Figure 7.7 depends on the number of surface facets. Refinement quadruples the number of triangles representing the surface - and hence provides a better approximation to the true surface energy. Refinement and minimisation must continue until the surface energy converges between two refinement levels.

The total surface energy as a function of iteration steps is shown in Fig-

ure 7.8. Refinement quadruples the number of facets while still allowing the structure to obey Euler's rules. The energy drop due to convergence at a refinement level is small in comparison to the energy drop between refinement levels. However, each refinement level also contains structure as Figure 7.9 shows.

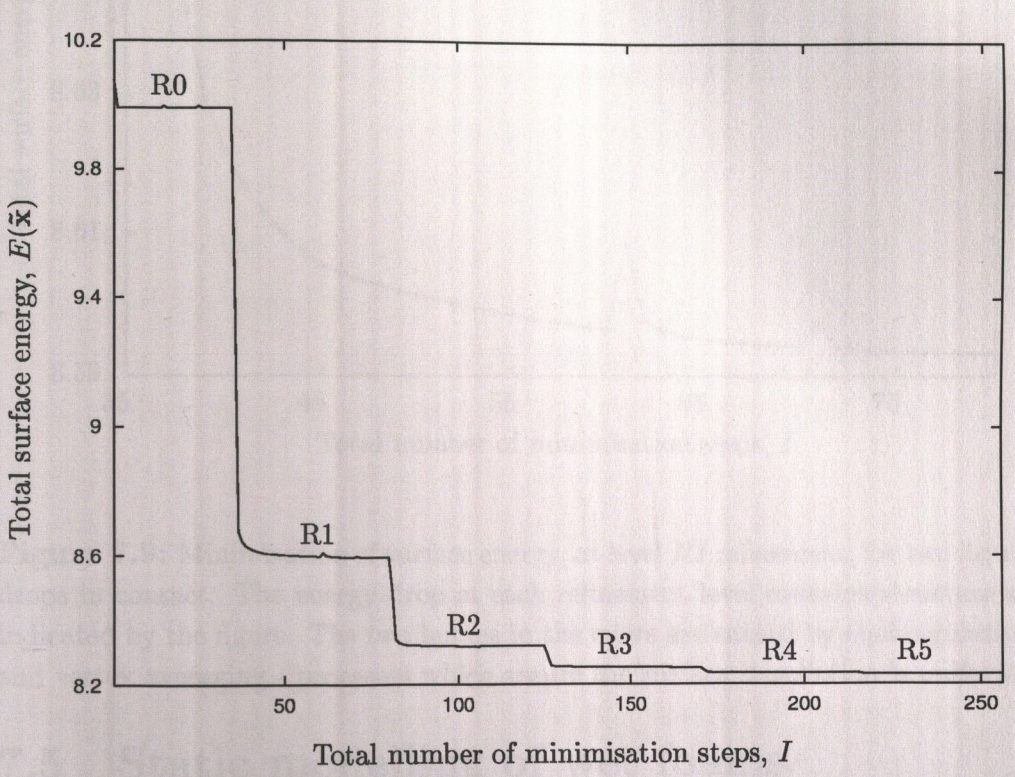

Figure 7.8: Surface energy minimisation of two liquid drops in contact. The total number of conjugate gradient steps required to minimise the surface at each refinement level, *R0* - *R5*, is shown. The energy difference between successive refinement levels clearly converges to zero.

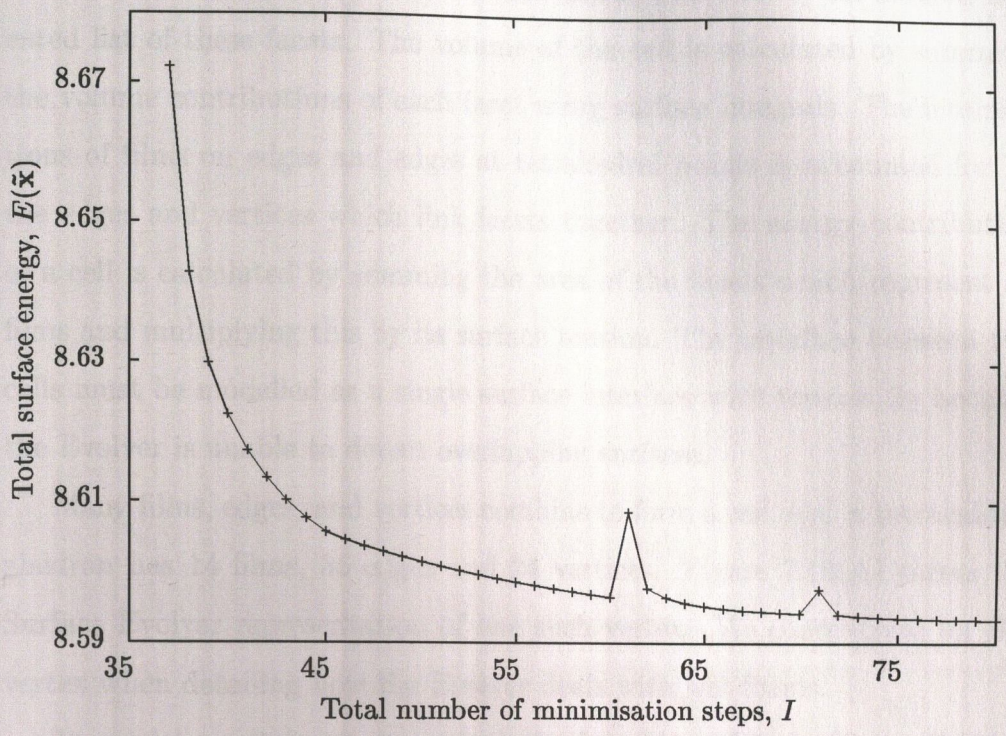

Figure 7.9: Minimisation of surface energy, at level *R1* refinement, for two liquid drops in contact. The energy drop at each refinement level contains structure as indicated by the figure. The two humps in the curve are caused by equiangulation and vertex averaging - processes which ensure the surface tessellation is uniform.

7.5 Static modelling of wet foams

In this section we detail how the Evolver representation of an idealised dry foam may be adapted to model wet foams. Dry foams, $\Phi_l \to 0$, must obey Plateau's rules and Laplace's law, section 1.2. Each polyhedral cell contains many curved films which meet three at a time on edges. These edges meet four at a time at tetrahedral points. The films surround the gas inside the cell, which is treated as incompressible. The energy of the cells is normally just a surface tension contribution, which is simply the total surface area of its films times its surface tension γ.

The Evolver represents films by flat facets, and cells by an ordered oriented list of these facets. The volume of the cell is calculated by summing the volume contributions of each facet using surface integrals. The intersections of films on edges and edges at tetrahedral points is accounted for by the edges and vertices which link facets together. The energy contribution of a cell is calculated by summing the area of the facets which represent its films and multiplying this by its surface tension. The interface between two cells must be modelled as a single surface interface with tension 2γ because the Evolver is unable to detect overlapping surfaces.

Many films, edges, and vertices combine to form a cell, e.g. a tetrakaidecahedron has 14 films, 36 edges and 24 vertices. Figure 7.10(A) shows the Surface Evolver representation of one such vertex. We concentrate on this vertex when detailing how the Evolver deals with wet foams.

To model a wet foam, we replace the four blue edges in Figure 7.10(A) with hollow tubes of length L and triangular cross section, where the triangles are equilateral with side length δ. The tetrahedral vertex is replaced by an hollow octahedron with four open sides each attached to a hollow tube, Figure 7.10(B).

The facets forming the hollow tubes are linked together to create an additional body, which represents the liquid channel and junction around this part of the cells in a wet foam. The volume of channel and junction, Φ_l, is calculated by its list of facets. The liquid channel forms a liquid-gas interface with the cell it surrounds, and has surface tension γ. We refer to it as a tetrahedral junction, or tetrahedral vertex.

The shape and volume of a tetrahedral junction are calculated by considering a junction in isolation. In Figure 7.10 the four gas bubbles which meet at the junction have been removed leaving only their films required to

produce the correct geometry.

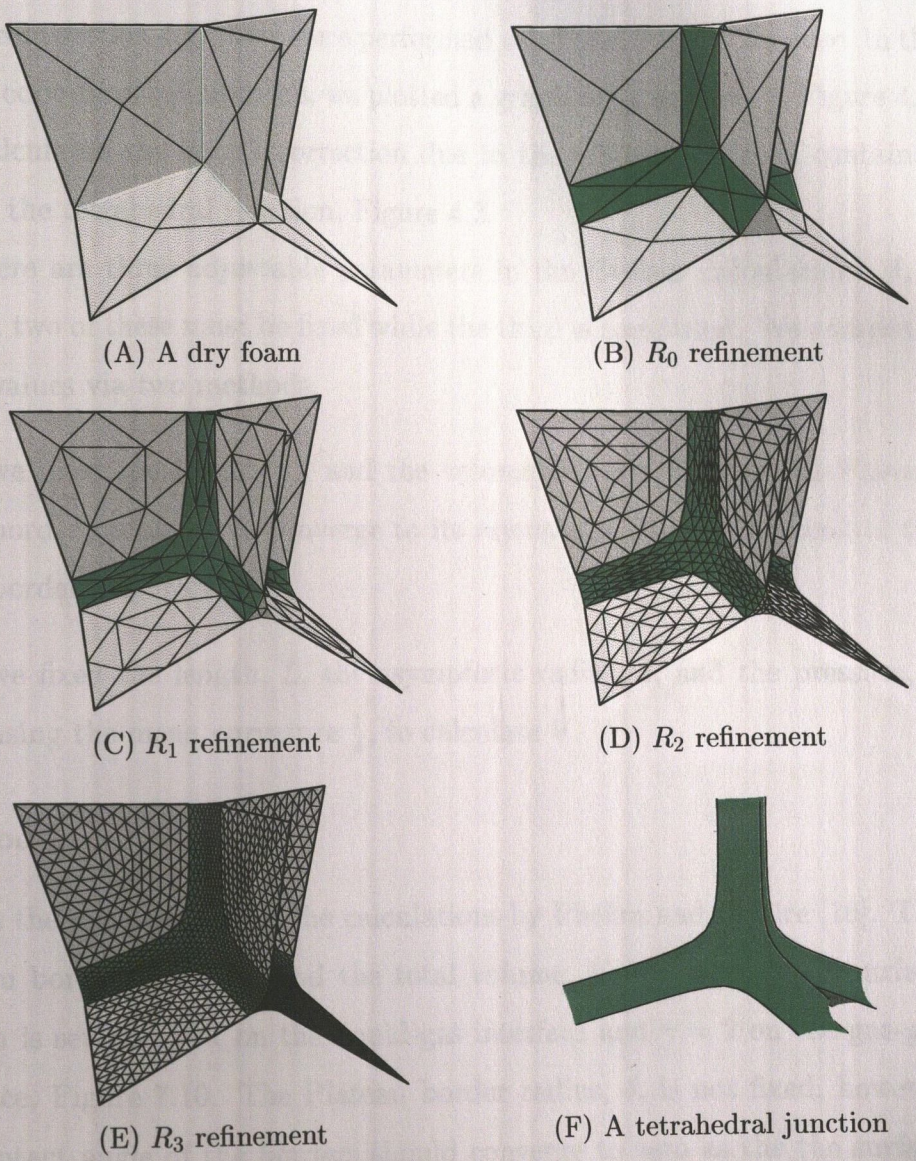

(A) A dry foam

(B) R_0 refinement

(C) R_1 refinement

(D) R_2 refinement

(E) R_3 refinement

(F) A tetrahedral junction

Figure 7.10: *Surface Evolver* simulations of a single tetrahedral junction. A foam in the dry limit ($\Phi_l \to 0$) obeys Plateau's rules and Laplace's law (A). For wet foam simulations, the lines are replaced by straight line tubes with triangular cross section and the point of intersection is replaced by an octahedron, (B). The structure is successively refined and minimised using conjugate gradient and Hessian techniques, (C), (D) and (E). The final minimised tetrahedral junction has its surrounding films removed, (F). $\Phi_l \approx 0.006$.

7.5.1 Vertex correction calculations

In this section we present the numerical details of vertex correction calculations from section 4.3, these were performed using the *Surface Evolver*. In the vertex correction calculations, we plotted a graph of $\frac{V}{\delta^3}$ against $\frac{L}{\delta}$, Figure 4.4, and calculated the length correction due to the volume of liquid contained within the tetrahedral junction, Figure 4.3.

There are three adjustable parameters in the Evolver calculations, δ, L and V, two of these must be fixed while the third is computed. We computed these values via two methods,

(I) we fixed the length, L, and the volume, V, and allowed the Plateau border radius, δ, to converge to its asymptotic value at the end of the border, Figure 4.3,

(II) we fixed the length, L, the asymptotic radius, δ, and the pressure, p using the mean curvature $\frac{1}{\delta}$, to calculate V.

Method I

This is the method used in the calculations by Phelan and Weaire [16]. The Plateau border length L, and the total volume, V, are fixed. The surface tension is set as $\gamma = 1$ on the liquid-gas interface and $\gamma = 2$ on the gas-gas interface, Figure 7.10. The Plateau border radius, δ, is not fixed, however the contact angle of the borders should converge to zero as the the surface tension jumps from $\gamma = 1$ to $\gamma = 2$ where the borders meet the gas films. Therefore δ should also converge to its unknown asymptotic value as the surface is successively refined and minimised. $\frac{L}{\delta}$ and $\frac{V}{\delta^3}$ may be calculated, and a length correction of 0.75δ is found using this method.

Unfortunately, there are problems with this method. The Plateau border

Refinement level	Method I, $C = 0.75\delta$, $\frac{\delta_n}{\delta}$	Method I, $C = 0.78\delta$, $\frac{\delta_n}{\delta}$	Method II, $C = 0.78\delta$, $\frac{\delta_n}{\delta}$
0	1.032	1.034	1.638
1	1.029	1.033	1.238
2	0.980	0.984	1.063
3	0.966	0.969	1.013
4	0.963	0.966	1.002

Table 7.3: A comparison between the computed radius, δ_n, and its asymptotic value at the end of a Plateau border arm, δ, is shown. Two methods are considered. If a method works correctly, $\frac{\delta_n}{\delta} \approx 1.0$ at high refinement levels. In Method I, $C = 0.75\delta$ or $C = 0.78\delta$, the radius is clearly not converging to its asymptotic value. In Method II, $C = 0.78\delta$, the radius converges to within 0.2% of the correct value after four levels of refinement and minimisation. (C is the vertex correction term.)

radius, δ, never actually reaches its asymptotic value, i.e. the contact angle between the Plateau border and the cell walls does not converge to zero. The volume of the four borders and vertex is written as

$$V_{Vertex} = 4c_g\delta^2(L + 0.75\delta) \tag{7.9}$$

using a length correction of 0.75δ per arm. We perform an Evolver calculation where L, δ and V_{Vertex} are set. L and V_{Vertex} are again fixed. If this method works correctly the asymptotic Plateau border radius should converge to its set value of δ following refinement and minimisation. This is not the case, as shown in Table 7.3.

Method II

In this method, the Plateau border length and radius are fixed. The surface tension is again set at $\gamma = 1$ on the liquid-gas interface and $\gamma = 2$ on the gas-gas interface, Figure 7.10. The volume is not fixed, and will grow uncontrollably unless it is somehow constrained. The trick (similar to one used by Brakke, [52]) is to set a constant pressure, p_c, outside the Plateau borders - we have assumed that the tetrahedral junction is surrounded by four bubbles with constant pressure which have been removed to simplify the calculations. The constant pressure is related to γ and δ by Laplace's Law,

$$p_c = \frac{\gamma}{\delta}$$

This provides an appropriate bound on the volume.

We calculated V, and hence $\frac{V}{\delta^3}$ and $\frac{L}{\delta}$ using this method. The results are plotted in Figure 4.4, producing a vertex correction of 0.78δ for each arm.

This method is successful in calculating the asymptotic Plateau border radius, and hence zero contact angle required, as Table 7.3 shows.

7.6 Fluent - Modelling liquid flow in foams

Fluent [24] is a computational fluid mechanics package used for solving complex flow problems in three dimensions. It is accompanied by Gambit [63], a preprocessor used for modelling geometrical shapes and generating internal meshes. Objects with different surface geometries may be created using Gambit, or may be fed into the program provided the method used to represent their geometry is supported. Various boundary conditions may be set on the surface geometry at this point. For example, to model the flow down a circular duct we would define the cylindrical surface of the duct as a *wall*,

and define the ducts at each ends as a pressure inlet or outlet. The geometry enclosed with the surface mesh is then refined to form a three dimensional volume mesh - or grid.

The volume grid is loaded into Fluent and all its boundary conditions are set. For example, these would include defining a no-slip boundary condition on the surface wall and setting the physical properties of the fluid flowing through the duct. Fluent may be used to model amongst others;

- flow in two and three dimensional geometries
- compressible or incompressible fluid flows
- Newtonian or non-Newtonian flows
- laminar, turbulent, or inviscid flow

Unstructured meshes are used in Fluent - they allow more complex geometries to be modelled and are more adaptable to modelling sharp localised surface curvatures. In general, initial meshes produced by Gambit may be adapted to produce a better representation of the surface geometry. Fluent solves the Navier-Stokes equations on the fluid flowing within the surface boundaries. Fluent uses one of two numerical methods to solve the governing continuity and momentum equations. In its segregated solver method, the governing nonlinear equations of the system are solved sequentially (segregated). The momentum equations are all solved, followed by the continuity equations. A check for convergence is made at the end of each iteration step. The solution is reached once some predefined convergence criteria is reached, Figure 7.11.

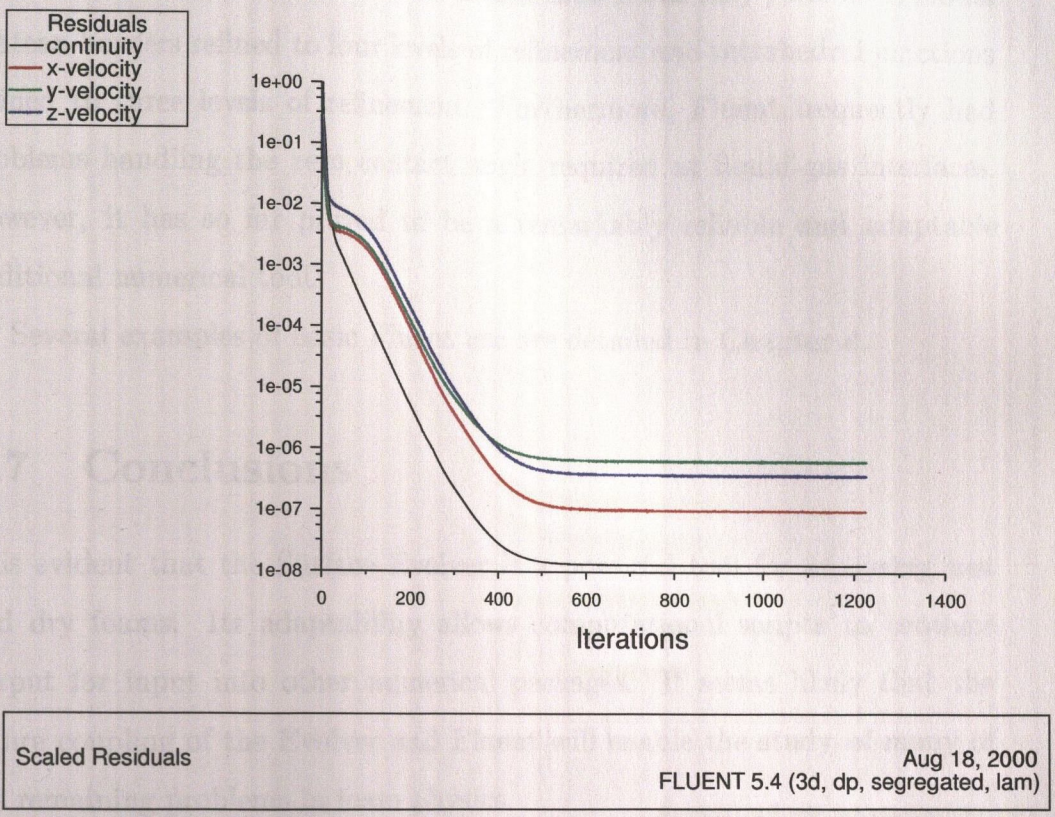

Figure 7.11: A typical residual graph produced by Fluent. The residuals of continuity and velocity are calculated after each iteration step. When the residuals converge the governing momentum and continuity equations are solved.

7.6.1 The Evolver and Fluent

The surface geometry produced by the Evolver is not in a format recognised by Gambit, so we developed a program to convert from one geometrical representation to another compatible one. Vertices are converted into three dimensional vertex co-ordinates, oriented edges are converted into disoriented edges, and oriented faces are converted into edges with no orientation. These faces are stitched together to form a volume. The resulting geometry forms a *journal file*, and is read into Gambit and meshed.

Unfortunately, Gambit seems unable to handle Evolver surface meshes with more than 7,000 vertices. This meant that it was only possible to model Plateau borders refined to four levels of refinement and tetrahedral junctions refined to three levels of refinement. Furthermore, Fluent frequently had problems handling the zero contact angle required at liquid-gas interfaces. However, it has so far proved to be a remarkably reliable and adaptable additional numerical tool.

Several examples of basic Fluent use are detailed in Chapter 4.

7.7 Conclusions

It is evident that the Surface Evolver is a powerful tool for analysing wet and dry foams. Its adaptability allows computational scripts to produce output for input into other numerical packages. It seems likely that the future coupling of the Evolver and Fluent will enable the study of many of the remaining problems in foam physics.

7.8 Acknowledgements

Thanks are due to Ken Brakke for providing the wet 211 Evolver datafile and some of the complex integrals used by the Surface Evolver. The Evolver implementation details are based largely on the software manual, [13]. Thanks are also due to Robert Phelan and Simon Cox for useful discussions.

Appendix A

Calculation details

A.1 A derivation of the Laplace-Young Law

Soap bubbles in equilibrium (or quasi-equilibrium) are stable due to a delicate balance of pressure, p, and surface tension, γ. Consider a spherical bubble of radius R, and volume, V. It's energy depends purely on its surface area, E_A, and surface tension (for two membranes). We evaluate its stability by applying a small perturbation, δR[1] to its radius. The new bubble volume and surface area may be approximated by

$$V_{R-\delta R} \approx 4\pi \left(R^3 - R^2\delta R\right) \quad \Longrightarrow \quad V_{\delta R} = 4\pi R^2 \delta R$$
$$A_{R-\delta R} \approx 8\pi \left(R^2 - R\delta R\right) \quad \Longrightarrow \quad A_{\delta R} = 8\pi R \delta R$$

and the work done is simply

$$\delta W_{\delta R} = 2\gamma 8\pi R\delta R. \tag{A.1}$$

The reduction of volume causes the pressure of gas inside the bubble to

[1] δ indicates a small change, and not a Plateau border radius, the clash in nomenclature is unfortunate.

increase, the work required to cause this increase is defined as

$$\delta W_{\delta R} = 4\pi R^2 \delta R \Delta p. \tag{A.2}$$

If the bubble reaches equilibrium, then equation A.1 equals equation A.2 giving,

$$\Delta p = \frac{4\gamma}{R} \quad \text{for a foam in three spatial dimensions.} \tag{A.3}$$

A.2 Volume calculations using the *Surface Evolver*

Suppose we wish to calculate the volume of a body $\mathcal{B}$. The volume may be defined as the triple integral

$$V = \int\int\int_{\mathcal{B}} dV, \tag{A.4}$$

where dV is an element of volume. The *Surface Evolver* is unable to calculate triple integrals, but we may write equation A.4 in terms of surface integrals using the divergence theorem, see Bourne and Kendall [97],

$$\int\int\int_{\mathcal{B}} \nabla \cdot \tilde{\mathbf{F}} dV = \int\int_{\partial\mathcal{B}} \tilde{\mathbf{F}} \cdot \tilde{\mathbf{n}} dA \tag{A.5}$$

where $\nabla \cdot \tilde{\mathbf{F}} = 1$. For a cylinder of radius R, oriented in the z direction, the obvious choice of vectorfield $\tilde{\mathbf{F}}$ is $\tilde{\mathbf{F}} = z\tilde{\mathbf{k}}$, giving

$$V = \int\int_{\partial B} z\tilde{\mathbf{k}} \cdot \tilde{\mathbf{n}} dA \tag{A.6}$$

We do not need to integrate over all of $\partial\mathcal{B}$. Suppose a surface $\mathcal{S} \subseteq \partial\mathcal{B}$ is part of a level set constraint $F(x, y, z) = 0$. Then the surface integral may be written as a line integral using Stokes Theorem, see Boas [62],

$$\int\int_{S} z\tilde{\mathbf{k}} \cdot \tilde{\mathbf{n}} dA = \int_{\partial S} \tilde{\omega} \cdot \tilde{\mathbf{dl}} \tag{A.7}$$

where $\nabla \times \tilde{\omega} = \tilde{\mathbf{F}} = z\tilde{\mathbf{k}}$. Now $\nabla \cdot (\nabla \times \tilde{\omega}) = 0$, but $\nabla z\tilde{\mathbf{k}} \neq 0$, so we need an equivalent form of $z\tilde{\mathbf{k}}$ which is divergenceless on $\mathcal{S}$. Clearly this can't be done for this case.

The trick is to choose a vector field, $\tilde{\mathbf{F}} = \frac{1}{3}\left(x\tilde{\mathbf{i}} + y\tilde{\mathbf{j}} + z\tilde{\mathbf{k}}\right)$, and drop the $\tilde{\mathbf{k}}$ component, giving a purely radial vectorfield. (This leads to implementation problems. These vectorfields may be applied to films with radial content only). Now $\tilde{\mathbf{F}} = \frac{1}{2}\left(x\tilde{\mathbf{i}} + y\tilde{\mathbf{j}}\right)$, is not in divergenceless form either, but we may rewrite it as

$$\tilde{\mathbf{F}} = \frac{R^2}{2(x^2+y^2)} x\tilde{\mathbf{i}} + y\tilde{\mathbf{j}}, \tag{A.8}$$

giving

$$\nabla \cdot \tilde{\mathbf{F}} = \left(\frac{(x^2+y^2)-2x^2}{(x^2+y^2)^2} + 0 + \frac{(x^2+y^2)-2y^2}{(x^2+y^2)^2}\right) = 0 \tag{A.9}$$

Solving $\nabla \times \tilde{\omega} = \tilde{\mathbf{F}}$ gives the vector potential

$$\tilde{\omega} = \frac{R^2 z}{2(x^2+y^2)}\left(-y\tilde{\mathbf{i}} + x\tilde{\mathbf{j}}\right) \tag{A.10}$$

$\tilde{\omega}$ is applied to all edges surrounding the volume, and the sum of these line integrals calculates the required volume.

A.3 Surface energy of cylindrical crystalline structures

The energy of a cylindrical crystalline foams in the dry limit, $\Phi_l \to 0$, depends only on the variation of bubble to tube radius, $\lambda = \frac{R}{r}$. Each bubble has an energy term associated with its films on the surface of the cylinder, E_S^{PB}, and a term associated with its interior films, E_F^{PB}. If E_i^{PB} is the energy of the

i^{th} bubble in a tube of fixed length L, and N is the total number of bubbles in the tube, the total energy may be written as

$$E_T(\lambda) = \sum_i E_i^{PB}.$$

Each bubble will have a volume

$$V^{PB} = \pi R^2 \frac{L}{N} = \frac{4}{3}\pi r^3,$$

and the energy per bubble E_T^{PB} may be written as

$$\begin{aligned}
E_T^{PB} &= \frac{E_F(\lambda) + E_S(\lambda)}{N} \\
&= E_F^{PB}(\lambda) + \frac{E_S(\lambda)}{N} \\
&= E_F^{PB}(\lambda) + \frac{2\pi RL}{N} V^{PB} \frac{N}{\pi R^2 L} \\
&= E_F^{PB}(\lambda) + \frac{2V^{PB}}{R} \\
&= E_F^{PB}(\lambda) + \frac{8\pi r^3}{3R} \\
&= E_F^{PB}(\lambda) + \frac{8\pi r^2}{3\lambda} \\
&= E_F^{PB}(\lambda) + \frac{8\pi}{3}\left(\frac{3}{4\pi}\right)^{2/3} \lambda^{-1} \qquad \text{when } V_{PB} = 1.0 \\
&= E_F^{PB}(\lambda) + 3.224\lambda^{-1}
\end{aligned}$$

Therefore, the energy of a cylindrical crystalline foam structure may be found by numerical calculations of E_F^{PB}, greatly saving computational resources.

A.4 The foam drainage equation

This section deals with the derivation and non-dimensionalisation of the *foam drainage equation*, [9, 88].

Consider a Plateau border of cross sectional area A oriented in the vertical z direction, surrounded by three gas bubbles at equal pressures p_g. The Laplace-Young Law, section 1.2.1, states

$$p_g - p_l = \frac{\gamma}{R} \tag{A.11}$$

where p_l is the pressure in Plateau border and R is the asymptotic radius of curvature of the surface.

The area of a P.B. is

$$A_{Pb} = (\sqrt{(3)} - \pi)R^2 \tag{A.12}$$

$$= C^2R^2 \tag{A.13}$$

The forces acting on the liquid in the Plateau border are

Gravity: ρg

Capillarity: $\frac{-\partial p_l}{\partial z}$

Dissipation: $-\frac{\eta u}{A}$

Balancing these forces yields:

$$\rho g - \frac{\partial p_l}{\partial z} - \frac{\eta u}{A} = 0 \tag{A.14}$$

$$u = \frac{1}{\eta}\left(A\rho g - A\frac{\partial p_l}{\partial z}\right) \tag{A.15}$$

$$\frac{\partial p_l}{\partial z} = \frac{\partial p_g}{\partial z} + \left(\frac{C\gamma}{2}A^{-\frac{3}{2}}\frac{\partial A}{\partial z}\right) \tag{A.16}$$

$$\Longrightarrow u = \frac{1}{\eta}\left(\rho g A - \frac{C\gamma}{2A^{\frac{1}{2}}}\frac{\partial A}{\partial z}\right) \tag{A.17}$$

The continuity equation, section 4.4.1,

$$\frac{\partial(A)}{\partial t} + \frac{\partial(Au)}{\partial z} = 0 \tag{A.18}$$

is applied to conserve the total amount of liquid in the system. Inserting equation A.17 into equation A.18 gives

$$\frac{\partial A}{\partial t} + \frac{\partial}{\partial z}\left(\frac{1}{\eta}\left(\rho g A^2 - \frac{C\gamma A^{\frac{1}{2}}}{2}\frac{\partial A}{\partial z}\right)\right) = 0 \tag{A.19}$$

or

$$\frac{\partial A}{\partial t} + \frac{\partial Q_l}{\partial z} = 0 \quad \text{where } Q_l = Au \tag{A.20}$$

A.4.1 A note on η

The quantity, η, is defined by the dissipation term $-\frac{\eta u}{A}$ and is equivalent to $\eta = \chi\eta_l$ used in Chapter 4. For a Plateau border, we found $\chi \approx 50$, where χ simply depends on the geometry of the cross-sectional duct the fluid is flowing through.

There is a further correction to make. We have assumed so far that all Plateau borders are oriented in the vertical direction, but this of course in not the case in a three dimensional foam sample. The borders will be tilted at some general angle, θ, to the vertical, and further, the fluid flowing down the borders will be subjected to a gravitational force also dependent on θ. The borders are then oriented with some direction $z_\theta = z\cos\theta$, and the force is written as $F_\theta = \rho g\cos\theta$, giving

$$\frac{\partial A}{\partial t} + \frac{\partial}{\partial z}\left(\frac{\cos^2\theta}{\eta}\left(\rho g A^2 - \frac{C\gamma A^{\frac{1}{2}}}{2}\frac{\partial A}{\partial z}\right)\right) = 0 \tag{A.21}$$

We then take the average of $\cos^2\theta$,

$$< \cos^2\theta >= \frac{\int_0^\pi \cos^2\theta \sin\theta d\theta}{\int_0^\pi \sin\theta d\theta} = \frac{1}{3}$$

to obtain the network average, and assume that the dimensionless drainage equation can be applied for a three dimensional network of Plateau borders provided we write the viscosity as

$$\eta^* = 3\eta \approx 150$$

The network average velocity and drainage equation are then written as

$$u = \frac{1}{\eta^*}\left(\rho g A - \frac{C\gamma}{2A^{\frac{1}{2}}}\frac{\partial A}{\partial z}\right) \tag{A.22}$$

$$\frac{\partial A}{\partial t} + \frac{\partial}{\partial z}\left(\frac{1}{\eta^*}\left(\rho g A^2 - \frac{C\gamma A^{\frac{1}{2}}}{2}\frac{\partial A}{\partial z}\right)\right) = 0 \tag{A.23}$$

A.4.2 A note on N

The drainage equation must be adapted to allow for a variation in N - the number of Plateau borders crossing a unit area of foam. We rewrite the continuity equation as

$$\frac{\partial(NA)}{\partial t} + \frac{\partial(NAu)}{\partial z} = 0 \tag{A.24}$$

follow derivation this leads to the foam drainage equation,

$$N\frac{\partial A}{\partial t} + \frac{\partial}{\partial z}\left(\frac{N}{\eta^*}\left(\rho g A^2 - \frac{C\gamma A^{\frac{1}{2}}}{2}\frac{\partial A}{\partial z}\right)\right) = 0 \tag{A.25}$$

A.4.3 Two dimensions

In two dimensions, [88, 19, 98], the continuity equation for liquid flowing through N Plateau borders of cross sectional area A_{Pb}, with downward flow velocity u in the z-direction and horizontal flow velocity v in the x-direction, becomes

$$\frac{\partial(NA)}{\partial t} + \frac{\partial(NAu)}{\partial z} + \frac{\partial(NAu)}{\partial x} = 0 \tag{A.26}$$

The balance of forces remains unchanged in the z-direction giving,

$$u = \frac{1}{\eta^*}\left(\rho g A - \frac{C\gamma}{2A^{\frac{1}{2}}}\frac{\partial A}{\partial z}\right) \tag{A.27}$$

from the one dimensional case. In the X direction, the forces acting on the liquid in the Plateau border are

Capillarity: $\frac{-\partial p_l}{\partial x}$

Dispersion: $-\frac{\eta v}{A}$

This gives the velocity in the X direction

$$v = \frac{A}{\eta^*}\frac{\partial}{\partial x}\left(\frac{C\gamma}{\sqrt{A}}\right) = \frac{C\gamma}{2\eta^* A^{\frac{1}{2}}}\frac{\partial A}{\partial x}$$

Substituting u and v in equation A.26 gives the 2d foam drainage equation,

$$N\frac{\partial A}{\partial t} = \frac{\partial}{\partial z}\left(\frac{N}{\eta^*}\left(\rho g A^2 - \frac{C\gamma A^{\frac{1}{2}}}{2}\frac{\partial A}{\partial z}\right)\right) + \frac{\partial}{\partial x}\left(\frac{NC\gamma A^{\frac{1}{2}}}{2\eta^*}\frac{\partial A}{\partial x}\right) = 0 \tag{A.28}$$

or

$$N\frac{\partial A}{\partial t} + \frac{\partial NQ_{zl}}{\partial z} + \frac{\partial NQ_{xl}}{\partial x} = 0 \quad \text{where } Q_{zl} = Au, Q_{xl} = Av \tag{A.29}$$

A.5 Metal foams - the dimensionless form of the foam drainage equation

The foam drainage equation, and the equations used in the computation of the relative density profile of a metal foam, must be cast in a dimensionless form before numerical methods are applied to solve them.

A.5.1 Foam drainage equation

We wish to write equation A.23 in a dimensionless form. Defining $z = \zeta z_0, A = \alpha z_0^2, t = \tau t_0$, $\rho = \hat{\rho}\rho_0, g = \hat{g}g_0$, $\eta^* = \eta_0\hat{\eta}$, equation A.23 becomes

$$\left(\frac{z_0^2}{t_0}\right)\frac{\partial\alpha}{\partial\tau} + \frac{1}{z_0}\frac{\partial}{\partial\zeta}\left(\frac{1}{\eta_0\hat{\eta}}\left(\rho_0\hat{\rho}g_0\hat{g}z_0^2\alpha^2 - C\gamma z_0\frac{\sqrt{\alpha}}{2}\frac{z_0^2}{z_0}\frac{\partial\alpha}{\partial\zeta}\right)\right) = 0 \quad \text{(A.30)}$$

This gives

$$\left(\frac{\eta_0 z_0}{C\gamma t_0}\right)\frac{\partial\alpha}{\partial\tau} + \frac{\partial}{\partial\zeta}\left(\frac{1}{\hat{\eta}}\left(\left(\frac{\rho_0 g_0}{C\gamma}\right)\alpha^2\hat{\rho}\hat{g} - \frac{\sqrt{\alpha}}{2}\frac{\partial\alpha}{\partial\zeta}\right)\right) = 0 \quad \text{(A.31)}$$

and may be cleaned up by letting

$$t_0 = \frac{\eta_0 z_0}{C\gamma}, z_0 = \sqrt{\frac{c\gamma}{\rho_0 g_0}}, \implies t_0 = \frac{\eta_0}{\sqrt{C\gamma\rho_0 g_0}} \quad \text{(A.32)}$$

$$\frac{\partial\alpha}{\partial\tau} + \frac{\partial}{\partial\zeta}\left(\frac{1}{\hat{\eta}}\left(\hat{\rho}\hat{g}\alpha^2 - \frac{\sqrt{\alpha}}{2}\frac{\partial\alpha}{\partial\zeta}\right)\right) = 0 \quad \text{(A.33)}$$

Including the variation in the number of Plateau borders crossing a unit area of this foam, N, this becomes

$$N\frac{\partial\alpha}{\partial\tau} + \frac{\partial}{\partial\zeta}\left(\frac{N}{\hat{\eta}}\left(\hat{\rho}\hat{g}\alpha^2 - \frac{\sqrt{\alpha}}{2}\frac{\partial\alpha}{\partial\zeta}\right)\right) = 0 \quad \text{(A.34)}$$

The flow rate,

$$Q_l = A_{Pb}u = \frac{1}{\eta}\left(\rho g A^2 - \frac{C\gamma}{2A^{\frac{1}{2}}}\frac{\partial A}{\partial z}\right) \quad \text{(A.35)}$$

is cast in a dimensionless form by defining $Q_l = \hat{Q}_l Q_l^0$

$$\hat{Q}_l Q_l^0 = \frac{1}{\hat{\eta}\eta_0}\left(\hat{\rho}\hat{g}\rho_0 g_0 z_0^4\alpha^2 - \frac{C\gamma z_0\sqrt{\alpha}}{2}\frac{z_0^2}{z_0}\frac{\partial\alpha}{\partial\zeta}\right) \quad \text{(A.36)}$$

$$\hat{Q}_l\left(\frac{Q_l^0\eta_0}{C\gamma z_0^2}\right) = \frac{1}{\hat{\eta}}\left(\hat{\rho}\hat{g}\alpha^2 - \frac{\sqrt{\alpha}}{2}\frac{\partial\alpha}{\partial\zeta}\right) \quad \text{(A.37)}$$

$$\textit{So} \qquad \hat{Q}_l = \frac{1}{\hat{\eta}}\left(\hat{\rho}\hat{g}\alpha^2 - \frac{\sqrt{\alpha}}{2}\frac{\partial\alpha}{\partial\zeta}\right), \quad Q_l^0 = \frac{C^2\gamma^2}{3\chi\eta_0\rho_0 g} \quad \text{(A.38)}$$

A.5.2 Heat transfer equation

Now, we wish to write the heat equations in a dimensionless form.

$$Q_h = -\kappa \frac{\partial T}{\partial z} \tag{A.39}$$

$$\Phi_l \rho C_p \frac{DT}{Dt} = -\frac{\partial Q_h}{\partial z} \tag{A.40}$$

$$\Longrightarrow \rho C_p \Phi_l \left(\frac{\partial T}{\partial t} + u \frac{\partial T}{\partial z} \right) = -\frac{\partial}{\partial z} \left(\kappa \frac{\partial T}{\partial z} \right) \tag{A.41}$$

Let $C = \hat{C} C_0$, $\kappa = \hat{\kappa} \kappa_0$ and $\hat{\Phi}_l = N\alpha$. T_{init} is the initial homogeneous temperature of the sample, T_0 is the temperature of the cooling bath, and T_{crit} is the solidification temperature. $T = \Theta(T_{init} - T_0) + T_0$. In all cases considered $T_0 = 0$. Let $T = \Theta T_{init}$ so

$$\rho \hat{\rho} C \hat{C} \Phi_l \left(\frac{T_{init}}{t_0} \frac{\partial \Theta}{\partial \tau} + \frac{Q_l^0 \hat{Q}_l}{\alpha z_0^2} \frac{T_{init}}{z_0} \frac{\partial \Theta}{\partial \zeta} \right) = \frac{1}{z_0} \frac{\partial}{\partial \zeta} \left(\kappa_0 \hat{\kappa} \Phi_l \frac{T_{init}}{z_0} \frac{\partial \Theta}{\partial \zeta} \right) \tag{A.42}$$

where $u = \frac{Q_l}{A} = \frac{Q_l^0 \hat{Q}_l}{\alpha z_0^2}$.

$$\hat{\rho} \hat{C} \hat{\Phi}_l \left(\frac{\partial \Theta}{\partial \tau} + \left(\frac{C \gamma t_0}{\eta_0 z_0} \right) \frac{\hat{Q}_l}{\alpha} \frac{\partial \Theta}{\partial \zeta} \right) = \left(\frac{\kappa_0 t_0}{z_0^2 \rho_0 C_0} \right) \frac{\partial}{\partial \zeta} \left(\hat{\kappa} \hat{\Phi}_l \frac{\partial \Theta}{\partial \zeta} \right) \tag{A.43}$$

The Peclet number $Pe = \frac{z_0^2 \rho_0 C_0}{\kappa_0 t_0}$, so

$$\hat{\rho} \hat{C} \hat{\Phi}_l \left(\frac{\partial \Theta}{\partial \tau} + \frac{\hat{Q}_l}{\alpha} \frac{\partial \Theta}{\partial \zeta} \right) = \frac{1}{Pe} \frac{\partial}{\partial \zeta} \left(\hat{\kappa} \hat{\Phi}_l \frac{\partial \Theta}{\partial \zeta} \right) \tag{A.44}$$

A.5.3 Viscosity, specific heat and latent heat

The viscosity

$$\eta_* = \eta_*^0 + \frac{\eta_{max} - \eta_0}{1 + exp((w_\eta)(T - T_{crit}))} \tag{A.45}$$

can be rewritten in a dimensionless form as

$$\hat{\eta} = 1 + \frac{\left(\frac{\eta_{max}}{\eta_{*0}} - 1 \right)}{1 + exp((w_\eta T_{init})(\Theta - \Theta_{crit}))} \tag{A.46}$$

The specific heat

$$C = C_0 + \frac{L_f w_C}{\sqrt{(\pi)}} exp\left(-\left(w_C\left(T - T_{init}\right)\right)^2\right) \tag{A.47}$$

is also written in a dimensionless form using $C = \hat{C}C_0$, $L_f = \hat{L}_f C_0$ giving

$$\hat{C} = 1 + \left(\frac{\hat{L}_f w_C}{\sqrt{\pi}}\right) exp\left(-\left(\Theta_{init} w_C\left(\Theta - \Theta_{crit}\right)\right)^2\right) \tag{A.48}$$

A.5.4 Metal foam equations in 1d

The coupled equations which govern the formation of a 1d metal foam, where $N = 1$, are

$$\begin{aligned}
\frac{\partial \alpha}{\partial \tau} + \frac{\partial \hat{Q}_l}{\partial \zeta} &= 0 \\
\hat{Q}_l &= \frac{1}{\hat{\eta}}\left(\hat{\rho}\hat{g}\alpha^2 - \frac{\sqrt{\alpha}}{2}\frac{\partial \alpha}{\partial \zeta}\right) \\
\hat{\rho}\hat{C}\hat{\Phi}_l\left(\frac{\partial \Theta}{\partial \tau} + \frac{\hat{Q}_l}{\alpha}\frac{\partial \Theta}{\partial \zeta}\right) &= \frac{1}{Pe}\frac{\partial}{\partial \zeta}\left(\hat{\kappa}\hat{\Phi}_l\frac{\partial \Theta}{\partial \zeta}\right) \\
\hat{\eta} &= 1 + \frac{\left(\frac{\eta_{max}}{\eta_{*0}} - 1\right)}{1 + exp((w_\eta T_{init})(\Theta - \Theta_{crit}))} \\
\hat{C} &= 1 + \left(\frac{\hat{L}_f w_C}{\sqrt{\pi}}\right) exp\left(-\left(\Theta_{init} w_C\left(\Theta - \Theta_{crit}\right)\right)^2\right)
\end{aligned} \tag{A.49}$$

A.5.5 Two dimensions

The generalised foam drainage equation in two dimensions may be written as

$$N\frac{\partial A}{\partial t} = \frac{\partial}{\partial z}\left(\frac{N}{\eta^*}\left(\rho g A^2 - \frac{C\gamma A^{\frac{1}{2}}}{2}\frac{\partial A}{\partial z}\right)\right) + \frac{\partial}{\partial x}\left(\frac{NC\gamma A^{\frac{1}{2}}}{2\eta^*}\frac{\partial A}{\partial x}\right) = 0 \quad \text{(A.50)}$$

$$N\frac{\partial A}{\partial t} + \frac{\partial Q_{zl}}{\partial z} + \frac{\partial Q_{xl}}{\partial x} = 0 \quad \text{where } Q_{zl} = NAu, Q_{xl} = NAv \quad \text{(A.51)}$$

The dimensionless form of the first two terms has already been worked out. It remains to write the third term in a dimensionless form. Let $x = \xi z_0$, then

$$\frac{\partial}{\partial x}\left(\frac{NC\gamma A^{\frac{1}{2}}}{2\eta^*}\frac{\partial A}{\partial x}\right) = \frac{1}{x_0}\frac{\partial}{\partial \xi}\left(\frac{NC\gamma z_0\sqrt{\alpha}}{2\eta^*}\frac{z_0^2}{z_0}\frac{\partial \alpha}{\partial \xi}\right) \quad \text{(A.52)}$$

$$= \frac{\partial}{\partial \xi}\left(\frac{NC\gamma z_0\sqrt{\alpha}}{2\eta^*}\frac{\partial \alpha}{\partial \xi}\right) \quad \text{(A.53)}$$

Dividing across by $C\gamma z_0$, in a similar manner to equation A.31 gives

$$N\frac{\partial \alpha}{\partial \tau} + \frac{\partial}{\partial \zeta}\left(\frac{N}{\hat{\eta}}\left(\hat{\rho}\hat{g}\alpha^2 - \frac{\sqrt{\alpha}}{2}\frac{\partial \alpha}{\partial \zeta}\right)\right) - \frac{\partial}{\partial \xi}\left(\frac{NC\gamma z_0\sqrt{\alpha}}{2\eta^*}\frac{\partial \alpha}{\partial \xi}\right) = 0 \quad \text{(A.54)}$$

The heat flow equation, A.41, becomes

$$\rho C_p \Phi_l\left(\frac{\partial T}{\partial t} + u\frac{\partial T}{\partial z} + v\frac{\partial T}{\partial x}\right) = -\frac{\partial}{\partial z}\left(\kappa\frac{\partial T}{\partial z}\right) - \frac{\partial}{\partial x}\left(\kappa\frac{\partial T}{\partial x}\right) \quad \text{(A.55)}$$

in two dimensions. Its dimensionless equivalent equation is

$$\hat{\rho}\hat{C}\hat{\Phi}_l\left(\frac{\partial \Theta}{\partial \tau} + \frac{\hat{Q}_{zl}}{\alpha}\frac{\partial \Theta}{\partial \zeta} + \frac{\hat{Q}_{xl}}{\alpha}\frac{\partial \Theta}{\partial \xi}\right) = \frac{1}{Pe}\left(\frac{\partial}{\partial \zeta}\left(\hat{\kappa}\hat{\Phi}_l\frac{\partial \Theta}{\partial \zeta}\right)\right) + \frac{1}{Pe}\left(\frac{\partial}{\partial \xi}\left(\hat{\kappa}\hat{\Phi}_l\frac{\partial \Theta}{\partial \xi}\right)\right) \quad \text{(A.56)}$$

where number Pe is the Peclet number as before.

Bibliography

[1] Daniel, J. C. and Audebert, R., *Small Volumes and Large Surfaces: The World of Colloids*, Soft Matter Physics, Daoud, M. and Williams C. E., (eds.), pp. , Springer-Verlag Berlin, (1999).

[2] *Soft Matter Physics*, Daoud, M. and Williams C. E., (eds.), Springer-Verlag Berlin, (1999).

[3] Weaire, D. and Hutzler, S., *The Physics of Foams*, Oxford University Press (1999).

[4] Gibson, L. J. and Ashby, M. F., *Cellular Solids*, Pergamon Press, (1998).

[5] Ekserova, D. R., Krugliakov, P. M., *Foam and foam films : theory, experiment, application*, Oxford, (1998).

[6] Plateau, J.A.F., *Statique expèrimentale et théorique des liquides soumis aux seules forces molècularies*, Gauthier-Villars, Paris, (1873).

[7] Taylor, J. E., *The structure of singularities in soap-bubble-like and soap-film-like minimal surfaces*, Ann. Math. **103**, pp 489-539, (1976).

[8] Verbist, G. and Weaire, D., *A Soluble Model for Foam Drainage*, Europhys. Lett. **26**:631-634, (1994).

[9] Verbist, G., Weaire, D. and Kraynik, A.M., *The foam drainage equation.* J. Phys.:Condensed Matter **8**:3715-3731, (1996).

[10] Weaire, D., Hutzler, S., Verbist, G. and Peters, E., *A review of the foam drainage equation*, Advances in Chemical Physics **102**, pp. 315-374, (1997).

[11] Koehler, S. A., Stone, H. A., Brenner, M. P., and Eggers J., *Dynamics of foam drainage*, Phys. Rev. E, No. **58**, pp 2097 (1998).

[12] Koehler, S. A., Hilgenfeldt, S. and Stone, H. A., *Liquid flow through aqueous foams: the node dominated foam drainage equation*, Phys. Rev. Lett. No. **82**, pp 4232-4235.

[13] Brakke, K., *The Surface Evolver*, Experimental Math. **1**, 141. (1992).

[14] Phelan, R., *Ph. D Thesis*, University of Dublin Library, (1996).

[15] Phelan, R., Weaire, D., Brakke, K., , Experimental Math **4** , No. 3. 181, (1995).

[16] Weaire, D. and Phelan, R., J. Phys. Condens. Mat. **8**, pp 9519, (1996).

[17] Bradley, K. G., Pittet, N. and Weaire, D., *Cylindrical foams*, Proceedings of EuroFoam 2000 Conference, P. 38.

[18] Bradley, K. G. and Weaire, D., *Instabilities in two liquid drops in contact*, Accepted for publication pending corrections, Computers in Scientific Engineering.

[19] Cox, S. J., Bradley, K. G., Hutzler, S. and Weaire, D., *Vertex corrections in the theory of foam drainage*, J. Phys.: Condens. Matter **13** (2001)1-7.

[20] Kraynik, A. M., Neilsen, M. K., Reinelt, D. A. and Warren, W. E., *Foam micromechanics*, Foams and Emulsions, Sadoc, J. F. and Rivier, N. (eds.), pp 259-286, (1999).

[21] Kraynik, A. M., Reinelt, D. A. and Loewenberg, M., *Foam Mircorheology*, Foams and Films, Weaire, D. and Banhart, J. (eds.), MIT-Verlag, Bremen (1999), pp 97-104.

[22] Reinelt et al., Private communications.

[23] Weaire, D., Bradley, K. G. and Phelan, R., *Speculations and calculations in the physics of foams* Soft Condensed Matter: Configurations, Dynamics and Functionality, Skjeltorp, A. T. and Edwards, S. F. (eds), 247-268. Kluwer Academic Publishers (2000).

[24] *FLUENT 5 User's Guide Volume I*, Fluent Incorpoated (1998).

[25] Taupin, C., *The Physicochemistry of Surfactants*, Soft Matter Physics, Daoud, M. and Williams, C. E. (eds.), pp. 132-153. Springer-Verlag Berlin, (1999).

[26] Seelinger, H. W., Metal Foams and Porous Metal Structures, Banhart, J., Ashby, M. and Fleck, N., (eds), MIT-Verlag, Bremen (1999), p. 23.

[27] Baumgartner, F., Duarte, I. and Banhart, J., *Industrialisation of Powder Compact Foaming Process* Advanced Engineering Materials 2000, 2, No. **4**. pp. 168-174, (2000).

[28] Weaire, D, Hutzler S. and Pittet, N., *Cylindrical packings of foam cells*, Forma, **7**, pp. 259-263, (1992).

[29] Pittet, N., Rivier, N. and Weaire, D., *Cylindrical packings of foam cells*, Forma, **10**, pp. 65-73 (1995).

[30] Pittet, N, Boltenhagen, P., Rivier N. and Weaire D., *Structural transitions in ordered, cylindrical foams*, Europhys. Lett., **35**, pp. 547-552 (1996).

[31] Thompson, D., *On growth and Form*, University Press, Cambridge, pp. 912-933 (1942).

[32] Mann, W. B. and Stephens, R. W. B., *Bubble formation in glass tubes*, Phil Mag **15**, pp. 143-146 (1933).

[33] Dodd, J. D., *An approximation of the minimal tetrakaidecahedron*, American Journal of Botany **42**, pp. 566-569 (1955).

[34] Bragg, L. and Nye, J.F., Proceedings of the Royal Soc. of London **190**, pp. 474-481 (1947).

[35] Boltenhagen, P. and Pittet, N., *Structural transitions in crystalline foams*, Europhys. Lett., **41** (5), pp. 571-576 (1996).

[36] Boltenhagen, P.,Pittet, N. and Rivier, N., *Giant deformations and topological hysteresis of an ordered foam*, Europhys. Lett., **43** (6), pp. 690-694 (1998).

[37] Hutzler, S., Weaire, D. and Crawford, R., *Moving boundaries in ordered cylindrical foam structures*, Philosophical Magazine B, 1997, **75**,No. 6, pp. 845-857.

[38] Weaire, D. and Phelan, R., *Vertex instabilities in foams and emulsions*, J. Phys.: Condens. Matter **8** (1996) L37-L43.

[39] Weaire, D. and Phelan, R., *Cellular structures in three dimensions*, Phil. Trans. R. Soc. Lond. A (1996) **354**, 1989-1997.

[40] Brakke, K., Private communications.

[41] Fortes, M. A. and Emilia Rosa, M., *Topological transitions during deformation of small clusters of bubbles*,

[42] Monti, R. and Savino, R., *Coalescence and Wetting Prevention by Marangoni effect Foams and Films*,

[43] Monti, R. and Dell'Aversana, P., *Microgravity experimentation in non-coalescing systems*, Microgravity Q. Vol. **4**, 123 (1994).

[44] Monti, R., Savion, R. and Tempesta, S., *Wetting prevention by thermal Marangoni effect. Experimental and numerical simulations*, European Journal of Mechanics B/Fluids 17,51 (1998).

[45] Dell'Aversana, P. and Neitzel, G. P., *When Liquids Stay Dry* Physics Today January 1998, p. 38.

[46] Valkovska, D. S. and Danov, K. D., *Mutual approach and stability of two slightly deformed bubbles*, Proceedings of EuroFoam 2000 Conference.

[47] Strong, C. L., *The Amateur Scientist: Curious bubbles in which a gas encloses a liquid instead of the other way around*, Scientific America, **230**, pp. 116-120, (April 1974).

[48] Skogen, N., American Journal of Physics, **24**, p. 239.

[49] Monti, R., Savino, R. and Cicala, A., *Surface Tension driven-flow in non-coalescing liquid drops*, Acta Astromautica, **38**, p. 937 (1996).

[50] Monti, R and Savino, R., *Correlation between experimental results and numerical solutions of the Navier-Stokes problem for non-coalescing liquid drops with Marangoni effects*, Physics of Fluids, **9**, p. 260 (1997).

[51] Monti, R. and Sovino, R., *Numerical model of non coalesence liquid drops and correlation with experimental results*, Microgravity Q. Vol. 6, **2-3**, pp. 102-108 (1996).

[52] Brakke, K., *The Surface Evolver and the stability of liquid surfaces*, Phil. Trans. R. Soc. Lond. A (1995).

[53] Killingbeck, J. P., *Microcomputer Quantum Mechanics*, Adam Hilger Ltd., Bristol, Second edition (1983).

[54] Brakke, K., *Hessian, Eigenvalues, Eigenvectors, and Stability in the Surface Evolver*, http://www.susqu.edu/facstaff/ b/brakke/evolver/html/ eigentut.htm

[55] Lenz, P. and Lipowsky, R., *Morphological transitions of wetting layers on structured surfaces*, Phys. Rev. Lett., vol. 80, **9**, pp. 1920-1923, (1998).

[56] Lemlich, R., J. Coll. Int. Sci., **64**, 107, (1977).

[57] Pertsov, A. V., Porodenko, E. V., and Simonov, A. V., *Plateau-Gibbs Borders: Calculation of shape, volume, and transport parameters.* Colloid Journal, Vol. 57, **5**, pp. 673-677, (1995).

[58] White, F. M., *Viscous Fluid Flow*, McGraw-Hill series in mechanical engineering, (1991).

[59] Landau, L. D. and Lifshitz, E. M., *Fluid Mechanics*, Pergamon Press, Second ed., (1987).

[60] Tannehill, J. C., Anderson, D. A. and Pletcher, R. H., *Computational Fluid Mechanics and Heat Transfer*, Taylor & Francis, Second Edition (1997).

[61] Shah, R. K., London., A. L., *Laminar Flow Forced Convection in Ducts*, Academics, New York, (1978).

[62] Boas, M. L., *Mathematical methods in the physical sciences*, Wiley, Second Edition, (1983).

[63] *Gambit I Modelling Guide*, Fluent Incorpoated (1998).

[64] Peters, E. A. J. F., MSc. Thesis. Eindhoven University of Technology, Eindhoven, (1995).

[65] Leonard, R. A. and Lemlich, R., AIChE J. 11 18, (1965).

[66] Koehler, S. A., Hilgenfeldt, S. and Stone, H. A., *Foam drainage: Experiments and a new model*, Foams and Films, Weaire, D. and Banhart, J. (eds.), MIT-Verlag, Bremen (1999), pp 49-58.

[67] Baumeister, J., German Patent DE 40 18 360 (1990); US Patent 5 151 246 (1992); European Patent EP 0460392A1 (1996)

[68] Baumeister, J. and Schrader, H., German Patent DE 41 01 630 (1991)

[69] Baumeister, J., Banhart, J. and Weber, M., German Patent DE 44 26 627 (1997)

[70] Cox, S. J., Bradley, K. G. and Weaire, D., *Modelling metallic foam formation: The competition between heat transfer and drainage*, Proc. Roy. Soc. 2000, in print.

[71] Neethling, S. and Cilliers, J. J., *A visual kinematics model of flowing foam incorporating coalesence*, Powder Technology, 101:249-256, (1999).

[72] Neethling, S. and Cilliers, J. J., *Visualisation and drainage of coalescing, flowing foams*, Foams and Films, Weaire, D. and Banhart, J. (eds.), MIT-Verlag, Bremen (1999), pp. 117-124.

[73] Cos, S. J., Alonso, M. D., Pittet, N. and Weaire, D., *The Stokes experiment on a foam*, Proceedings of EuroFoam 2000 Conference.

[74] Hutzler, S., Weaire, D. and Shah, S. *Bubble sorting*, Phil. Mag. Lett. **80**, p 41, 2000.

[75] Weaire, D., Pittet, N. and Hutzler, S., Phys. Rev. Lett. **71**, 2670 (1993).

[76] Durand, M., Martinoty, G. and Langevin, D., Phys. Rev. E. **60** R6307, (1999).

[77] Saint-James, A., Vera., M. U. and Durian, D. J., Europhys. Lett. **50**, 695, (2000).

[78] Goldfarb, I. I., Kahn, K. B. and Schreiber, I., Inz. Akad. Nauk SSSR **2** 103, 1987.

[79] Helbing, D. and Treiber, M., *Numerical simulations of macroscopic traffic equations*, Computing in Science and Engineering, Vol. 1 No. 5, pp. 89-99, (1999).

[80] Press, W. H., Teukolsky, S. A., Vetterling, W. T. and Flannery, B. P., *Numerical recipes in C*, Cambridge University Press, (Second Edition) 1992.

[81] Lax, P. D., *Weak solutions of Nonlinear Hyperbolic Equations and their Numerical Computation*, Commun. Pure Appl. Math., vol. 7, pp. 159-193, (1954).

[82] Lax, P. D. and Wendroff, B., *Systems of Conservation Laws*, Commun. Pure Appl. Math., vol. 13, pp. 217-237, (1960).

[83] MacCormack, R. W., *Numerical solutions of Viscosity in Hypervelocity Impact Cratering*, AIAA Paper 69-354, Cincinnati, Ohio. (1969).

[84] Banhart, J., Ashby, M.F. and Fleck, N.A. (eds)., *Metal foams and Porous Metal Structures*, MIT, Bremen.

[85] Körner, C. and Singer, R. F., *Numerical simulations of foam formation and evolution with modified cellular automata*, Metal Foams and Porous Metal Structures, Banhart, J., Ashby, M. and Fleck, N., (eds), MIT-Verlag, Bremen. p. 23 (1999).

[86] Banhart, J., Baumeister, J., *Production methods for metallic foams*, Proc. MRS Spring Meeting, San Francisco, (1998).

[87] Menzel, Donald H., *Boundary Value Problems in General*, Mathematical Physics, Dover Publications, pp. 224-225, (1961).

[88] Murphy, J., *New dimensions on the foam drainage equation*, Shell trainee report, (1998).

[89] *Maple*, Waterloo Maple, Inc., (1997).

[90] Weaire, D. and Banhart, J., (eds.), Foams and Films, MIT-Verlag, Bremen (1999).

[91] Tegart, J., *AiAA Paper AIAA-91-2174*, 27th Joint Propulsion Conference, Sacramento, CA (1991).

[92] Racz, L.M., Szekely, J. and Brakke, K., ISIJ International, **33**, 2. (1993).

[93] Brakke, K., Surface Evolver Manual, Version 2.14, (1999).

[94] Bolton, F., *PLAT: A computer program for the simulation of a two-dimensional foam*, http://www.tcd.ie/Physics/People/Denis.Weaire /foams, (1990).

[95] Kermode, J. P. and Weaire, D., *2D-FROTH: A program for the investigation of 2-dimensional froths*, Computer Physics Communications, **60**, pp 75-109, (1990).

[96] Brakke, K., Surface Evolver Manual, Version 2.10. pp. 18-21, pp. 36-39., (1998).

[97] Bourne, D. E. and Kendall, P. C., *Vector analysis and Cartesian tensors* Chapman and Hall, Third edition, (1992).

[98] Cox, S. J., Weaire, D., Hutzler, S., Murphy, J., Phelan, R. and Verbist, G., *Applications and generalisations of the foam drainage equation* Proc. Royal. Soc. (in press).